Line, Surface, and Volume Integral Equations for the Electromagnetic Modelling of the Electroencephalography Forward Problem

Axelle Pillain

UNIVERSITE
BRETAGNE
LOIRE

THÈSE / Télécom Bretagne
sous le sceau de l'Université Bretagne Loire
pour obtenir le grade de Docteur de Télécom Bretagne
En accréditation conjointe avec l'Ecole Doctorale Sicma
Mention : Sciences de l'Ingénieur

présentée par
Axelle Pillain
préparée dans le département Micro-ondes
Laboratoire Labsticc, Pôle MOM

Line, Surface, and Volume Integral Equations for the Electromagnetic Modelling of the Electroencephalography Forward Problem

Thèse soutenue le 11 octobre 2016
Devant le jury composé de :

François Rousseau
Professeur, Télécom Bretagne / Président

Théodore Papadopoulo
Directeur de Recherche, Inria - Sofia Antipolis / Rapporteur

Kristof Cools
Associate Professor, University of Nottingham / Rapporteur

Anatole Lecuyer
Directeur de Recherche, Inria - Rennes / Examinateur

Jussi Lindgren
Ingénieur, Irria Rennes / Examinateur

Francesco P. Andriulli
Professeur, Télécom Bretagne/ Directeur de thèse

N° d'ordre 2016telb0412

Sous le sceau de l'Université Bretagne Loire

Télécom Bretagne

En accréditation conjointe avec l'Ecole Doctorale Sicma

Line, Surface, and Volume Integral Equations for the Electromagnetic Modelling of the Electroencephalography Forward Problem

---

Thèse de Doctorat

Mention : Sciences de l'Ingénieur

Présentée par **Axelle Pillain**

Département Micro-ondes

LabSTIC, Pôle : MOM

Directeur de thèse : Francesco P. Andriulli

Soutenue le 11 Octobre 2016

Jury
M. Théodore Papadopoulo, Directeur de Recherche, INRIA Sofia Antipolis (Rapporteur)
M. Kristof Cools, Associate Professor, University of Nottingham (Rapporteur)
M. Anatole Lecuyer, Directeur de Recherche, INRIA Rennes
M. Jussi Lindgren, Ingénieur, INRIA Rennes
M. François Rousseau, Professeur, Télécom Bretagne, Brest
M. Francesco P. Andriulli, Professeur, Télécom Bretagne, Brest (Directeur de thèse)

To those I love and love me

Acknowledgements

Eventually reaching this section, I have a lack of inspiration to express my gratitude to the persons I met during these years. There are many I would like to thank and few words to say it.

First and foremost, I am deeply grateful to my advisor, Francesco Andriulli, who introduced me to computational electromagnetics and gave me the opportunities to meet the community and visit many places. He has gone far beyond scientific advising only and I will not forget his commitment and strive for diversity.

The years in the new born CERL would never have been the same without my fellow PhD students and post doc. For the moments we spent together I would like to express my sincere gratitude to Lyes Rahmouni, a real gentleman since the beginning, John Erick Ortiz Guzman, for supporting me even or especially after 18:30 in the office, Adrien Merlini, (stop complaining! and it is not my fault), Simon Adrian, Rajendra Mitharwal, Maksims Abalenkov, Abdelrahm Ijeh, Riswan Masood(i) and Alexandre Dely.

I should also thanks Stanislas Marie Antoine Penhirin, otherwise known as "Stan", for all our scientific discussions on a wide range of subjects.

Marie-Odette, your support has been a great value during these years. I can only say "thank you" and wish that our friendship continue as it is. Kenza and Inès, we haven't finished our tour of Europe! Despite the distance, the weekends spent together were unforgettable and a warm breath of oxygen.

I should not forget my small gymnastics community, and in particular my coach, Myriam, thank you for believing in me since the very beginning.

Last, I wish I could express better my deep gratitude to my family, my parents, my brother and my sisters, for your support, friendship, crises, love,... in a nutshell for the path you helped me to follow and the sailing we do together.

Abstract

The work presented in this thesis focuses on developing new modelling tools for the electroencephalography (EEG) forward problem using the boundary elements method. Indeed, in the EEG forward problem (i.e. the computation of the electric potential at the scalp, knowing the electric current source configuration in the brain) it is often necessary to model the anisotropic conductivity profiles of the skull and of the white matter. These profiles, however, cannot be handled by standard surface integral formulations (Boundary Element Methods, BEMs). The work presented fits the general framework of electromagnetic modelling. The introductory chapter shows how from Maxwell's equations we can derive the EEG forward problem. It is also explained how this problem can be solved by using integral equations and the Boundary Element Methods. The discussion on the function spaces, besides familiarizing the readers with them, also allows to show that the usual discretization of the current integral EEG formulation does not abide by the spectral properties of the operators.

The second chapter seeks to fill the gap in the treatment of anisotropy in the EEG forward problem within the framework of the boundary element method. A new surface integral formulation for the EEG forward problem that can handle anisotropic conductivity profiles is proposed. The main challenge resides in the fact that standard formulations for the isotropic case can leverage on

the existence of a globally harmonic function satisfying the isotropic and homogeneous Poisson's equation in each head compartment. In the case of the anisotropic EEG forward problem, instead, a solution of the homogeneous Poisson's equation in one compartment will not be, in general, a solution of the homogeneous Poisson's equation in a different compartment of the head. To circumvent this problem, we opted in this work for an indirect formulation. This strategy has also the advantage of straightforwardly enabling the treatment of non-nested head compartments. Furthermore, a mixed discretization is employed to further improve the accuracy of the new formulation. A set of numerical results is presented to corroborate all theoretical treatments and to show the impact of the proposed approach on both canonical and real case scenarios.

The third chapter assesses the impact of mixed forward EEG formulations in the EEG inverse problem. Its contribution is twofold : (i) to merge the mixed forward formulation with the inverse algorithm in a stable way, that would allow to decrease the error which is traditionally observed when the source approaches the boundary; (ii) to show by mean of extensive numerical assessments that mixed discretization BEM formulations compare favorably with previously existing techniques and that this technique can be easily adapted to real case scenarios.

In the fourth chapter, we show how the preconditioning effect of Calderon strategies can be extended from the classical framework (high frequency, homogeneous media) to multilayered media. This result is quite relevant for EEG simulations since high resolution brain imaging necessitates to solve with a high accuracy the EEG forward problem. This means that the mesh used to model the geometry of the head should be very dense. Without any fast direct

techniques, the high dimensions of the problem prevent the use of direct solvers and iterative solvers must be used. The precision of the solution obtained with an iterative solver as well as the rapidity of computation of the solution directly depends on the condition number of the system matrix. Calderon preconditioning technique enables to get a stable condition number with the mesh refinement by multiplying the system matrix with an operator which is spectrally equivalent to its inverse. The contribution of this chapter proves that Calderon techniques are applicable to the multilayered EEG forward problem. This is further corroborated by means of numerical evidences.

Chapter five proposes a Calderon preconditioner for the wire Electric Field Integral Equation. The proposed preconditioner uses the classical and modified single layer operators in 1D. The preconditioning technique allows to build a system matrix whose condition number is stable with the mesh refinement when the geometry is closed. For open curves the condition number grows, but only logaritmically, i.e. $O(log(1/h))$ with h the mesh parameter. The idea of modelling wires with 1-D curves is extended to the brain. The chapter ends by presenting also a new wire (1D) integral equation for the EEG forward problem to take into account the anisotropy of the white matter fibers.

The sixth chapter studies the impact of a fast direct solver in solving the EEG forward problem. Such a solver enables to get the solution of a matrix equation in $O(N^{1.5})$ instead of $O(N^3)$ in the case of pure direct solver (where N is the number of unknowns in the system). Since the solution of the EEG inverse problem requires many solutions of the EEG forward problem, the advantage of a fast direct solver can be seen both in computing the solution of the inverse and in the forward EEG problem. This chapter presents preliminary results on the impact of the use of such a solver in forward modelling.

Finally, chapter seven presents the conclusions of this thesis and delineate some avenues for future investigations.

Résumé

Le travail présenté dans cette thèse s'articule autour du développement de nouveaux outils de modélisation du problème direct de l'électroencéphalographie (EEG). En exploitant les trois dimensions de l'espace, lignes, surface et volume, le travail permet de représenter précisément les différentes caractéristiques du milieu de propagation qu'est la tête. En effet, lors de la résolution du problème direct de l'EEG, c'est-à-dire lors du calcul du potentiel électrique au niveau du scalp, il est nécessaire de modéliser correctement les propriétés anisotropes du crâne et de la matière blanche. Ces propriétés ne peuvent pas être prises en compte par les formulations intégrales présentes dans la littérature. Le travail présenté entre dans le cadre plus général de la modélisation des phénomènes électromagnétiques. Le chapitre introductif montre comment il est possible d'obtenir les équations modélisant le problème direct de l'électroencéphalographie à partir des équations de Maxwell. Ainsi le problème direct de l'electroencéphalogrphie est donné par

$$\nabla \cdot \bar{\bar{\sigma}} \nabla V = f \tag{1}$$

où V est le potentiel inconnu, $\bar{\bar{\sigma}}$ le tenseur de conductivité de chaque domaine et f la source électrique. Une unique solution (à une constante près) est assurée avec les conditions aux frontières suivante, à chaque interface Γ_{ij} entre deux domaines Ω_i et Ω_j de conductivité différente

$$[V]_{ij} = 0 \ \forall i, \forall j \in \omega_i \setminus \{N+1\} \tag{2a}$$

$$[\vec{n} \cdot \bar{\bar{\sigma}} \nabla V]_{ij} = 0 \ \forall i, \forall j \in \omega_i. \tag{2b}$$

Ce chapitre explique aussi la manière dont ce problème peut être résolu en utilisant les équations intégrales et la méthode des moments. La discussion sur les espaces de Sobolev, au-delà de familiariser le lecteur avec ces derniers, permet de montrer que la discrétisation standard, de type Galerkin, utilisée dans les formulations actuelles du problème direct de l'EEG ne correspond pas aux propriétés spectrales des opérateurs.

Le second chapitre cherche à combler les lacunes des formulations intégrales actuelles du problème direct de l'EEG dans le traitement de l'anisotropie. Une nouvelle formulation intégrale surfacique est ainsi proposée. Le défi principal réside dans le fait que les formulations actuelles traitant le cas isotrope peuvent exploiter l'existence d'une fonction globalement harmonique dans le domaine considéré. Cette fonction satisfait à l'équation de Poisson dans chaque compartiment de la tête. Dans le cas du problème direct de l'EEG anisotrope, une solution de l'équation homogène de Poisson dans un compartiment n'est en général pas une solution de l'équation de Poisson homogène dans un compartiment différent. Pour résoudre ce problème, nous avons eu recourt à une formulation indirecte. Cette stratégie a de plus l'avantage de permettre directement le traitement de géométries de la tête non définies par couches et donc plus générales. En considérant la géométrie

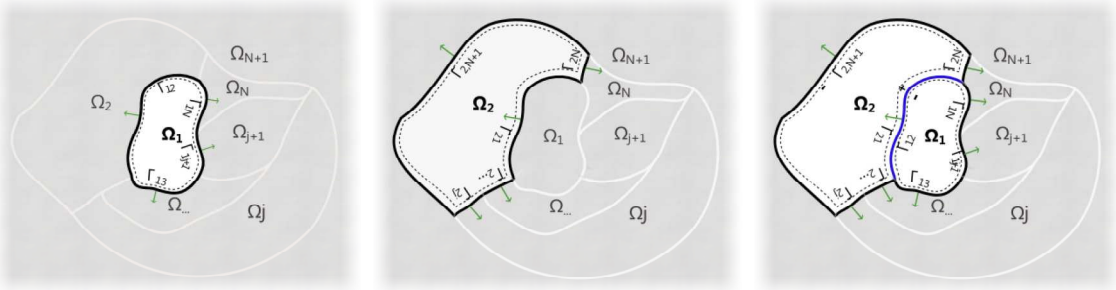

(a) Problème intérieur dans Ω_1. (b) Problème intérieur dans Ω_2. (c) Problème à l'interface entre Ω_1 et Ω_2.

Figure 1: Notations pour obtenir la nouvelle équation intégrale du problème direct de l'EEG prenant en compte l'anisotropie du milieu cérébral

décrite Figure1, les deux équations intégrale que nous obtenons pour chaque interface Γ_{ij}

du domaine considéré sont les suivantes:

$$\sum_{k\in\omega_i} S_i\phi_{ik} - \sum_{l\in\omega_j} S_j\phi_{jl} = -(\gamma^-_{0,ij}v_i - \gamma^-_{0,ji}v_j) \tag{3}$$

$$\frac{1}{2}\phi_{ij} + \sum_{k\in\omega_i} D^*_i\phi_{ik} + \frac{1}{2}\phi_{ji} - \sum_{l\in\omega_j} D^*_j\phi_{jl} = -(\gamma^-_{1,ij}v_i - \gamma^-_{1,ij}v_j). \tag{4}$$

où S_i et D^*_i sont respectivement l'opérateur simple couche et l'opérateur double couche adjoint associés à l'équation de Poisson anisotropique; l'ensemble ω_i représente les domaines voisins de Ω_i; v_i est le potentiel connu généré par une source placé dans le domaine Ω_i ne prenant pas en compte les conditions aux frontières et ϕ_{ik} est la densité aux frontières inconnue telle que $V_i = v_i + S_i\phi_i = v_i + \sum_k S_i\phi_{ik}$.

Une discrétisation de type mixe est employée, ceci afin d'améliorer la précision de la formulation. L'ensemble des résultats numériques présentés confirme les développements théoriques et montre l'impact de la nouvelle approche dans les cas de scénarios canoniques et réalistes. La Figure 2 que lors de l'augmentation de la densité du maillage, l'erreur relative avec la solution de référence diminue. Ceci confirme la validité de la solution proposée. Une comparative montre que la précision de la solution obtenue est comparable à la précision des solutions intégrale existant dans la littérature. Ces résultats sont montrés Figures 3 et 4. Dans ce chapitre, il est aussi montré que la formulation proposée peut être appliqué à des maillages volumiques en fusionnant les différents tétrahèdres lorsque la conductivité est la même comme montré Figure 4

Le troisième chapitre de ce manuscrit cherche à évaluer l'impact de l'emploi d'une discrétisation de type mixe dans les formulations intégrales standard du problème inverse de l'EEG. Sa contribution est (i) de relier les discrétisations mixes du problème direct au problème inverse d'une manière stable, ce qui permet de diminuer l'erreur de localisation lorsque la source électrique est proche d'une frontière; (ii) de montrer, à l'aide de plusieurs simulations numériques, que les formulations aux éléments de frontière (BEM) ayant une

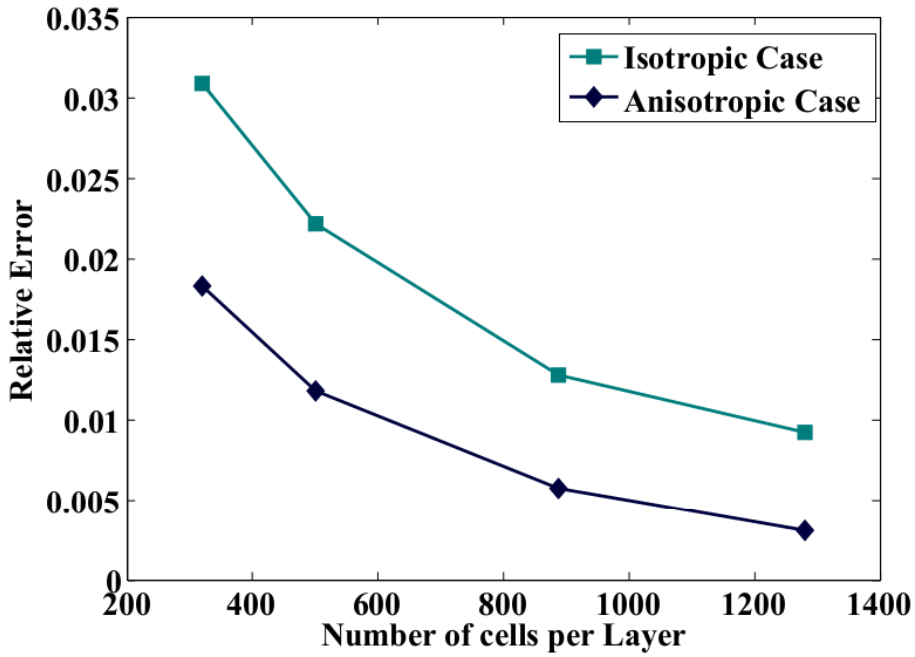

Figure 2: Convergence de la solution de l'équation intégrale proposée avec l'accroissement du nombre d'inconnues (la solution de référence est la solution analytique dans le cas isotropique et une solution aux éléments finis dans le cas anisotropique.

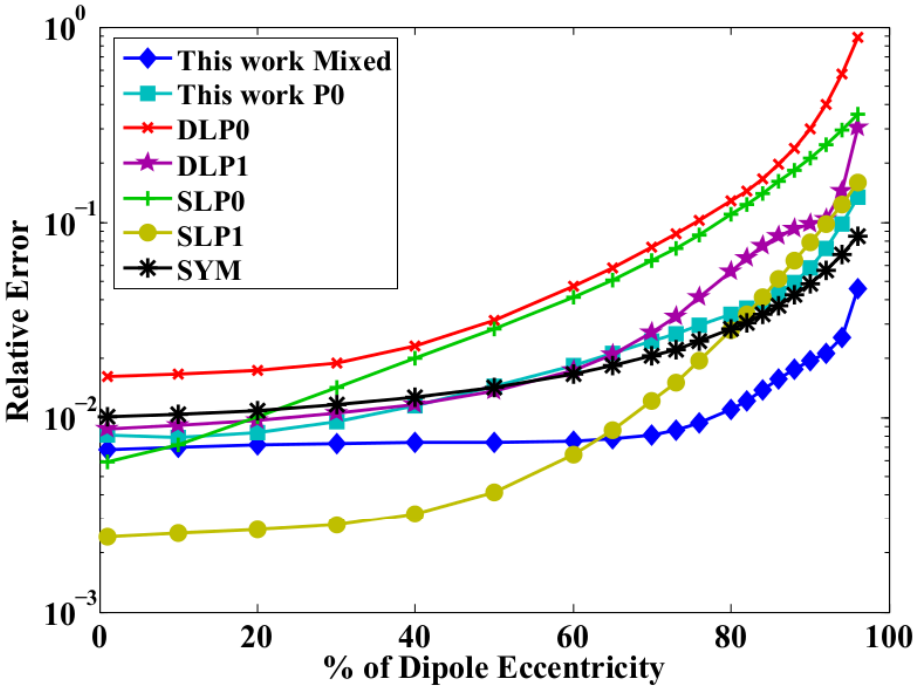

Figure 3: Erreur relative par rapport à l'excentricité de la source dipolaire pour la méthode proposée dans ce travail et d'autres formulations existantes dans la littérature.

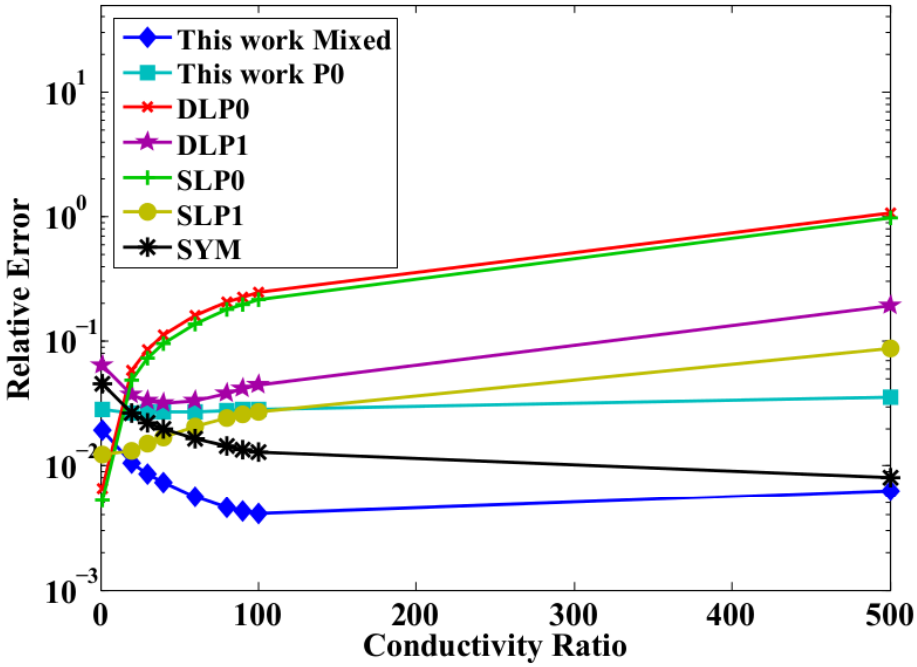

Figure 4: Erreur relative par rapport au rapport de conductivité (entre le cerveau et le crâne) pour la méthode proposée dans ce travail et d'autres formulations existantes dans la littérature.

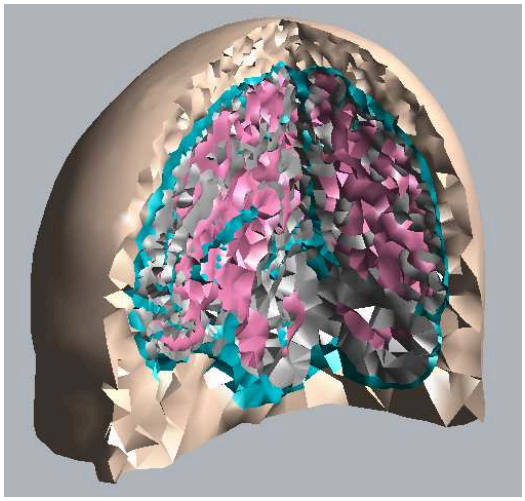

(a) Maillage volumique.

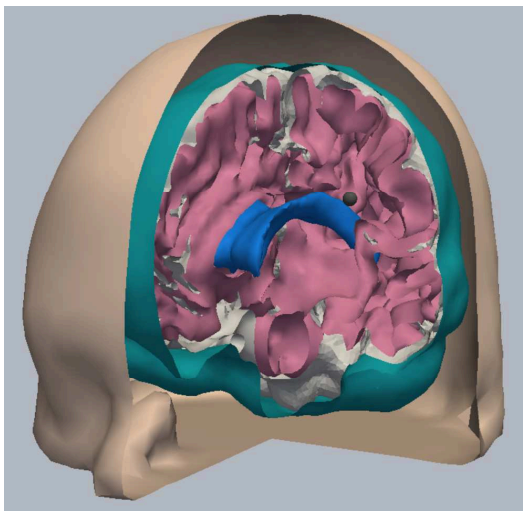

(b) Maillage surfacique obtenu après preprocessing selon les valeurs de conductivité des tétrahèdres..

Figure 5: Maillage volumique obtenu à partir des données IRM avant (a) et après preprocessing (b).

discrétisation mixes sont favorablement comparables aux formulation BEM ayant une discrétisation de type Galerkin et que ces méthodes peuvent être facilement adaptées à des scénarios réalistes. La méthode employé ici pour résoudre le problème indirect de l'EEG est distributive et linéaire : les sources inconnues responsables du potentiel mesuré à la surface du scalp sont placées sur une grille cartésienne, pour chaque source de la grille, la solution au problème direct est calculé. Dans les résultats présentés, l'inversion est réalisée à l'aide de sLORETA. On montre Figure 6 que lorsqu'une discretisation de type mixe est employée, la localisation est plus résistante à la présence de bruit dans les mesures.

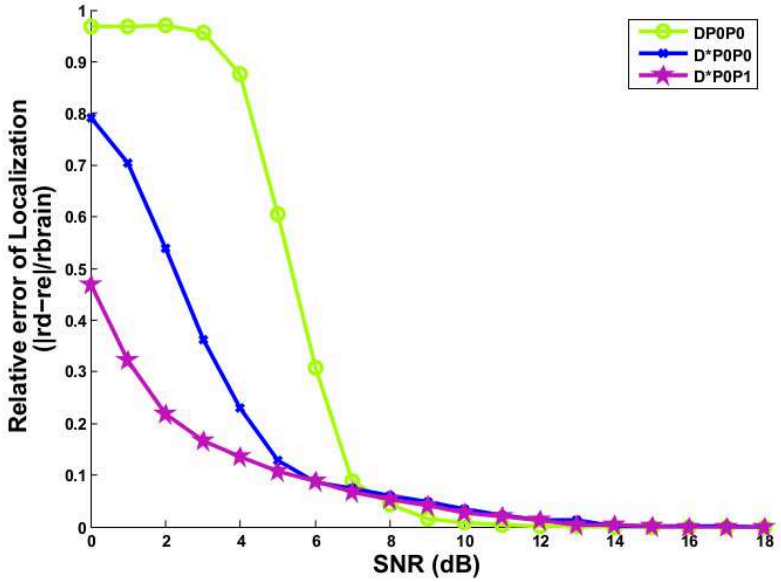

Figure 6: Erreur de localisation par rapport au SNR, l'erreur de localisation est donné par $|r_d - r_e|$ où r_d représente la vraie position du dipole position et r_e sa position estimée.

L'imagerie cérébrales haute résolution nécessite de résoudre avec une grande précision le problème direct de l'EEG. Cela signifie que la géométrie de la tête doit être fidèlement reproduite lors de la résolution du problème direct. Par conséquent, cela implique que les maillages utilisés doivent être très denses. Sans technique de résolution rapide directe, les grandes dimensions du problème empêchent la résolution directe du problème et un solveur itératif doit être utilisé. La précision de la solution obtenue en utilisant une technique itérative ainsi que le nombre d'itérations requis dépend du conditionnement de

la matrice du système. La contribution du quatrième chapitre montre que les techniques de préconditionnement de type Calderon, connues dans le domaine des hautes fréquences pour les milieux homogènes peut être étendue aux milieux multicouches. Ce résultats est appliqué à l'imagerie cérébrale en présentant des résultat liés à l'introduction d'une technique de préconditionnement de type Calderon pour la formulation symmétrique du problème direct de l'EEG. En effet, différemment des autres formulations du problème direct de l'EEG, cette formulation intégrale esst de première espèce. La technique proposée permet d'obtenir un conditionnement de la matrice du système stable avec le raffinement du maillage. Cela est réalisé en multipliant la matrice du système par une matrice représentant un opérateur spectralement équivalent à son inverse. Ceci peut être vu Figure 7, où le numéro de conditionnement de la matrice du système de la formulation symmétrique du problème direct de l'EEG avec et sans préconditionement est montré en fonction de la taille du maillage (h).

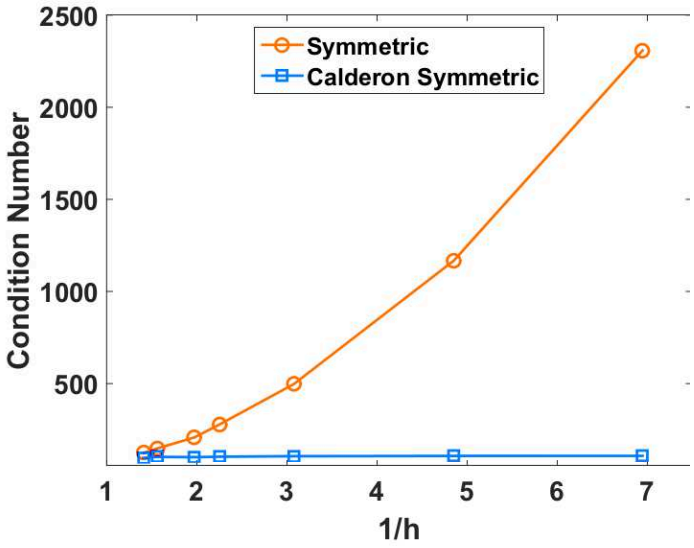

Figure 7: Condition Number with respect to the mesh refinement.

Une simulation numérique, Figure 8, d'un cas réaliste montre que le préconditionnement permet d'obtenir la solution du problème direct avec un nombre d'itérations bien moindre.

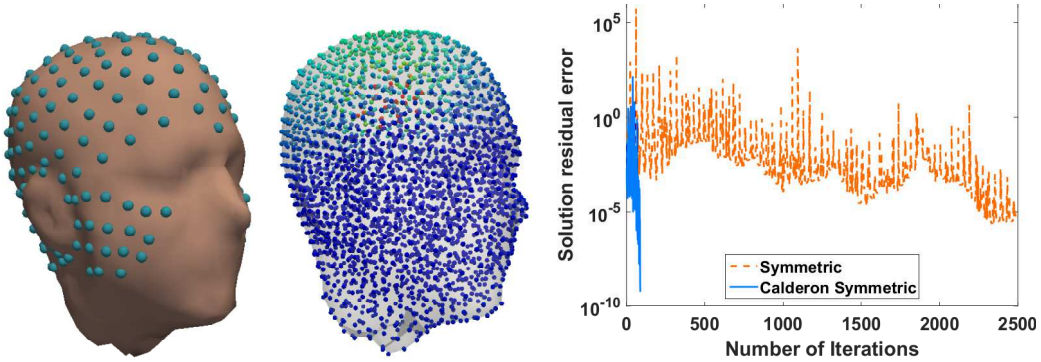

(a) Modèle de tête et électrodes. (b) Potentiel électrique calculé. (c) Convergence du solveur itératif.

Figure 8: Résultats pour un modèle de tête réel.

Un préconditionneur de type Calderon est proposé pour l'équation intégrale du champ électrique (EFIE) lorsque la structure considérée est une courbe de l'espace tridimensionnel. Le préconditioneur proposé utilise l'opérateur intégral classique de simple couche et une version modifié en une dimensions afin de prendre en compte les effet de bord lorsque la structure n'est pas fermée. La technique de préconditionement proposée permet de construire une matrice de système ayant un numéro de conditionement stable avec l'accroissement de la densité du maillage dans le cas de courbes fermées. Pour des courbes ouvertes, le numéro de conditionement augmente mais seulement de manière logarithmique c'est à dire en $O\left(\log(1/h)\right)$ où h est le paramètre du maillage. Ce résulat est montré Figure 9.

L'idée de modéliser les structures fines avec des courbes est étendue au milieu cérébral. Le chapitre présente ainsi une nouvelle équation intégrale pour le problème direct de l'EEG afin de prendre en compte les caractéristiques anisotropes des fibres constituant la matière blanche. La Figure 10 permet de vérifier que lorsque la densité du maillage augmente, l'erreur relative de la solution proposée, par rapport à une solution aux éléments finis choisie comme référence, diminue. Ceci confirme la validité de l'approche présentée.

Le dernier chapitre présente l'impact de l'utilisation d'un solveur direct lors de la

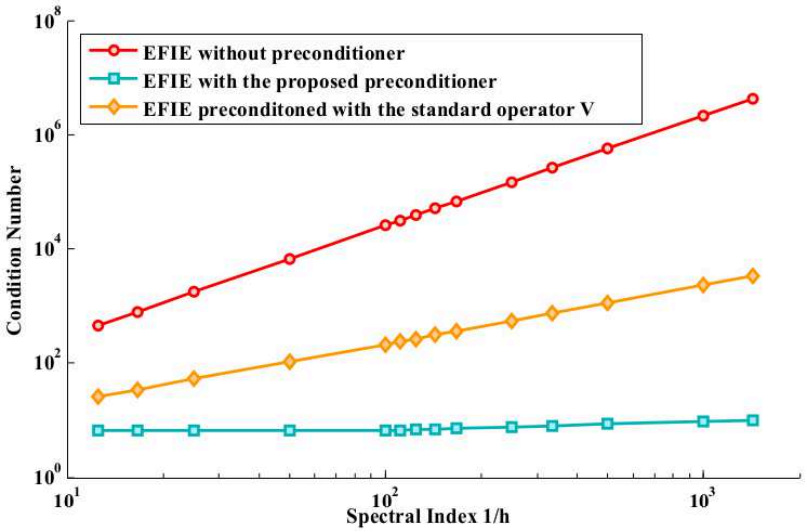

Figure 9: Nombre de conditionnement de la matrice de system de l'EFIE ($\mathbf{Z}$) non préconditioné et préconditioné avec l'opérateur simple couche non modifié ($\mathbf{V}$) et modifié ($\widetilde{\mathbf{V}}$) pour une courbe ouverte.

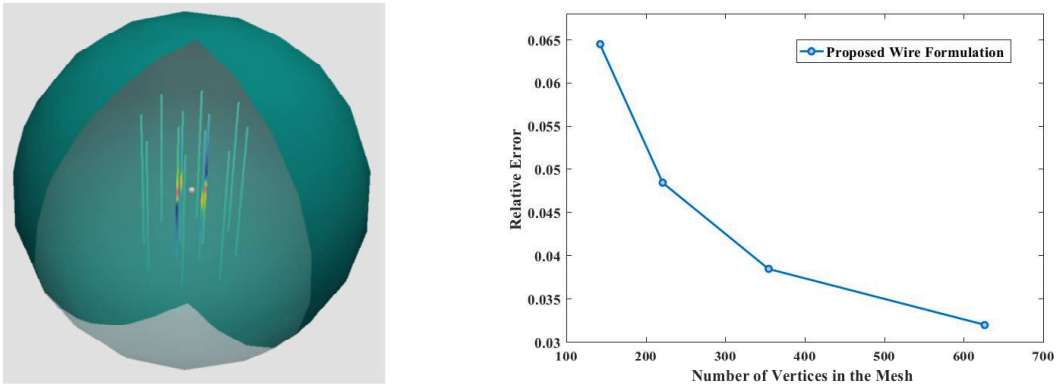

(a) La sphère blanche représente la source dipolaire, les couleurs montrent l'amplitude du courant sur les cylindres représentant la matière blanche.

(b) Erreur relative lors de l'accroissement du nombre d'inconnues par rapport à une solution FEM an présence de 12 fibres.

Figure 10: Simulation de 12 fibres anisotropes dans un modèle de tête homogène simple couche.

résolution du problème direct de l'EEG. Le solveur utilisé permet de passer d'une complexité algorithmique $O(N^3)$ lors de la résolution directe du système à $O(N^{1.5})$, avec N le nombre d'inconnues du système. Puisque la résolution du problème inverse de l'EEG nécessite de résoudre de nombreuses fois le problème direct de l'EEG, l'avantage d'un solveur rapide direct se situe non seulement lors du calcul de la solution au problème mais

aussi lors de la reconstruction des sources cérébrales de l'EEG. Le chapitre présente des résultats préliminaires sur l'impact d'un tel solveur lors de la modélisation de la propagation des sources cérébrales.

Contents

List of Figures

Chapter 1

Introduction

This chapter shows how from Maxwell's equations we can derive the electroencephalography (EEG) forward problem. It explains how this problem can be solved using integral equations and the boundary element method. The chapter will show the necessity of improving currently available solutions of the EEG forward problem to take into account realistic conductivity profiles and in particular the anisotropy properties of the head media with in the boundary element method framework. For handling such properties fast solutions are also a must. This is why we will introduce preconditioning techniques and fast algorithms.

1.1 Recording the Brain Activity

While the euphoric effect of poppy plant has been known by the Sumerian since at least 4000 BC, one must wait until the fourth century BC for Hippocrates to deny the divine origin of epilepsy and to attribute it to brain malfunction [60]. Since then, the advances in medicine and technology have greatly improved our current knowledge of the brain. In particular, the work of du Bois Reymond and von Helmholtz, gave birth to what is now known as electro-physiology [81]. It is the electrochemical activity of the neurons which is responsible for the potential that can be recorded using ElectroEncephaloGraphy (EEG) [72]. This neuro-imaging tool is used in many medical applications such as the

presurgical evaluation of the epileptic focus [82, 71], the study of strokes, or the design of Brain Computer Interfaces (BCIs) [59].

Neurons, or nerve cells, are mainly located in the neocortex (the gray matter), a 2 to 5 mm thick folded layer that surrounds the white matter in the cerebrum [72]. Neurons process and transmit electrochemical signals through their synapses. Typical neurons are made of a cell body, dendrites and axons. In the white matter, axons connect the neurons together. The synaptic potential generated by groups of neurons are the so-called generator of the electric field that EEG (and Magnetoencephalography -MEG-) can measure [72]. Because of the dynamics behind the EEG sources, EEG temporal resolution is very good (around 1 milliseconds) hence it can be used for real time applications [59]. EEG recorded on the scalp of patients or with intracranial electrodes records the activity of groups of neurons. It is possible, by placing micro electrodes or meso-electrodes in the cortex, to record the activity of a single neuron. However, this operation (as well as intracranial EEG) remains invasive and cannot be a long term solution since the glial cells soon form a scar around the electrode that mutes the electrical activity [84]. As a consequence, EEG if not invasive, has a low spatial resolution. However, the anatomy of the brain can be imaged using other tools such as Magnetic Resonance Imaging (MRI) or Positron Emission Tomography (PET). The physical quantity recorded by MRI is the relaxation time of water nucleus in the body exposed to magnetic field [86]. Diffusion tensor MRI (DTI) can be used to infer the conductivity of the head tissues from the water diffusion tensor data [98]. Positron Emission Tomography also provides a way to image the brain by labelling molecules with radioisotopes. Functional MRI or Near Infrared spectroscopy (NIRS) give an insight of the brain dynamics by recording the change of oxygen concentration in the blood that circulates in the brain [73], however the achieved temporal resolution is not as high as the one of EEG. The rational behind this is that these neuroimaging techniques only record metabolic changes linked to the brain activity. Those phenomena are slow (with re-

spect to the electric activity) and therefore the achieved temporal resolution is limited. The ideal neuroimaging technique would combine the high spatial resolution of MRI and the high temporal resolution of EEG and MEG.

Locating the brain sources responsible for the EEG measured potential is still possible by solving the so called *EEG inverse source problem* [37] [68]. Since the number of EEG signal generators is much greater than the number of electrodes, this problem is ill-posed. It is therefore necessary to make assumptions on the underlying sources. First of all an accurate propagation model from the sources to the sensor must be available. This problem is known as the *EEG forward problem* [43]. In solving the EEG forward problem, since the head is topologically equivalent to a sphere, spherical head model have historically been used. They have the advantage that their analytical solution is known [26]. However, it has been shown that the solution to the inverse problem is greatly improved if realistic head models are used [21] [3]. These accurate models can be recovered using MRI data. Another important information to provide is the correct conductivity of head tissues, in particular their anisotropy and inhomogenity. Indeed, it was shown that neglecting the anisotropic properties of the skull and the white matter increases the error when performing source imaging [39] [41] [61] [104]. This data, as mentioned previously, can be obtained by using DTI. Then, assuming that the anatomical information is known, what are the equations governing the phenomena? A partial answer is given by Maxwell equations and the derived equation is a partial differential equation that, in quasi static, fits the more general framework of elliptic problems. The work carried out in this thesis focuses on developing new tools for solving the EEG forward problem leveraging mathematical concepts developed in the framework of boundary elements methods.

1.2 From Maxwell's Equations to the EEG Forward Problem

As in any electromagnetic phenomena, the governing equations are the Maxwell's equations. These equations relate the electric field, the magnetic field and their sources i.e. charges and currents. They read

$$\nabla \cdot \mathbf{E} = \frac{\rho}{\epsilon} \tag{1.1a}$$

$$\nabla \cdot \mathbf{H} = 0 \tag{1.1b}$$

$$\nabla \times \mathbf{E} = -\mu \frac{\partial \mathbf{H}}{\partial t} \tag{1.1c}$$

$$\nabla \times \mathbf{H} = \mathbf{J} + \epsilon \frac{\partial \mathbf{E}}{\partial t} \tag{1.1d}$$

where $\mathbf{E}$ and $\mathbf{H}$ are respectively the electric field and the magnetizing field, to which we can respectively associate the electric field displacement field $\mathbf{D} = \epsilon \mathbf{E}$ and the magnetic field $\mathbf{B} = \mu \mathbf{H}$. The constants ϵ and μ are the electric permittivity and the magnetic permeability of the medium. In the above equations, $\mathbf{J}$ is the electric current density and ρ the charge density. They are related through the charge conservation law

$$\nabla \cdot \mathbf{J} = -\frac{\partial \rho}{\partial t} \tag{1.2}$$

Moreover, the Ohm's law gives

$$\mathbf{J} = \sigma \mathbf{E} + \mathbf{J_0} \tag{1.3}$$

where $\mathbf{J_0}$ is the initial current density (impressed) and σ the conductivity of the medium. In case of isotropic conductivity, σ is a scalar.

The frequency of the recorded brain electric phenomena is well below 1000 Hz [72]. In this situation, the temporal derivative can be neglected and as a consequence, the electric

field and the magnetic field decouple. We then obtain from (1.1c)

$$\nabla \times \mathbf{E} = 0 \Leftrightarrow \mathbf{E} = -\nabla V \tag{1.4}$$

with V the electric potential. This is this physical quantity that is measured when recording an EEG. We can derive the associated equation using the quasi static approximation of (1.1d)

$$\nabla \times \mathbf{H} = \mathbf{J}, \tag{1.5}$$

and the Ohm's law (1.3), so that (1.5) becomes

$$\nabla \times \mathbf{H} = \sigma \mathbf{E} + \mathbf{J_0}. \tag{1.6}$$

Inserting the result of (1.4), we get

$$\nabla \times \mathbf{H} = -\sigma \nabla V + \mathbf{J_0} \tag{1.7}$$

Applying the divergence operator we finally obtain

$$\nabla \cdot \sigma \nabla V = \nabla \cdot \mathbf{J_0}. \tag{1.8}$$

This partial differential equation is the Poisson equation. In order to find a unique solution (up to a constant) we must enforce boundary conditions. In the context of EEG, the potential must be continuous through the interfaces of the different domain of the head media as well as its conormal derivative. Then denoting with

$$\gamma_0^{\pm} u = u_{|\Gamma^{\pm}} \tag{1.9}$$

the outer and inner trace of a function u defined in a domain Ω of boundary Γ and

$$\gamma_1^{\pm} u = \vec{n} \cdot \gamma_0^{\pm} \sigma \nabla u \tag{1.10}$$

its conormal derivative [92], those boundary conditions read

$$\begin{cases} \gamma_0^+ V = \gamma_0^- V \\ \gamma_1^+ V = \gamma_1^- V \end{cases} \tag{1.11}$$

The partial differential equation (1.8) together with the boundary conditions (1.11) form the EEG forward problem. If, as desired, realistic head shapes are to be taken into account, only numerical solutions exist. In the last decades, many solutions have been proposed [43]. Finite Elements Methods (FEM) [17, 43, 61, 64, 103, 105] and Finite Difference Methods (FDM) [43, 99] can handle both inhomogeneous and anisotropic conductivity profile naturally since they discretize the whole volume. They however have the disadvantage of being based on differential operators and as such are intrinsically ill-conditioned. Boundary Element methods [54] are very accurate and only require the discretization of the interfaces of the conductor. However, they can only handle isotropic conductivity profiles even if some steps have been taken towards the handling of anisotropy in [74] and [108]. Chapter 2 of this thesis is dedicated to the introduction of a new boundary element method that can handle anisotropies. In Chapter 5, a specific boundary element method for handling white matter anisotropy is also presented. In the following section, we present the general strategy for solving partial differential equation with the boundary element method.

1.3 Integral Equations for Elliptic Problems

It is easy to see that the differential operator $\nabla \cdot \sigma \nabla$ can be simplified into the Laplacian operator Δ when σ is isotropic. From Maxwell equations, we can also derive other equations for other types of electromagnetic problems, like, for example, the Helmholtz equation $\nabla \cdot \nabla u + k^2 u = f$. Actually, away from resonance, all the differential operators mentioned are elliptic differential operators for which we can prove the existence and uniqueness of the solution [94]. The following discussion will then be oriented towards the treatment of this class of operators and the EEG forward problem will be treated as an applicative case.

In a domain Ω with boundary Γ, we consider the following general linear elliptic differential operator

$$Lu = \nabla \cdot \mathbf{A}\nabla u + \mathbf{b} \cdot \nabla u + cu \tag{1.12}$$

with $\mathbf{A}$ a symmetric positive definite matrix and $\mathbf{b}$ a vector. Note that throughout the text, bold characters will indicate vector or matrix parameters (in capital letters). In the EEG forward problem, $\mathbf{A} = \sigma$, $\mathbf{b} = 0$ and $c = 0$.

The variational form of the problem $Lu = f$ is given by

$$\langle Lu, g \rangle = \langle f, g \rangle \tag{1.13}$$

where $\langle \cdot, \cdot \rangle$ is the L_2 duality product:

$$\langle w, v \rangle = \int_\Omega w(r)v(r)dr \quad w, v \in L^2(\Omega) \tag{1.14}$$

The two formulations are equivalent [94]. We recall that $L^2(\Omega)$ is the space of all square integrable functions on Ω.

1.3.1 Function Spaces for the Solution

The solution of $Lu = f$ requires that u is twice differentiable. When formulating the variational problem (1.13), this condition can be weakened by requiring u to be only once derivable. In this case (1.13) is often referred to as *weak formulation*. However for functions in L^2, it is not possible to define the classical pointwise derivative everywhere, one needs to resort to generalized derivative, denoted D^α and defined using integration by part, where α is the order of derivation. We then need to introduce the following function space [4]

Definition 1.1. For a bounded domain $\Omega \subset \mathbf{R}^d$, the Sobolev space of order $s \geq 0$ $H^s(\Omega)$ is defined as

$$H^s(\Omega) = \{u \in L_2(\Omega) | D^\alpha u \in L^2(\Omega), \forall |\alpha| \leq s\}.$$

This allows to conclude that the solution of (1.13) is in H^1, the space of function square integrable and whose first (generalized) derivative is also square integrable.

The Sobolev spaces $H^s(\Omega)$ are Hilbert spaces. For $s < 0$, they are defined by duality with respect to the L_2 inner product. Denoting X' the dual of X, a bounded and linear space, we have

$$(H^s(\Omega))' = H^{-s}(\Omega).$$

They are also defined for s non integer. In particular, if we want to define boundary integral equations, we need to define Sobolev spaces on $\partial\Omega = \Gamma$. This can be done assuming a certain smoothness of Ω. The smoothness of the domain will determine the smoothness of a function defined on its boundary. (For a rigorous definition of the *smoothness* of a domain we refer the reader to [92], informally it refers to the continuity and derivability properties of the function that describes the boundary). Since we are concerned only with functions at most in $H^1(\Omega)$, the following trace theorem holds [94]

Theorem 1.1. *If $\Omega \subset \mathbf{R}^{\mathrm{d}}$ is a Lipschitz domain with $\partial\Omega = \Gamma$, then for $\frac{1}{2} < s \leq 1$, the interior trace operator*

$$\gamma_0^- : H^s(\Omega) \to H^{s-1/2}(\Gamma)$$

is bounded satisfying

$$||\gamma_0^- v||_{H^{s-1/2}(\Gamma)} \leq c||v||_{H^s(\Omega)}.$$

This remains true for $s \in \left\{\frac{1}{2}, \frac{3}{2}\right\}$ [94]. Since the EEG forward problem enforces boundary conditions using the trace operator, we will always assume that Ω is a Lipschitz domain. Definition of the geometry as well as an example of a non Lipschitz domain are shown Figure 1.1.

We are now equipped with the correct topology to solve elliptic boundary value problems, in particular the EEG forward problem. The next section will introduce fundamental solutions and the representation theorem.

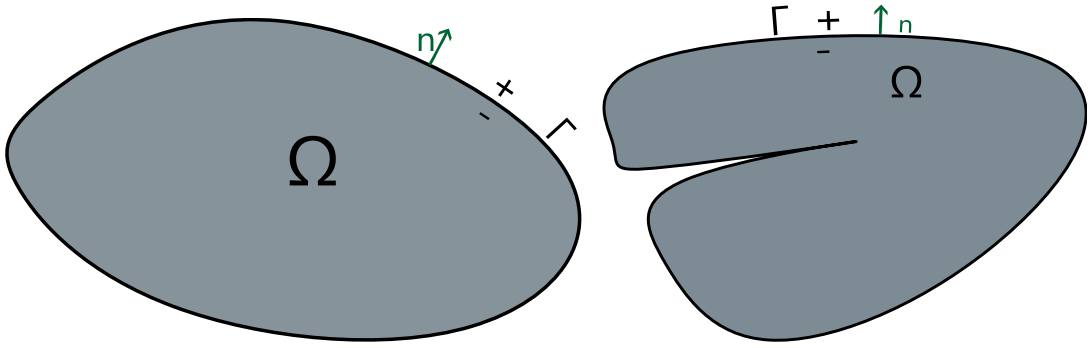

(a) Lipschitz domain (b) Non-lipschitz domain

Figure 1.1: The figure on the left (a), shows a Lipschitz domain while the domain in the right figure is not a Lipschitz domain. The notations employed for defining the geometry are also shown in both figures.

1.3.2 Fundamental Solutions

We call fundamental solution of the equation $Lu = f$ a function $G(\mathbf{r})$ which is the solution of $Lu = \delta_0$. This solution is also often called *Green's function*. It depends on the dimension of the problem. We have [92]

$$G(\mathbf{r}) = \begin{cases} \dfrac{e^{\langle \mathbf{b},\mathbf{r}\rangle}}{2\pi\sqrt{\det \mathbf{A}}} \log\left(\dfrac{1}{||\mathbf{r}||_A}\right) & \text{for } d = 2 \text{ and } \lambda = 0 \\ \dfrac{e^{\langle \mathbf{b},\mathbf{r}\rangle}}{4\sqrt{\det \mathbf{A}}} i H_0^{(1)}\left(i\lambda||\mathbf{r}||_A\right) & \text{for } d = 2 \text{ and } \lambda \neq 0 \\ \dfrac{1}{4\pi\sqrt{\det \mathbf{A}}} \dfrac{e^{\langle \mathbf{b},\mathbf{r}\rangle - \lambda||\mathbf{r}||_A}}{||\mathbf{r}||_A} & \text{for } d = 3 \end{cases} \tag{1.15}$$

with $\lambda = i\sqrt{|c + ||\mathbf{b}||_A^2|}$, and $||\mathbf{x}||_A = \langle \mathbf{x}, \mathbf{x}\rangle_{\mathbf{A}}^{1/2}$ where $\langle \mathbf{x}, \mathbf{y}\rangle_{\mathbf{A}} = \mathbf{x}^T \mathbf{A}^{-1} \mathbf{y}$. Moreover in the above equation, $H_0^{(1)}$ denotes the Hankel function of first kind and order 0. The fundamental solution is singular for $\mathbf{r} = 0$ and analytical when $\mathbf{r} \neq 0$. We choose to work with Green's functions that satisfy the following radiation condition at infinity,

$$\begin{cases} \lim\limits_{r \to +\infty} r|G(r)| < \infty \\ \lim\limits_{r \to +\infty} r \dfrac{\partial |G(r)|}{\partial r} = 0 \end{cases}$$

which means that the solution vanishes at infinity.

For the EEG forward problem (1.8), the Green's function is given by

$$G(\mathbf{r}) = \frac{1}{4\pi\sqrt{\det\sigma}}\frac{1}{\sqrt{\sigma^{-1}\mathbf{r}\cdot\mathbf{r}}}. \tag{1.16}$$

This is the fundamental solution that we will use to introduce a boundary element method that takes into account the anisotropy of the head media. The common BEM formulations that assume an isotropic conductivity are using the fundamental solution of the Laplace problem for which the Green's function is

$$G(\mathbf{r}) = \frac{1}{4\pi||\mathbf{r}||} \tag{1.17}$$

For the Helmholtz equation it is

$$G(\mathbf{r}) = \frac{e^{-ik||\mathbf{r}||}}{4\pi||\mathbf{r}||} \tag{1.18}$$

This solution will be used in the fifth Chapter where we study the wire electric field integral equation. In this chapter, we will also deal with operators derived from the solution of the Laplace Problem in 2D. The fundamental solution in this case is given by

$$G(\mathbf{r}) = -\frac{1}{2\pi}\log||\mathbf{r}||. \tag{1.19}$$

By integrating on the domain Ω, we can obtain a solution to the equation $Lu = f$ using the fundamental solutions

$$u(\mathbf{r}) = -\int_{\Omega} G(\mathbf{r}-\mathbf{r}')f(\mathbf{r}')d\mathbf{r}' \tag{1.20}$$

Note that this solution does not respect the boundary conditions on Γ and an additional term should be added to enforce them. This term should satistify the homogeneous equation $Lu = 0$. Solutions to this equation are called *L-harmonic*. Actually for solving the EEG forward problem, the key point lies in finding this harmonic function.

1.3.3 Representation Theorem

Considering, here and in the following of this manuscript, that the normal $\vec{n}$ of the boundary Γ is oriented towards the exterior of the domain Ω, the divergence theorem gives, for all $f \in H^1(\Omega)$

$$\int_\Omega \nabla \cdot f(\mathbf{r}) dr = \int_\Gamma \vec{n} \cdot \gamma_0^- f(\mathbf{r}) d_\Gamma \mathbf{r} \tag{1.21}$$

We then have for $u \in H^2(\Omega)$ and $v \in H^1(\Omega)$ the Green's first formula [92]

$$\int_\Omega \nabla \cdot \mathbf{A} \nabla u(\mathbf{r}) v(\mathbf{r}) d\mathbf{r} = -\int_\Omega \mathbf{A} \nabla u(\mathbf{r}) \cdot \nabla v(\mathbf{r}) d\mathbf{r} + \int_\Gamma \mathbf{A}\vec{n} \cdot \nabla u(\mathbf{r}) v(\mathbf{r}) d_\Gamma \mathbf{r} \tag{1.22}$$

Exchanging u and v we obtain

$$\int_\Omega \nabla \cdot \mathbf{A} \nabla v(\mathbf{r}) u(\mathbf{r}) d\mathbf{r} = -\int_\Omega \mathbf{A} \nabla v(\mathbf{r}) \cdot \nabla u(\mathbf{r}) d\mathbf{r} + \int_\Gamma \mathbf{A}\vec{n} \cdot \nabla v(\mathbf{r}) u(\mathbf{r}) d_\Gamma \mathbf{r} \tag{1.23}$$

Taking the difference of the two equations, we get the second Green's formula [92]

$$\begin{aligned} \int_\Omega \nabla \cdot \mathbf{A} \nabla u(\mathbf{r}) v(\mathbf{r}) d\mathbf{r} - \int_\Omega u(\mathbf{r}) \nabla \cdot \mathbf{A} \nabla v(\mathbf{r}) d\mathbf{r} = \\ \int_\Gamma \mathbf{A}\vec{n} \cdot \nabla u(\mathbf{r}) v(\mathbf{r}) d_\Gamma \mathbf{r} - \int_\Gamma \mathbf{A}\vec{n} \cdot \nabla v(\mathbf{r}) u(\mathbf{r}) d_\Gamma \mathbf{r} \end{aligned} \tag{1.24}$$

Now, let's choose $u(\mathbf{r}) = G(\mathbf{r} - \mathbf{r}')$, the fundamental solution for the operator L and $v = \phi \in H^1(\Omega)$ the unknown function. We obtain:

$$\begin{aligned} \int_\Omega \nabla \cdot \mathbf{A} \nabla G(\mathbf{r} - \mathbf{r}') \phi(\mathbf{r}) d\mathbf{r} - \int_\Omega G(\mathbf{r} - \mathbf{r}') \nabla \cdot \mathbf{A} \nabla \phi(\mathbf{r}) d\mathbf{r} = \\ \int_\Gamma \mathbf{A}\vec{n} \cdot \nabla G(\mathbf{r} - \mathbf{r}') \phi(\mathbf{r}) d_\Gamma \mathbf{r} - \int_\Gamma \mathbf{A}\vec{n} \cdot \nabla \phi(\mathbf{r}) G(\mathbf{r} - \mathbf{r}') d_\Gamma \mathbf{r} \end{aligned} \tag{1.25}$$

$$\begin{aligned} \Leftrightarrow \quad \int_\Omega [L - \mathbf{b} \cdot \nabla - c] G(\mathbf{r} - \mathbf{r}') \phi(\mathbf{r}) d\mathbf{r} - \int_\Omega G(\mathbf{r} - \mathbf{r}') \left[L - \mathbf{b} \cdot \nabla - c\right] \phi(\mathbf{r}) d\mathbf{r} = \\ \int_\Gamma \mathbf{A}\vec{n} \cdot \nabla G(\mathbf{r} - \mathbf{r}') \phi(\mathbf{r}) d_\Gamma \mathbf{r} - \int_\Gamma \mathbf{A}\vec{n} \cdot \nabla \phi(\mathbf{r}) G(\mathbf{r} - \mathbf{r}') d_\Gamma \mathbf{r} \end{aligned} \tag{1.26}$$

$$\begin{aligned} & \phi(\mathbf{r}') - \int_\Omega \left[\mathbf{b}\cdot\nabla + c\right] G(\mathbf{r}-\mathbf{r}')\phi(\mathbf{r})d\mathbf{r} - \int_\Omega G(\mathbf{r}-\mathbf{r}')f(\mathbf{r})d\mathbf{r} \\ \Leftrightarrow \quad & + \int_\Omega G(\mathbf{r}-\mathbf{r}')\left[\mathbf{b}\cdot\nabla + c\right]\phi(\mathbf{r})d\mathbf{r} = \\ & \int_\Gamma \mathbf{A}\vec{n}\cdot\nabla G(\mathbf{r}-\mathbf{r}')\phi(\mathbf{r})d_\Gamma\mathbf{r} - \int_\Gamma \mathbf{A}\vec{n}\cdot\nabla\phi(\mathbf{r})G(\mathbf{r}-\mathbf{r}')d_\Gamma\mathbf{r} \end{aligned} \tag{1.27}$$

$$\begin{aligned} & \phi(\mathbf{r}') - \int_\Omega \left[\mathbf{b}\cdot\nabla\right] G(\mathbf{r}-\mathbf{r}')\phi(\mathbf{r})d\mathbf{r} - \int_\Omega G(\mathbf{r}-\mathbf{r}')f(\mathbf{r})d\mathbf{r} + \int_\Omega G(\mathbf{r}-\mathbf{r}')\left[\mathbf{b}\cdot\nabla\right]\phi(\mathbf{r})d\mathbf{r} = \\ \Leftrightarrow \quad & \int_\Gamma \mathbf{A}\vec{n}\cdot\nabla G(\mathbf{r}-\mathbf{r}')\phi(\mathbf{r})d_\Gamma\mathbf{r} - \int_\Gamma \mathbf{A}\vec{n}\cdot\nabla\phi(\mathbf{r})G(\mathbf{r}-\mathbf{r}')d_\Gamma\mathbf{r} \end{aligned} \tag{1.28}$$

In the case of interests in this thesis $\mathbf{b} = 0$ which gives

$$\phi(\mathbf{r}') = \int_\Omega G(\mathbf{r}-\mathbf{r}')f(\mathbf{r})d\mathbf{r} + \int_\Gamma \mathbf{A}\vec{n}\cdot\nabla G(\mathbf{r}-\mathbf{r}')\phi(\mathbf{r})d_\Gamma\mathbf{r} - \int_\Gamma \mathbf{A}\vec{n}\cdot\nabla\phi(\mathbf{r})G(\mathbf{r}-\mathbf{r}')d_\Gamma\mathbf{r} \tag{1.29}$$

$$\Leftrightarrow \phi(\mathbf{r}') = \int_\Omega G(\mathbf{r}-\mathbf{r}')f(\mathbf{r})d\mathbf{r} + \int_\Gamma \gamma_1^- G(\mathbf{r}-\mathbf{r}')\phi(\mathbf{r})d_\Gamma\mathbf{r} - \int_\Gamma \gamma_1^-\phi(\mathbf{r})G(\mathbf{r}-\mathbf{r}')d_\Gamma\mathbf{r} \tag{1.30}$$

which is known as the Green's representation theorem [92]. It shows that the solution ϕ of the differential equation $Lu = f$ is determined only by its boundary values. The following operators

$$S_\Omega\psi(r) = \int_\Gamma G(\mathbf{r}-\mathbf{r}')\psi(\mathbf{r}')d_\Gamma\mathbf{r}' \quad S\psi : H^{-1/2}(\Gamma) \to H^1(\Omega) \tag{1.31}$$

and

$$D_\Omega\phi(r) = \int_\Gamma \gamma_1 G(\mathbf{r}-\mathbf{r}')\phi(\mathbf{r}')d_\Gamma\mathbf{r}' \quad D\phi : H^{1/2}(\Gamma) \to H^1(\Omega) \tag{1.32}$$

arise naturally in (1.30). We can show that [92, Theorem 3.1.1]

$$LS\psi = LD\phi = 0 \tag{1.33}$$

In other words, we can build a $L-$harmonic function using the operators S and D. This property will be used in Chapter 2 to build a solution for the anisotropic EEG forward problem. Since we are interested in building a harmonic function given Neuman and Dirichlet

data, we recall the following relationships and introduce the single layer operator S, the double layer operator D, the adjoint double layer operator D^*, and the hypersingular operator N.

$$\begin{aligned}
\gamma_0^{\pm} S_\Omega \psi(\mathbf{r}) \quad &= \int_\Gamma G(\mathbf{r}-\mathbf{r}')\psi(\mathbf{r}')d\mathbf{r}' && \text{(1.34a)}\\
&= S\psi(\mathbf{r}), \quad S\psi : H^{-1/2}(\Gamma) \to H^{1/2}(\Gamma)\\
\gamma_0^{\pm} D_\Omega \phi(\mathbf{r}) \quad &= \pm\frac{1}{2}\phi(r) + \int_\Gamma \gamma_1^{\pm} G(\mathbf{r}-\mathbf{r}')\phi(\mathbf{r}')d\mathbf{r}' && \text{(1.34b)}\\
&= \pm\frac{1}{2}\phi(r) + D\phi(\mathbf{r}), \quad D\phi : H^{1/2}(\Gamma) \to H^{1/2}(\Gamma)\\
\gamma_1^{\pm} S_\Omega \psi(\mathbf{r}) \quad &= \mp\frac{1}{2}\psi(\mathbf{r}) + \int_\Gamma \gamma_1^{\pm} G(\mathbf{r}-\mathbf{r}')\psi(\mathbf{r}')d\mathbf{r}' && \text{(1.34c)}\\
&= \mp\frac{1}{2}\phi(\mathbf{r}) + D^*\psi(\mathbf{r})d\mathbf{r}', \quad D^*\psi : H^{-1/2}(\Gamma) \to H^{-1/2}(\Gamma)\\
\gamma_1^{\pm} D_\Omega \phi(\mathbf{r}) \quad &= \gamma_1^{\pm} \int_\Gamma \gamma_1^{\pm} G(\mathbf{r}-\mathbf{r}')\phi(\mathbf{r}')d\mathbf{r}' && \text{(1.34d)}\\
&= N\phi(\mathbf{r}), \quad N\phi : H^{1/2}(\Gamma) \to H^{-1/2}(\Gamma).
\end{aligned}$$

Using the Green's function for the Laplace equation in 3D, those operators are the operators we find in the common BEM formulations of the EEG forward problem as given in [54] for example. They are derived using the representation theorem (1.30) and the boundary conditions (1.11).

The operators S is elliptic, D and D^* are compact operators, and N is a bounded first order operator [92]. We will use these properties for deriving a preconditioner for the symmetric EEG formulation in Chapter 4 and a preconditioner for the wire electric field integral equation in Chapter 5.

1.4 Discretization

A strategy to solve a differential equation is to resort to a variational formulation as stated in the beginning of section 1.3. Consider the following equation

$$Bu = f$$

where B is a differential operator $B : X \to Y'$. By multiplying with a test function $v \in Y$ and integrating on $\partial\Omega$, we get the following variational formulation

$$\langle v, Bu \rangle = \langle v, f \rangle$$

In many situations this equation can only be solved numerically. This means that the geometry must first be discretized into simple elements. On this elements, we define the basis and testing functions used to discretize the unknown and test the equation. In the previous section, we showed that the original differential equation could be turned into a boundary integral equation. As a consequence, we just need to discretize the surface of the considered domain. Even if quadrilateral elements could be used, we will always use triangular elements to discretize the geometry. We call *mesh* $\mathcal{M}_\Omega$ of the surface Γ the sets of triangles $\{t_i\}_{i=1}^{N_t}$, vertices $\{v_i\}_{i=1}^{N_v}$, and edges that constitute the discrete approximation of the surface. We call *mesh parameter* (or *mesh width*) the maximum length of the edges that constitute the elements of the mesh. Here and in the following, this parameter will be denoted with h. Figure 1.2 shows a surface and an associated mesh.

We denote with $X_h = span\{\phi_h\}_{k=1}^{M} \subset X$ and $Y_h = span\{\psi_h\}_{k=1}^{N} \subset Y$ the finite dimensional spaces of functions associated to X and Y. The discretization process leads to look for $u_h = \sum_{i=1}^{M} \alpha_i \phi_i$. The standard Galerkin approach is to expand and test the equation with the same set of functions. However, the convergence of the discrete solution u_h towards the solution u of the variational formulation is ensured in this case only if $Y' = X'$. In the general case, $||u - u_h|| \xrightarrow[h\to 0]{} 0$ if the set of testing function is chosen in the

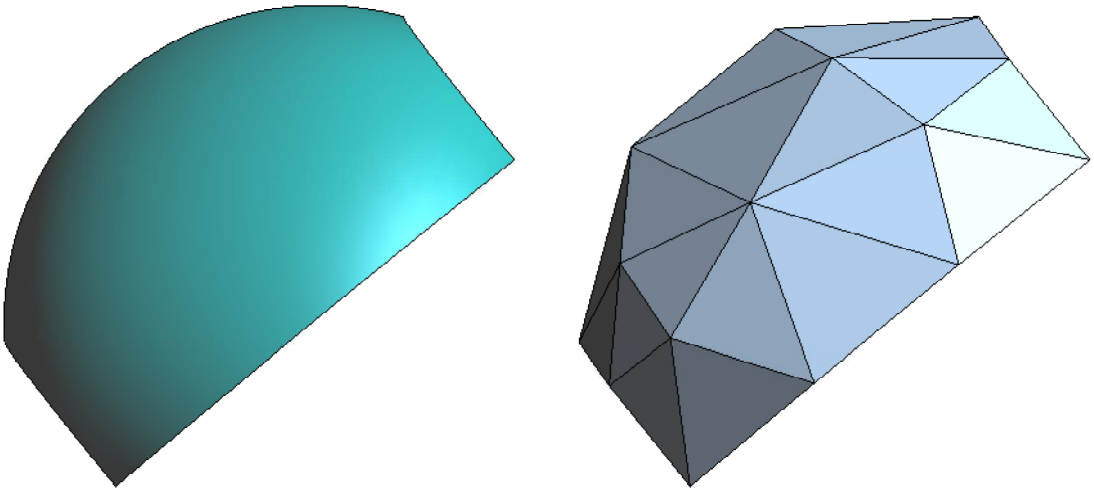

(a) (b)

Figure 1.2: A Lipschitz surface (a), and an example of mesh of this surface (b).

dual of the range of the operator [94], i.e. Y''. Since we deal with Hilbert spaces, we have $Y'' = Y$. Therefore, the testing should be done using functions in Y_h. Assuming moreover that $dim(X_h) = dim(Y_h)$ we get the following system matrix

$$\mathbf{Bu} = \mathbf{f}$$

with $\mathbf{u}_j = \alpha_j$, $\mathbf{f}_i = \langle \psi_h, f \rangle_{Y \times Y'}$ and

$$\mathbf{B}_{ij} = \langle \psi_h, B\phi_j \rangle_{Y \times Y'},$$

a square matrix (invertible if there is no null space).

Hence, the boundary elements method provides a way to build the solution using finitely many parameters. This can be done for example using polynomials functions defined on the elements of the mesh. The most common elements are the piecewise constant functions P_0 and piecewise linear functions P_1 illustrated in Figure 1.3.

Piecewise constant basis functions $P_0 = span\{P_{0i}\}_{i=1}^{N_t}$ are defined such that

$$P_{0i}(\mathbf{r}) = \begin{cases} 1 & \text{if } \mathbf{r} \in t_i \\ 0 & \text{elsewhere} \end{cases} \tag{1.35}$$

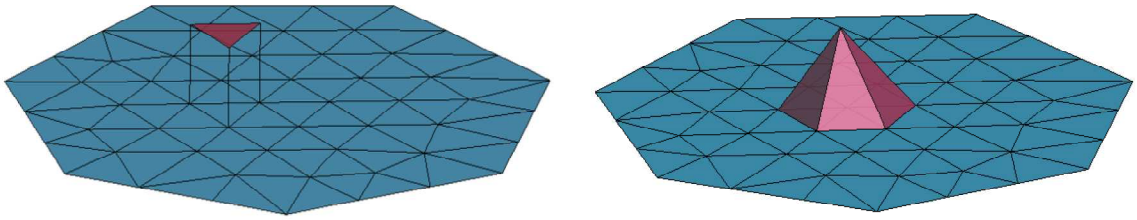

(a) Piecewise constant basis function P_0 (b) Piecewise linear basis function P_1

Figure 1.3: Example of two polynomial basis functions defined on a mesh.

The choice of the constant value could be different. This is however the choice we did throughout the text if not specified otherwise. Piecewise constant basis functions $P_1 = span\{P_{1i}\}_{i=1}^{N_v}$ are the set of functions defined on vertices such that their value is one on the corresponding vertex and linearly decrease to zero on the neighbouring vertex. Here also the choice of the value 1 could have been different. Their support is given by $\mu_{P_{1i}} = \{t_j | v_i \text{ is a vertex of } t_j\}$. We have $P_0 \subset H^{-1/2}(\Gamma)$ and $P_1 \subset H^{1/2}(\Gamma)$. These basis functions are used commonly in formulating the discrete system for the integral equations associated to the EEG forward problem. However, they are not sufficient to be able to test correctly (i.e. in the dual of the range of the operator) all the integral equation. This is why we will also resort in Chapter 2, 3, 4 and 5 to dual boundary elements, as proposed by [18] and as [88] did for the single and double layer integral formulations of the EEG forward problem.

1.5 Solving the Discrete System

After finding the integral equation, expanding the unknown in terms of finite boundary elements and testing it with the correct discrete functions, we end-up with a square linear system to solve. This system can be solved with different techniques. If the size of the matrix is small enough, direct inversion of the obtained system matrix is possible. However, in the context of EEG, to achieve high accuracy and since MRI images from which we can obtain the mesh [24] and [28] have a high resolution; the number of unknowns can reach the order of hundreds of thousands [3], preventing direct inversion. In this case, one must

resort to iterative methods such as conjugate gradient square methods. In this technique, the number of iterations needed to achieve a desired accuracy depends on the condition number of the matrix, the ratio of the maximum singular value over the minimum singular value of the matrix. These values depends on the integral operators involved.

In second kind integral equations (that is when the unknown function is also outside the integrand), the presence of the identity operator bounds the minimum singular value away from zero. If the other integral operator has a bounded maximum singular value then the overall operator has bounded minimum and maximum singular values. This is the case for the double layer and adjoint double layer EEG formulations : the involved operators are D and D^* which are compact operators and which have the property to have a bounded maximum singular value. However, in first kind integral equations (that is when the unknown function is only inside the integrand), the bounds on the minimum and maximum singular value cannot be enforced by the involved operator alone (it would otherwise be spectrally equivalent to an identity). This means that these integral equations will give rise to system matrices which are ill-conditioned. This is the case of the EEG symmetric formulation [54] that we will introduce in Chapter four. Nonetheless it is possible to build a stable system matrix by multiplying the ill-conditioned operator with an operator spectrally equivalent to its inverse. This technique is called *preconditionning*, it aims at achieving a stable condition number with respect to the mesh parameter. In Chapter 4 we propose a preconditioner for the EEG symmetric formulation.

Electroencephalography is well-known for its temporal resolution. However, when performing source imaging, the solution of the forward model must be computed several times. It would be very desirable to solve the forward problem as fast as possible. Fast direct solvers can also be used. Differently from Fast Multiple Method (FMM) or any Krylov subspace method, they do not store the system matrix in a linear complexity [62] but its *inverse*. This means that once this inverse is built, only one matrix-vector multiplication is

needed to obtain the solution, even if the dimensions of the system are large. This technique is therefore very promising for solving the EEG forward problem several times. In the last chapter, we present preliminary results on the impact of using a fast direct solver in solving the EEG forward problem.

1.6 Conclusion

This chapter presented a basic introduction to integral equations for the EEG forward problem and presented the challenges we have faced. It gives the reader the definitions and notations that will be used throughout the text. The fundamental steps for obtaining a numerical solution to this elliptic boundary problem were presented. We also discussed on the merits of the current formulations for the EEG forward problem. We showed that current BEM formulations do not handle anisotropies even if this parameter appears to be important in the literature. We will propose in Chapters 2 and 5 two new formulations for handling anisotropic conductivity profiles. The discussion on the function space, besides familiarizing the reader with them, also allowed to show that the usual discretization of the current integral EEG formulation does not abide by the spectral properties of the operators. We will discuss in Chapter 3 the effect of testing the equation in the dual of the range of the operators instead of using the usual Galerkin discretization. Finally, the section on the numerical solution of the obtained discrete system introduced the concept of preconditioning, that we will apply in Chapters 4 and 5.

Chapter 2

A New Integral Formulation for Handling Brain Anisotropies in the EEG Forward Problem

In the electroencephalography (EEG) forward problem (i.e. the computation of the electric potential at the scalp, knowing the electric current source configuration in the brain), it is often necessary to model the anisotropic conductivity profiles of the skull and of the white matter. These profiles, however, cannot be handled by standard surface integral formulations (Boundary Element Methods, BEMs). This chapter proposes a new surface integral formulation for the EEG forward problem that can handle anisotropic conductivity profiles. The main challenge resides in the fact that standard formulations for the isotropic case can leverage on the existence of a globally harmonic function satisfying the isotropic and homogeneous Poisson's equation in each head compartment. In the case of the anisotropic EEG forward problem, instead, a solution of the homogeneous Poisson's equation in one compartment will not be, in general, a solution of the homogeneous Poisson's equation in a different compartment of the head. To circumvent this problem, we opted in this work for an indirect formulation. This strategy has also the advantage of straightforwardly enabling the treatment of non-nested head compartments. Furthermore, a mixed discretization is employed to further improves the accuracy of the new formulation. A set of numerical results is presented to corroborate all theoretical treatments and to show

the impact of the proposed approach on both canonical and real case scenarios.

2.1 Introduction

Epileptic source localization from high resolution electroencephalographies (EEGs) is a fundamental step in the pre-surgical evaluation of focal epileptic patients that are refractory to pharmacological treatment and for whom surgical resection of the epileptic focus is considered [57, 83, 67, 32, 38]. In this brain imaging technique, starting from the electrical potential measured on the scalp, the brain current sources responsible for focal epilepsy are localized by solving an inverse source problem [37, 13, 35]. Solving this inverse problem requires the multiple solution of an EEG forward problem that provides, from known brain electrical current sources, the surfacic potential measured at the electrodes' locations [37, 43]. The inverse problem is ill-posed so that different source configurations can produce the same potential measure. As a consequence, the solution of the forward problem must be computed with the highest possible precision [31, 78, 3].

In solving the EEG forward problem, spherical head models have been historically used since analytic solutions are available for them [26, 106]. However, modern techniques rely on the use of realistic head models that require a numerical solution, but for which the accuracy of the forward EEG solution is largely improved [9, 21, 89, 102]. Several methods can be used for numerically solving the EEG forward problem, including Finite Difference [99] , Finite Element (FEM) [103] and Boundary Element methods (BEM) [44, 30, 54, 96]. Boundary Element methods have been quite popular given that they require only surfacic discretization of the brain layers when compared to the other two techniques that rely on volume discretizations. These methods however are not panacea given that, in their standard incarnations, they cannot handle anisotropic conductivity profiles. Indeed, correct modeling of anisotropic conductivity profiles is quite important given the influence of white matter and especially of the skull anisotropic conductivities on source

localization [61, 104, 41, 45, 69]. The reader should notice that anisotropic conductivity profiles can be naturally treated with FEM approaches although, as pointed out before, this would result in volumetric discretizations and thus a purely surfacic BEM method (with anisotropic modeling capabilities) would be highly desirable. Some steps in this direction have been presented in [75] where a hybrid surface volume scheme is presented but without obtaining a fully surfacic scheme given that the anisotropies are still treated in a volumetric way. Moreover, [108] proposed an interesting coordinate transform to handle a constant anisotropy of a single conducting body. No details, however, were provided for the multi compartments problem and the associated numerical solutions.

This chapter will propose a fully surfacic mixed discretized BEM formulation capable of handling constant piecewise homogeneous conductivity profiles including anisotropies for both nested and non-nested compartments. This has been obtained by leveraging on an indirect method strategy that, differently from standard approaches to obtain EEG Integral Equations, allows to maintain harmonicity properties also across different anisotropic media. Moreover, the work leverages on a mixed discretization strategy which abides by the mapping properties of all the operators involved and provides highly accurate solutions with minimal computational overhead.

The chapter is organized as follows: Section 2.2 describes background material and sets the notation. Section 2.3 presents the new anisotropic integral equation. Section 2.4 focuses on the BEM solution of the new formulation and introduces a mixed discretization to further improve its accuracy. Section 2.5 complements all the theoretical developments with numerical results that show the effectiveness of the newly proposed method in both canonical and real case scenarios.

2.2 Background and Notation

Consider a domain Ω divided into N non overlapping subdomains Ω_i with Lipschitz boundary $\Gamma_i = \partial_{\Omega_i}$ such that $\Omega = \bigcup_j^N \bar{\Omega}_i$. We further define $\Gamma_i = \bigcup_{j\in\omega_i} \Gamma_{ij}$, where $\omega_i = \{j \leq N+1 \quad | \quad \bar{\Omega}_i \cap \bar{\Omega}_j \neq \emptyset\}$ and $\Gamma_{ij} = \bar{\Omega}_i \cap \bar{\Omega}_j$. The normal $\vec{n}_{ij}$ to the interface Γ_{ij} is oriented from Ω_i to Ω_j with $i < j$. The index $N+1$ corresponds to the external domain. Figure 2.1 shows a general decomposition of Ω into subdomains. Standard EEG BEM formulations often make use of nested domains [54], so that when a three layers geometry is chosen, the compartments represents the brain, the skull and the scalp. In this particular case, $\Gamma_i = \Gamma_{i,i-1} \cup \Gamma_{i,i+1}$. We define the traces of a function g on a boundary Γ_i and of its conormal derivative as [92]

$$\gamma_{0i}^{\pm} g = g_{|\Gamma_i^{\pm}} \tag{2.1a}$$

$$\gamma_{1_i}^{\pm} g = \vec{n} \cdot \bar{\bar{\sigma}} \pm \nabla g_{|\Gamma_i^{\pm}}, \tag{2.1b}$$

where $\bar{\bar{\sigma}}$ is the conductivity tensor Moreover $[\cdot]_{ij}$ will denote the jump of a function across the surface Γ_{ij}: $[g]_{ij} = \gamma_{0i}^{-} g_{ij} - \gamma_{0i}^{+} g_{ij}$ and $[\vec{n} \cdot \bar{\bar{\sigma}} \nabla g]_{ij} = \gamma_{1i}^{-} g_{ij} - \gamma_{1i}^{+} g_{ij}$.

The EEG forward problem amounts at computing the electric potential V knowing the brain electric sources $f = \nabla \cdot j$ when the current j propagates in a medium of conductivity $\bar{\bar{\sigma}}$ which is a real symmetric and positive definite matrix. Under standard quasi-static assumptions, this calls for the solution of the Poisson's equation [91]

$$\nabla \cdot \bar{\bar{\sigma}} \nabla V = f \tag{2.2}$$

with boundary conditions at each interface Γ_{ij}

$$[V]_{ij} = 0 \ \forall i, \forall j \in \omega_i \setminus \{N+1\} \tag{2.3a}$$

$$[\vec{n} \cdot \bar{\bar{\sigma}} \nabla V]_{ij} = 0 \ \forall i, \forall j \in \omega_i. \tag{2.3b}$$

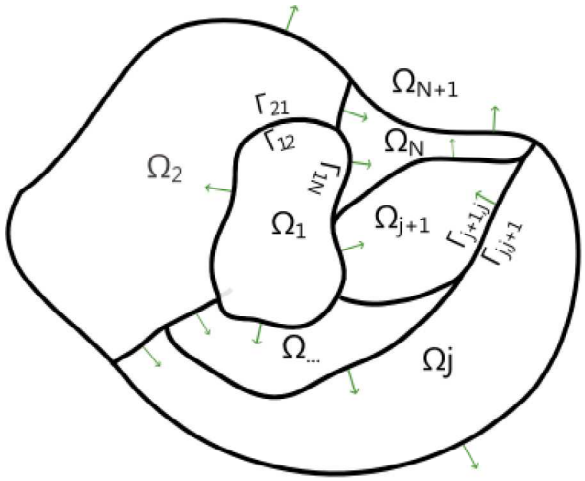

Figure 2.1: Decomposition of the domain Ω into subdomains Ω_i with boundary Γ_{ij} and normal $\vec{n}$.

The conditions above enforce the continuity of the potential and of its derivative between different compartments of the head. The conductivity $\bar{\bar{\sigma}}$ is assumed to be piecewise homogeneous and potentially anisotropic, $\bar{\bar{\sigma}}_i$ will denote the conductivity of the domain Ω_i. The source term $f = \nabla \cdot j$ is usually a linear combination of dipole sources f_j such that $f_j = q_j \cdot \nabla \delta_{r_{0j}}$ with q_j the dipole moment and r_{0j} the dipole position [27], [72].

2.3 A Surface Integral Formulation for Anisotropic Conductivity Profiles

The fundamental solution (Green's function) of (2.2) in an unbounded medium reads [19]

$$G_j(r, r') = \frac{1}{4\pi} \frac{1}{\sqrt{det(\bar{\bar{\sigma}}_j)} \sqrt{\bar{\bar{\sigma}}_j^{-1}(r - r') \cdot (r - r')}} \tag{2.4}$$

where $\bar{\bar{\sigma}}_j$ denotes the homogeneous conductivity tensor of the domain Ω_i. Define the following integral operators

$$S_i \nu(r) = \int_{\Gamma_i} G_i(r, r') \nu(r') dr' \quad S_i : H^{-1/2}(\Gamma_i) \to H^{1/2}(\Gamma_i) \tag{2.5}$$

and

$$D_i \mu(r) = \int_{\Gamma_i} \mu(r') \vec{n'} . (\bar{\bar{\sigma}}_i \nabla G_i(r, r')) dr' \quad D_i : H^{1/2}(\Gamma_i) \to H^{1/2}(\Gamma_i). \tag{2.6}$$

Here and in the following H^s will denote the Sobolev space of order s. It can be shown that for the elliptic differential operator $\Delta_{\bar{\bar{\sigma}}}$ defined as $\Delta_{\bar{\bar{\sigma}}} g = \nabla \cdot \bar{\bar{\sigma}} \nabla g$, we have $(\Delta_{\bar{\bar{\sigma}}} S\nu)(x) = (\Delta_{\bar{\bar{\sigma}}} D\mu)(x) = 0, \forall \nu \in H^{-1/2}, \forall \mu \in H^{1/2}, \forall x \in \Omega$ [92]. It should be noted that

$$\gamma_1^{\pm} S_i = \mp \frac{1}{2} I + D_i^* \tag{2.7}$$

with

$$D_i^* \nu(r) = \int_{\partial\Omega_i} \nu(r) \vec{n} \cdot (\bar{\bar{\sigma}}_i \nabla G_i(r, r')) dr' \quad D_i^* : H^{-1/2}(\Gamma_i) \to H^{-1/2}(\Gamma_i). \tag{2.8}$$

and where I is the identity operator.

2.3.1 A New Anisotropic Integral Formulation for Nested and Non-Nested Compartments

If an integral equation formulation should be able to handle anisotropic conductivity profiles, the integral form of the EEG forward problem cannot be obtained by following the standard procedure. Indeed, the common way to solve the isotropic EEG forward problem (which reads $\Delta V = f/\sigma$ with $\bar{\bar{\sigma}} = \sigma \bar{\bar{\mathbf{I}}}$) is to divide the solution V into two contributions: $V = u + v$. One term, v, accounts for the source term in an unbounded medium. This part of the solution is easily obtained using the Green's function. The second contribution u is a harmonic solution, $\Delta u(r) = 0 \ \forall r \in \Omega$, that enforces the boundary conditions [54]. This harmonic function is an homogeneous solution in each of the sub-domains Ω_i, i.e. whatever the conductivity is, we have $\nabla \cdot \sigma \nabla u = \sigma \Delta u = 0$. However, in the case of the anisotropic EEG forward problem, if u is a homogeneous solution for $\Delta_{\bar{\bar{\sigma}}_1} = \nabla \cdot \bar{\bar{\sigma}}_1 \nabla \cdot$, i.e. $\nabla \cdot \bar{\bar{\sigma}}_1 \nabla u = 0$, we have in the general case $\nabla \cdot \bar{\bar{\sigma}}_2 \nabla u \neq 0$. This means that $\Delta_{\bar{\bar{\sigma}}}$-harmonicity is not maintained between the compartments when the conductivity changes and, as a consequence, u cannot be defined globally harmonic on Ω. A solution is to consider the problem in each compartment separately by leveraging on an indirect approach. We will hence tackle the anisotropic EEG forward problem (2.2) with boundary conditions (2.3a) and

(2.3b) still by considering, $V = u + v$, with v accounting for the source contribution in an unbounded medium but where u is piecewise $\Delta_{\bar{\bar{\sigma}}}$-harmonic i.e. $\Delta_{\bar{\bar{\sigma}}} u = \nabla \cdot \bar{\bar{\sigma}} \nabla u = 0$, and $u = \sum_i u_i$ with $\nabla \cdot \bar{\bar{\sigma}}_i \nabla u_i(r) = 0$ if $r \in \Omega_i$ and $u_i = 0$ elsewhere. The unknown potential V will then be $V = \sum_i V_i$ with $V_i = u_i + v_i$, where v_i is the contribution in an infinite medium of a source placed in Ω_i. In a nutshell, we let

$$V = \sum_i^N V_i \text{ ,with } V_i = u_i + v_i \text{ where } \begin{cases} \bar{\bar{\sigma}}_i \nabla u_i(r) = 0 & \text{if } r \in \Omega_i \\ v_i(r) = \sum_j q_j \cdot \nabla G_i(r, r_{0j}) & \text{if } r \in \Omega_i \\ u_i = v_i = 0 & \text{elsewhere} \end{cases} .$$

The next step is to find a procedure to build the unknown $\Delta_{\bar{\bar{\sigma}}_i}$-harmonic function u_i. As said before, the strategy here is to resort to an indirect approach. Indeed, as shown before, the ansatz $S_i\nu$ satisfies the homogeneous equation $\bar{\bar{\sigma}}_i \nabla S_i \nu = 0$. In other words, for any boundary density ν it is possible to build a $\Delta_{\bar{\bar{\sigma}}_i}$-harmonic function using the single layer potential operator S_i (or the double layer operator D_i, mutatis mutandis). Then the problem amounts at finding the boundary density ν that abides by the boundary conditions (2.3a) and (2.3b). In the following, this particular boundary density will be denoted ϕ_i and then u_i reads

$$u_i = S_i \phi_i \tag{2.9}$$

where $\phi_i \in H^{-1/2}(\Gamma_i)$. Then, the boundaries conditions (2.3a) and (2.3b) allows to write two equations for the unknown ϕ_i such that

$$\begin{cases} \text{(2.3a)} \Leftrightarrow [u + v]_{ij} = 0 \; \forall i, \forall j \in \omega_i \setminus N + 1 \\ \text{(2.3b)} \Leftrightarrow [\vec{n} \cdot \bar{\bar{\sigma}} \nabla (u + v)]_{ij} = 0 \; \forall i, \forall j \in \omega_i \end{cases} \tag{2.10}$$

$$\Leftrightarrow \begin{cases} \gamma^-_{0ij} (S_i \phi_i + v_i) = \gamma^+_{0ij} (S_j \phi_j + v_j) \;\; \forall i, \forall j \in \omega_i \setminus N + 1 \\ \gamma^-_{1_{ij}} (S_i \phi_i + v_i) = \gamma^+_{1_{ij}} (S_j \phi_j + v_j) \;\; \forall i, \forall j \in \omega_i \end{cases} \tag{2.11}$$

The above equations highlight the fact that we can treat each domain separately: in each domain we can express the unknown potential using the unknown boundary density ϕ_i, then the obtained interior problems are linked using (2.11) in order to find the unknown

ϕ_i. As the boundaries of the subdomains are also subdivided, $\Gamma_i = \cup_{i\in\omega_i}\Gamma_{ik}$, we let $\phi_i = \sum_{j\in\omega_i}\phi_{ij}$, with $\phi_{ij} = 0$ in $\Gamma_{ik}, k \neq j$.

Let us consider $\Gamma_{ij} = \Gamma_i \cap \Gamma_j \neq \emptyset$ with $i < j$ to express the interior problems and combine the obtained equations to enforce the boundary conditions at the interface Γ_{ij} (see Figures 2.2a, 2.2b, and 2.2c, where we describe the geometry when dealing with the interface Γ_{12} : we first express the potential in Ω_1 then in Ω_2 and finally find the equations on the interface Γ_{12} between Ω_1 and Ω_2). In Ω_i we have, for $r \in \Gamma_i = \bigcup_{k\in\omega_i}\Gamma_{ik}$, writing $\phi_i = \sum_{k\in\omega_i}\phi_{ik}$ with $\phi_{ik}(r) = 0$ if $r \notin \Gamma_{ik}$, we can derive

$$\gamma_{0,i}^{-}V_i = \gamma_{0,i}^{-}v_i + S_i\phi_i \quad \Leftrightarrow \quad \gamma_{0,ij}^{-}V_i = \gamma_{0,ij}^{-}v_i + \sum_{k\in\omega_i} S_i\phi_{ik} \tag{2.12}$$

$$\gamma_{1,i}^{-}V_i = \gamma_{1,i}^{-}v_i + \frac{1}{2}\phi_i + D_i^*\phi_i \quad \Leftrightarrow \quad \gamma_{1,ij}^{-}V_i = \gamma_{1,ij}^{-}v_i + \frac{1}{2}\phi_{ij} + \sum_{k\in\omega_i} D_i^*\phi_{ik} \tag{2.13}$$

and, in Ω_j, for $r \in \Gamma_j = \bigcup_{l\in\omega_j}\Gamma_{jl}$ with $\phi_j = \sum_{l\in\omega_j}\phi_{jl}$ with $\phi_{jl}(r) = 0$ if $r \notin \Gamma_{jl}$:

$$\gamma_{0,j}^{-}V_j = \gamma_{0,j}^{-}v_j + S_j\phi_j \quad \Leftrightarrow \quad \gamma_{0,ij}^{+}V_j = \gamma_{0,ji}^{-}v_j + \sum_{l\in\omega_j} S_j\phi_{jl} \tag{2.14}$$

$$\gamma_{1,j}^{-}V_j = \gamma_{1,j}^{-}v_j - \frac{1}{2}\phi_j + D_j^*\phi_j \quad \Leftrightarrow \quad \gamma_{1,ij}^{+}V_j = \gamma_{1,ij}^{-}v_j - \frac{1}{2}\phi_{ji} + \sum_{l\in\omega_j} D_j^*\phi_{jl} \tag{2.15}$$

then from (2.3a), (2.12) and (2.14) we obtain

$$\sum_{k\in\omega_i} S_i\phi_{ik} - \sum_{l\in\omega_j} S_j\phi_{jl} = -(\gamma_{0,ij}^{-}v_i - \gamma_{0,ji}^{-}v_j) \tag{2.16}$$

and from (2.3b), (2.13) and (2.15) we get

$$\frac{1}{2}\phi_{ij} + \sum_{k\in\omega_i} D_i^*\phi_{ik} + \frac{1}{2}\phi_{ji} - \sum_{l\in\omega_j} D_j^*\phi_{jl} = -(\gamma_{1,ij}^{-}v_i - \gamma_{1,ij}^{-}v_j). \tag{2.17}$$

After solving (2.16) and (2.17), a solution for the entire EEG forward problem is obtained. In fact, once ϕ_i is known for all i, V can be easily derived using $V_i = v_i + S_i\phi_i = v_i + \sum_k S_i\phi_{ik}$, $k \in \omega_i$. The proposed formulation can be easily be applied, as a special case, to layered domains for which standard formulations are very popular [54].

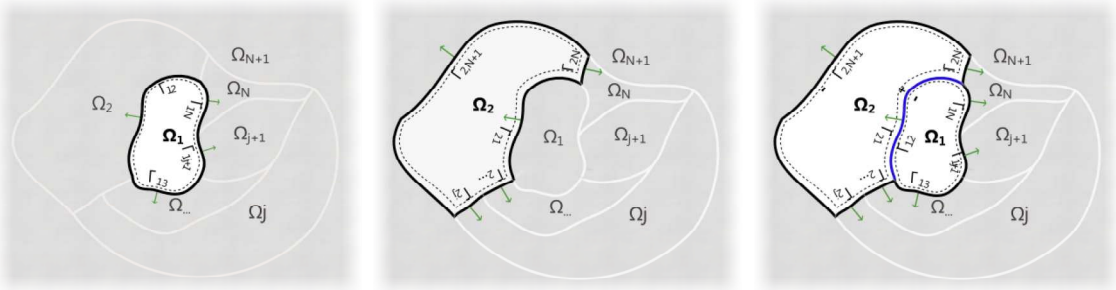

(a) Internal problem in Ω_1.

(b) Internal problem in Ω_2.

(c) Interface problem between Ω_1 and Ω_2.

Figure 2.2: Conventions used in setting up the integral equations.

2.4 Discretization of the New Equation

Following a BEM strategy, to numerically solve the obtained integral equations, the geometry, the unknown and the equations have to be discretized. The geometry is tessellated into N_t triangular cells t_i and N_v vertices ν_i. With $\mathcal{M}_\Omega$ we denote the mesh representing the discretized domain. To obtain a linear system to be solved, following the usual BEM strategy [94], the integral equations must be tested with a suitably chosen set of basis functions. This will give rise to the following linear system

$$\mathbf{Za} = \mathbf{b} \tag{2.18}$$

where $\mathbf{Z}$ is the system matrix that contains the discrete version of the integral equation, i.e. each entry of $\mathbf{Z}$ is given by

$$[\mathbf{Z}]_{kl} = \int_{\mu_{f_{tk}}} f_{tk}(r') Z\left(f_{el}\right)(r') dr' \tag{2.19}$$

where Z is the operator of the integral equation under consideration, $\{f_t\}$ is the set of testing functions, and $\{f_e\}$ is the set of expansion functions. The right hand side $\mathbf{b}$ is defined as

$$[\mathbf{b}]_k = \int_{\mu_{f_{tk}}} f_{tk}(r') b dr', \tag{2.20}$$

with b the known data and $\mu_{f_{tk}}$ the support of the function f_{tk}. The vector $\mathbf{a}$ contains the coefficients in the unknown expansion.

In our case, the unknown ϕ_{ij} can be discretized using as expansion functions, f_{ek} in (2.19), piecewise constant functions P_{0k} such that

$$\phi_{ij} \approx \sum_k a_{ij,k} P_{0k} \tag{2.21}$$

where $P_{0i}(r) = 1$ if $r \in t_i$ and 0 elsewhere. The support of P_{0i} is given by $\mu_{P_{0i}} = t_i$. Piecewise linear elements, P_1, can also be used albeit a higher computational cost. They are defined such that $P_{1i}(r) = 1$ if $r = \nu_i$ and linearly decreases to 0 on their support $\mu_{P_{1i}} = \{t_k | v_i \text{ is a vertex of } t_k\}$. In this case, the discretized unknown would read $\phi_{ij} = \sum_k a_{ij,k} P_{1k}$.

In the context of BEM solutions, Galerkin's strategy to discretize the equations consists in using the same testing function as the expansion functions. This method has been widely used in solving the EEG forward problem with BEM [54]. As [88] has stressed, however, the choice of expansion and testing functions should be carried out with care. In fact, expansion and testing functions should comply, in our case, with the operatorial mappings of the involved integral operators S_i and D_i^*. Standard source and testing boundary elements are chosen to be the piecewise constant ones, i.e. $P_0 \in H^{-1/2}$ would play the role of both expansion and testing functions, f_{ek} and f_{tk}, in (2.19). Regrettably, this is compatible only with a L_2 discretization of D^* while a more consistent formulation would dictate a testing in the dual space of the range of D_i^*, i.e. $H^{1/2}$. This choice is expected to be more performing in particular when the source location is in the proximity of a boundary layer given that a testing with $H^{1/2}$ elements would allow the right hand side to live in $H^{-1/2}$ which is a larger space than L^2. For this reason we also propose a conforming discretization that abides by the mapping properties of the operators, as described in the following paragraph.

2.4.1 Mixed Discretizations and Implementation Related Details

As stated before, the range of S_i is $H^{1/2}$ for which the dual space is $H^{-1/2}$. As $P_0 \in H^{-1/2}$ these functions can indeed be used for testing equation (2.16). However, the operator of

(2.17) is D_i^* whose range is $H^{-1/2}$. This means that P_0 functions suitable to test S_i should not be used. To test in $H^{1/2}$, pyramidal functions $P_1 \in H^{1/2}$ are suitable, but $N_t \neq N_v$, as a consequence, P_1 functions cannot be used directly given that otherwise the system matrix would result being rectangular. A solution is to resort to the so called mixed discretizations. For the sake of completeness and readibility, we recall the main technical points about these techniques. However, for a more detailed treatment of the matter, the reader should refer to [88].

Start by considering the dual mesh $\mathcal{M}_\Omega^*$ of $\mathcal{M}_\Omega$. In this mesh each cell corresponds to a vertex in $\mathcal{M}_\Omega$ and vice versa. The dual mesh is obtained using a barycentric refinement of $\mathcal{M}_\Omega$ by joining each vertex v_i to the mid-point of the opposite edge. Figure 2.3 shows the standard mesh, its barycentric refinement and the dual mesh. We denote with c_i the cells of $\mathcal{M}_\Omega^*$ and with b_i the barycenter of t_i. In $\mathcal{M}_\Omega^*$ we can build the dual pyramidal functions $\tilde{P}_1$ [18], (shown in Figure 2.4c), such that their support $\mu^*_{\tilde{P}_{1i}}$ is the set of cells c_k around the considered barycenter: $\mu^*_{\tilde{P}_{1i}} = \{c_k^* | b_i \text{ is a vertex of } c_k^*\}$. The coefficients to obtain these functions are provided in the caption of Figure 2.4. Hence, using $\tilde{P}_1$ centered on the barycenters of $\mathcal{M}_\Omega$ to test D_i^*, we can correctly discretize (2.17) and obtain a square invertible system matrix.

To fix the ideas and to simplify the implementation of the scheme, we provide below the explicit form of the matrices in the case of the geometry depicted Figure 2.5, were the skull layer is subdivided into four subdomains. The system matrix reads

$$\mathbf{Z} = \begin{pmatrix} \boldsymbol{\Sigma_{11}} & \boldsymbol{\Sigma_{12}} & \dots & 0 \\ \boldsymbol{\Sigma_{21}} & \boldsymbol{\Sigma_{22}} & \dots & 0 \\ \dots & \dots & \ddots & 0 \\ 0 & \boldsymbol{\Sigma_{62}} & \dots & \boldsymbol{\Sigma_{66}} \end{pmatrix},$$

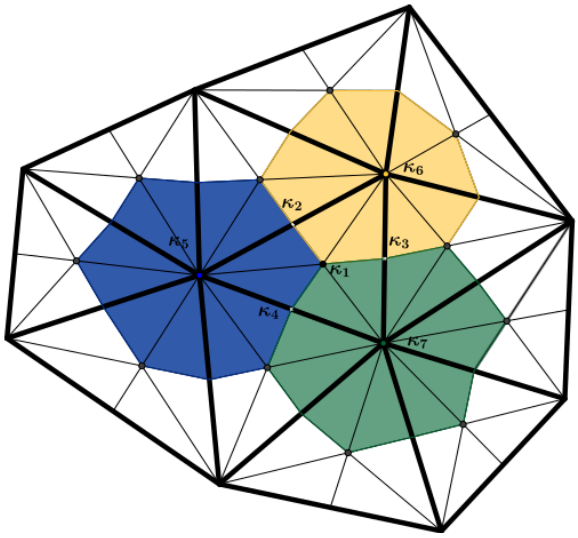

Figure 2.3: Standard mesh (in bold) and associated barycentric refinement. Three cells of the dual mesh are shown in different colors.

with

$$\boldsymbol{\Sigma_{11}} = \begin{pmatrix} \mathbf{S_1} & -\mathbf{S_2} & \mathbf{S_1} & 0 & \mathbf{S_1} & 0 & \mathbf{S_1} & 0 \\ \frac{1}{2}\mathbf{I} + \mathbf{D_1^*} & \frac{1}{2}\mathbf{I} - \mathbf{D_2^*} & \mathbf{D_1^*} & 0 & \mathbf{D_1^*} & 0 & \mathbf{D_1^*} & 0 \\ \mathbf{S_1} & 0 & \mathbf{S_1} & -\mathbf{S_3} & \mathbf{S_1} & 0 & \mathbf{S_1} & 0 \\ \mathbf{D_1^*} & 0 & \frac{1}{2}\mathbf{I} + \mathbf{D_1^*} & \frac{1}{2}\mathbf{I} - \mathbf{D_3^*} & \mathbf{D_1^*} & 0 & \mathbf{D_1^*} & 0 \\ \mathbf{S_1} & 0 & \mathbf{S_1} & 0 & \mathbf{S_1} & -\mathbf{S_4} & \mathbf{S_1} & 0 \\ \mathbf{D_1^*} & 0 & \mathbf{D_1^*} & 0 & \frac{1}{2}\mathbf{I} + \mathbf{D_1^*} & \frac{1}{2}\mathbf{I} - \mathbf{D_4^*} & \mathbf{D_1^*} & 0 \\ \mathbf{S_1} & 0 & \mathbf{S_1} & 0 & \mathbf{S_1} & 0 & \mathbf{S_1} & -\mathbf{S_5} \\ \mathbf{D_1^*} & 0 & \mathbf{D_1^*} & 0 & \mathbf{D_1^*} & 0 & \frac{1}{2}\mathbf{I} + \mathbf{D_1^*} & \frac{1}{2}\mathbf{I} - \mathbf{D_5^*} \end{pmatrix},$$

an $2N_{t_1} \times 2N_{t_1}$ matrix (with N_{t_1} the number of triangles of Γ_1),

$$\boldsymbol{\Sigma_{22}} = \begin{pmatrix} \mathbf{S_2} & -\mathbf{S_3} & \mathbf{S_2} & 0 & \mathbf{S_2} & 0 \\ \frac{1}{2}\mathbf{I} + \mathbf{D_2^*} & \frac{1}{2}\mathbf{I} - \mathbf{D_3^*} & \mathbf{D_2^*} & 0 & \mathbf{D_2^*} & 0 \\ \mathbf{S_2} & 0 & \mathbf{S_2} & -\mathbf{S_5} & \mathbf{S_2} & 0 \\ \mathbf{D_2^*} & 0 & \frac{1}{2}\mathbf{I} + \mathbf{D_2^*} & \frac{1}{2}\mathbf{I} - \mathbf{D_5^*} & \mathbf{D_2^*} & 0 \\ \mathbf{S_2} & 0 & \mathbf{S_2} & 0 & \mathbf{S_2} & -\mathbf{S_6} \\ \mathbf{D_2^*} & 0 & \mathbf{D_2^*} & 0 & \frac{1}{2}\mathbf{I} + \mathbf{D_2^*} & \frac{1}{2}\mathbf{I} - \mathbf{D_6^*} \end{pmatrix},$$

an $2N_{t_2}^* \times 2N_{t_2}^*$ matrix (with N_{t_2} the number of triangles of Γ_2 and $N_{t_{12}}$ the number of

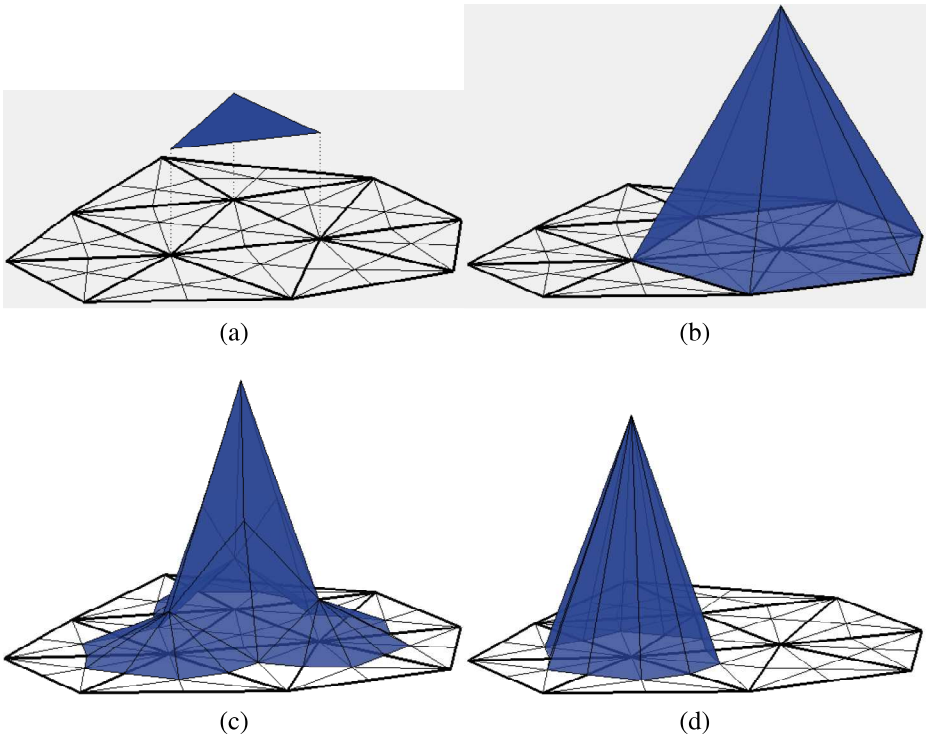

Figure 2.4: Figure (a) shows a constant piecewise function on the standard mesh, Figure (b) a piecewise linear function on the standard mesh, and Figure (c) a dual piecewise linear function. These dual functions are obtained by a linear combination of standard piecewise linear functions $\hat{P}_1$ shown in Figure (d) defined on the barycentrically refined mesh: $\tilde{P}_{1k} = \sum_{l=1}^{7} \kappa_l \hat{P}_{1l}$ with $\kappa_1 = 1$, $\kappa_l = 1/2$ if $l \in \{2,3,4\}$ and $\kappa_l = 1/n$ with n the number of triangles of the standard mesh sharing the considered vertex, if $l \in \{5,6,7\}$. The coefficients κ are shown in Figure 2.3.

triangles in Γ_{12}, $N^*_{t_2} = N_{t_2} - N_{t_{12}}$),

$$\mathbf{\Sigma_{12}} = \begin{pmatrix} -\mathbf{S_2} & 0 & -\mathbf{S_2} & 0 & -\mathbf{S_2} & 0 \\ -\mathbf{D^*_2} & 0 & -\mathbf{D^*_2} & 0 & -\mathbf{D^*_2} & 0 \\ 0 & -\mathbf{S_3} & 0 & 0 & 0 & 0 \\ 0 & -\mathbf{D^*_3} & 0 & 0 & 0 & 0 \\ 0 & 0 & 0 & 0 & 0 & 0 \\ 0 & 0 & 0 & 0 & 0 & 0 \\ 0 & 0 & 0 & -\mathbf{S_5} & 0 & 0 \\ 0 & 0 & 0 & -\mathbf{D^*_5} & 0 & 0 \end{pmatrix}, \mathbf{\Sigma_{21}} = \begin{pmatrix} 0 & \mathbf{S_2} & 0 & -\mathbf{S_3} & 0 & 0 & 0 & 0 \\ 0 & \mathbf{D^*_2} & 0 & -\mathbf{D^*_3} & 0 & 0 & 0 & 0 \\ 0 & \mathbf{S_2} & 0 & 0 & 0 & 0 & 0 & -\mathbf{S_5} \\ 0 & \mathbf{D^*_2} & 0 & 0 & 0 & 0 & 0 & -\mathbf{D^*_5} \\ 0 & 0 & 0 & 0 & 0 & 0 & 0 & 0 \\ 0 & 0 & 0 & 0 & 0 & 0 & 0 & 0 \end{pmatrix},$$

with $\mathbf{\Sigma_{12}}$ a $2N_{t_1} \times 2N^*_{t_2}$ matrix, and $\mathbf{\Sigma_{21}}$ a $2N^*_{t_2} \times 2N_{t_1}$,

$$\mathbf{\Sigma_{62}} = \begin{pmatrix} 0 & 0 & 0 & 0 & 0 & \mathbf{D^*_6} \end{pmatrix}, \mathbf{\Sigma_{66}} = \left(\tfrac{1}{2}\mathbf{I} + \mathbf{D^*_6} \right),$$

with $\mathbf{\Sigma_{62}}$ is a $N_{t_6} \times 2N^*_{t_2}$ matrix (where N_{t_6} is the number of triangles of the outermost

layer, Γ_{67}) and with $\mathbf{\Sigma_{66}}$ a $N_{t_6} \times N_{t_6}$ matrix. and where the matrices $\mathbf{S_i}$ and $\mathbf{D_i^*}$ are given by [7]

$$[\mathbf{S_i}]_{kl} = \int_{t_k} S_i(P_{0l})(r') \; P_{0k}(r') dr' \tag{2.22}$$

$$[\mathbf{D_i^*}]_{kl} = \int_{\mu_k^*} D_i^*(P_{0l})(r') \; \tilde{P}_{1k}(r') dr' \tag{2.23}$$

Each couple of lines of the system matrix $\mathbf{Z}$ is associated with a domain interface and arises from the discretization of the integral equations (2.16) and (2.17). An exception is represented by the last line which corresponds to the outermost surface where we only enforce equation (2.3b). The columns of the matrix also should be considered pairwise: to each pair of column corresponds the inner and outer unknowns defined on the considered interface. Summarizing, the linear system that needs to be solved reads

$$\mathbf{Z} \begin{pmatrix} \mathbf{a_{12}} \\ \mathbf{a_{21}} \\ \mathbf{a_{13}} \\ \vdots \\ \mathbf{a_{65}} \\ \mathbf{a_{67}} \end{pmatrix} = - \begin{pmatrix} \mathbf{b_{12}} \\ \mathbf{d_{12}} \\ \mathbf{b_{13}} \\ \vdots \\ \mathbf{d_{56}} \\ \mathbf{d_{67}} \end{pmatrix} \tag{2.24}$$

where

$$[\mathbf{a_{ij}}]_l = a_{ij,l} \tag{2.25}$$

$$[\mathbf{b_{ij}}]_k = \int_{t_k} (\gamma_{0,ij}^- v_i - \gamma_{0,ji}^- v_j) P_{0k} \tag{2.26}$$

$$[\mathbf{d_{ij}}]_k = \int_{\mu_k^*} (\gamma_{1,ij}^- v_i - \gamma_{1,ji}^- v_j) \tilde{P}_{1k} \tag{2.27}$$

In practice, to compute the elements $[\mathbf{S_i}]_{kl}$ and $[\mathbf{D_i}^*]_{kl}$ two integrations are needed. The inner integral requires to compute either the integral of G_j or of its derivative times

[7] If a standard discretization is to be used (with P_0 used as both expansion and testing functions) then the operators matrices would read: $[\mathbf{S_i}]_{kl} = \int_{t_k} S_i(P_{0l})(r') \; P_{0k}(r') dr'$ (as above) and $[\mathbf{D_i^*}]_{kl} = \int_{t_k} D_i^*(P_{0l})(r') \; P_{0k}(r') dr$.

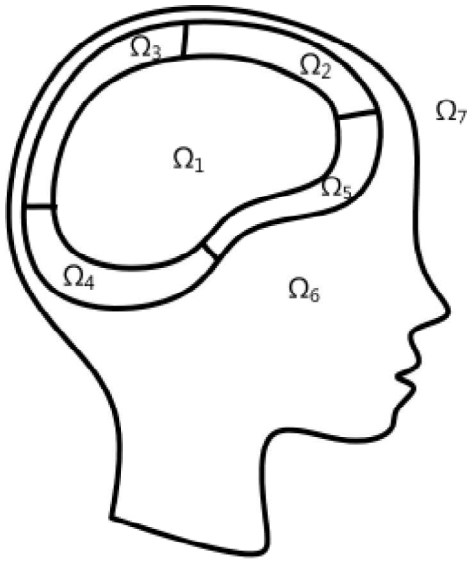

Figure 2.5: Decomposition and notation of the domains used to write the exemplificatory system matrix in Section 2.4.1.

the constant function P_{0i}. An analytical solution to obtain this integration for the usual Green's function $G(r, r') = \frac{1}{4\pi}\frac{1}{||r-r'||}$ has been proposed in [34]. In (2.4), the change of variable $R = \sqrt{\bar{\bar{\sigma}}_i^{-1}}r$ ($\bar{\bar{\sigma}}_i$ is a symmetric positive definite tensor) transforms $G_i(r, r')$ into $G_i(R, R') = \frac{1}{4\pi}\frac{1}{||R-R'||}$ for which we can apply the analytical integration formulas in [34]. The outer integrals (arising from the testing of the operators) are performed numerically using Gaussian integration rules.

Remark 2.1. The formulation can naturally handle volume meshes made of tetrahedra provided that a preprocessing of the volume mesh is done: the neighbouring tetrahedra presenting the same conductivity can be gathered to form one unique domain whose boundary will be defined by the triangular cells of the tetrahedra whose neighbours do not have the same conductivity.

Remark 2.2. As the reader can notice, in the proposed formulation two unknowns per layer are defined except on the outermost layer. Denoting with N_{ext} the number of triangles in the outermost layer, the total number of unknown is given by $2 \times N_t - N_{ext}$.

2.5 Numerical Results

A first set of numerical experiments has been focusing on verifying the convergence of the newly proposed formulation when the number of unknowns is increased. We have firstly considered a spherical geometry with a piecewise homogeneous, nested, and isotropic conductivity profile. The model used consists of three spherical layers of radius 0.87, 0.92 and 1 in normalized units. These layers stand for the brain, skull, and scalp, respectively. A first convergence test was done by using an isotropic conductivity with a ratio between the skull and the brain equal to $\sigma_{skull,iso} = 1/15$, following [76]. It is well known that in this case an analytical solution is available [106]. The accuracy is assessed by calculating $RE = \frac{||V_{BEM} - V_{ref}||}{||V_{ref}||}$, i.e. the relative error V_{BEM} of the proposed integral formulation with respect to the analytic reference solution V_{ref}. The results for this case are shown in Figure 2.6.

In a second test, the validity of the proposed formulation is assessed in the presence of anisotropic conductivity profiles. The same three spherical layer structure of the previous case has been used. In this case, however, it is assumed an homogeneous isotropic conductivity for the brain and the scalp (equal to 1) and a diagonally anisotropic conductivity for the skull such that [104]

$$\frac{4}{3}\pi\sigma_r(\sigma_t)^2 = \frac{4}{3}\pi\sigma_{skull,iso}^3. \tag{2.28}$$

A conductivity ratio of 1/10 has been used between the conductivity along one Cartesian component coordinate (say z) and the other two Cartesian components (x and y). This case, even if not realistic, is chosen only to test the ability to handle anisotropic conductivity profile. In this case, the reference method is a FEM method computed on a very refined mesh.

In both simulations, the number of cells per layer is increased from 320 to 1280. A single dipole source with unitary moment along the z-axis is placed in the center of the

innermost sphere to avoid the dipole position influence on the numerical results (studied in a second scenario). From Figure 2.6 it is clear that the relative error decreases, showing the convergence of the proposed approach.

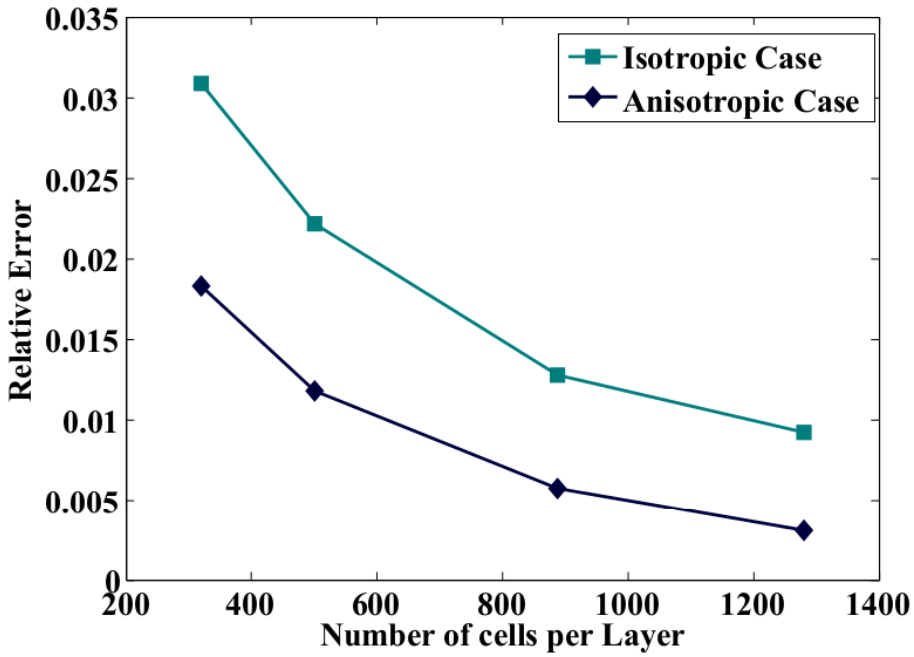

Figure 2.6: Convergence of the solution of the proposed equation when increasing the number of unknowns.

The performances of the proposed formulation has then been evaluated with respect to BEM formulations available in the literature as listed in Table 2.1. As these methods only handle isotropic conductivities, the simulation was performed under this condition. A three layer sphere was employed to model the geometry in order to use the analytical solution as the reference solution for all the methods. In Figure 2.7, the relative error of the formulations with respect to the dipole eccentricity is displayed. It shows that the mixed discretization employed with our formulation enhances greatly the accuracy of the solution of the forward problem with respect to the other methods when the dipole is moved close to the exterior boundary of the brain. It should be noted that the high accuracy of

the adjoint double layer discretized with P1 expansion and testing functions for low dipole eccentricity is obtained at the cost of using linear elements, and as a consequence a higher computational load. The relative error with respect to the conductivity ratio is shown in Figure 2.8. It is evident from the figure that the performance of the proposed approach is very competitive with the existing formulations.

Abbreviation	Name	Discretization	
		testing functions	expansion functions
DLP0	Double Layer	P0	P0
DLP1		P1	P1
SLP0	Adjoint Double Layer	P0	P0
SLP1		P1	P1
SYM	Symmetric formulation [54]	P0 & P1	P0 & P1

Table 2.1: Acronyms used for identifying different BEM formulations in the numerical examples.

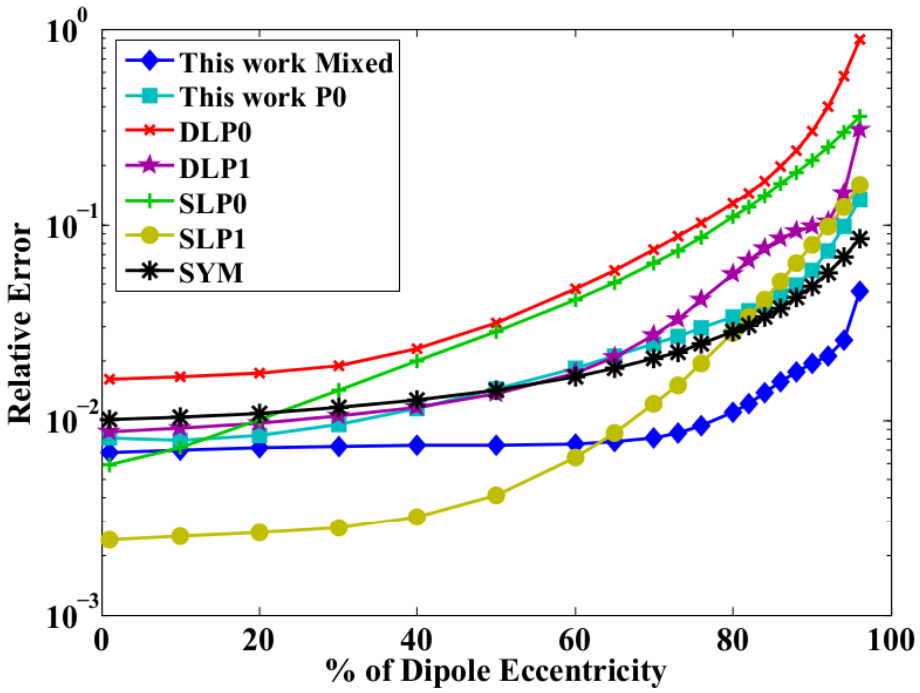

Figure 2.7: Relative error vs dipole eccentricity for the method proposed in this work and for other formulations in literature (see Table 2.1 for interpreting the acronyms).

Since one dipole may not be representative of the complex brain electric sources pattern of activation, we carried out another experiment in which dipole positions are randomly set.

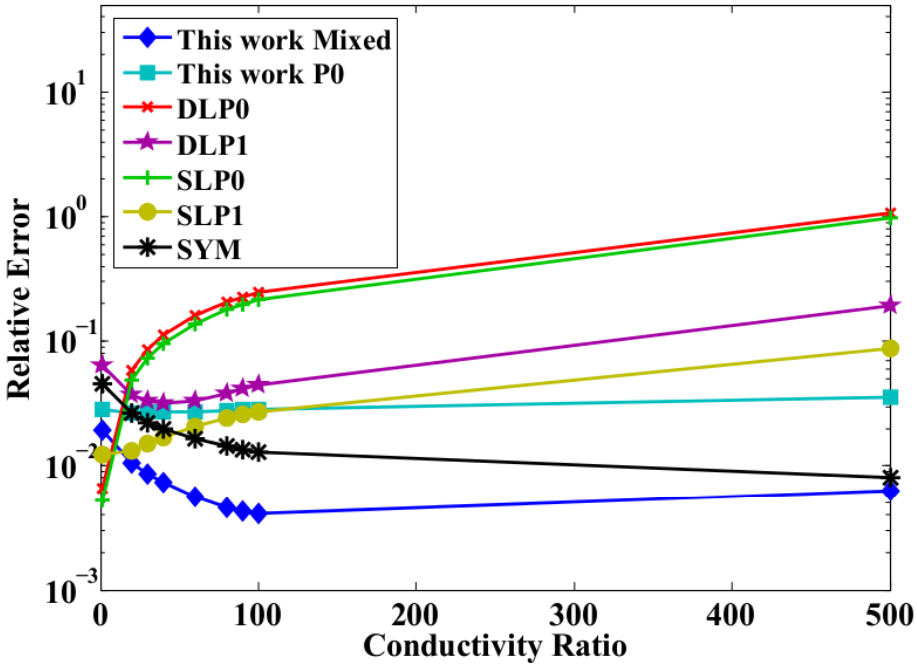

Figure 2.8: Relative error vs conductivity ratio (between the skull and the scalp) for the method proposed in this work and for other formulations in literature (see Table 2.1 for interpreting the acronyms).

For each eccentricity, we computed the relative error in 100 simulations of 1 dipole source, for radial and tangential dipole moment. The resulting Relative Difference Measure (RDM) and Magnification error (MAG) are shown Figure 2.9 and Figure 2.10. These two figures confirms that the proposed approach provides a formulation whose accuracy matches the other existing formulation with the advantage that it can handle anisotropies as will be shown in further numerical experiments.

The axons present in the white matter result in an anisotropic conductivity profile since, along the fiber, the conductivity is ten times higher. This can be modelled by adding, in the brain layer, differently conducting cylinders that would simulate the axons' presence as in the study case proposed by [75]. Following this paper, we considered a cylindrical region of anisotropic conductivity oriented along the z-axis in the innermost sphere of an isotropic three-layers model. The cylindrical region has a radius 0.05, length 1, and it is centered in (0.2, 0, 0). In this simulation, the conductivity ratio between the skull and the scalp is 1/30,

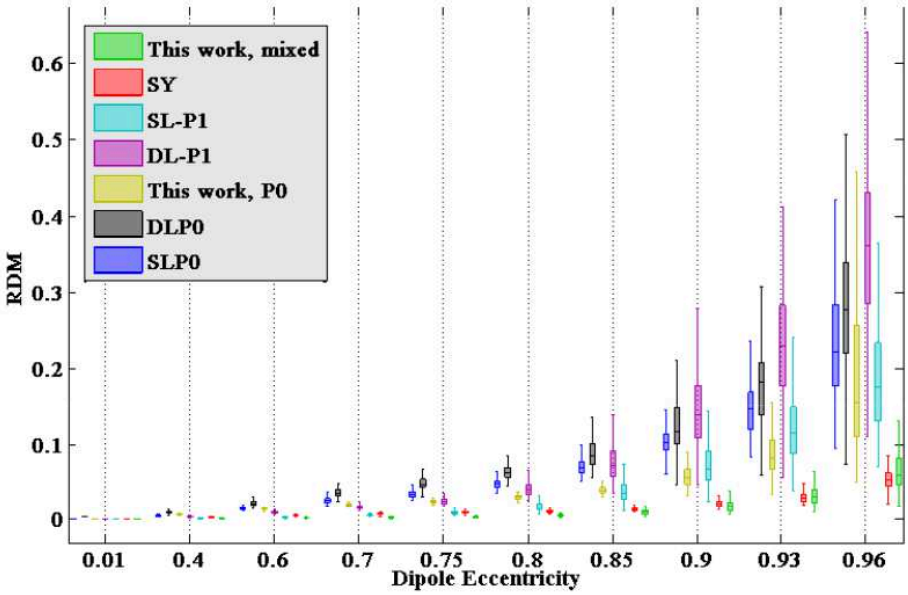

Figure 2.9: Relative Difference Measure versus dipole eccentricity in the computation of 100 dipole source both for radial and tangential dipole orientation for the method proposed in this work and for other formulations in literature (see Table 2.1 for interpreting the acronyms).

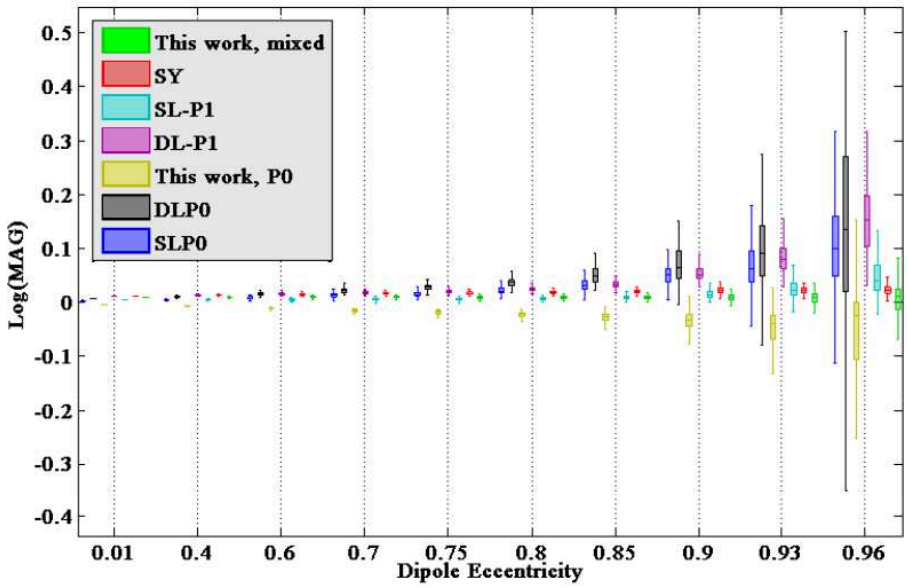

Figure 2.10: Magnitude error versus dipole eccentricity in the computation of 100 dipole source both for radial and tangential dipole orientation for the method proposed in this work and for other formulations in literature (see Table 2.1 for interpreting the acronyms).

following [75]. The results are shown in Figure 2.11. The results of the simulation without anisotropy are presented in Figure 2.11a, in this case, the relative error is computed against

the analytical solution [106]. The relative error with respect to the dipole eccentricity in the presence of the fiber (anisotropic case) is instead displayed in Figure 2.11b. In this case, the reference solution for computing the relative error is a FEM solution. From the figures it is clear that the accuracy of the formulation is not jeopardized by the presence of the anisotropy.

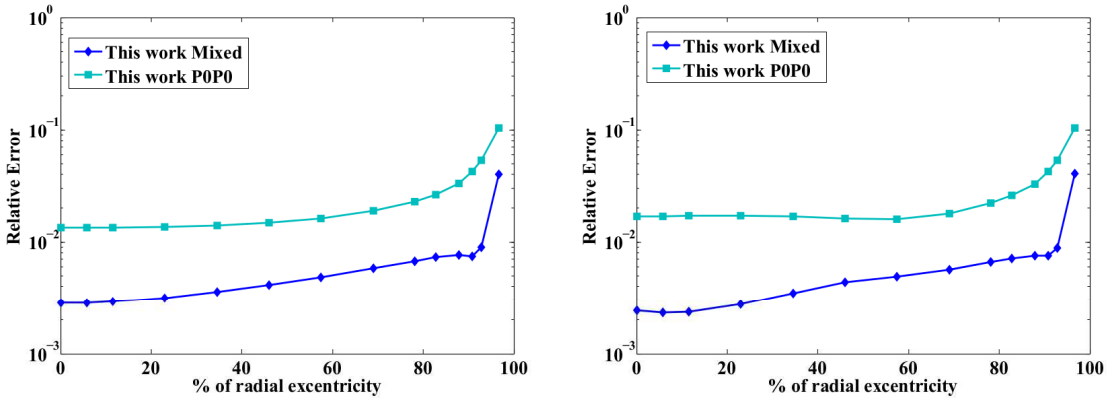

(a) (b)

Figure 2.11: Relative Error with respect to the dipole source excentricity, when no anisotropy is present (Figure (a)) and when an anisotropic fiber is inserted (Figure (b))

A last simulation was performed showing that the proposed formulation can also handle volume mesh. This has the advantage that it could directly be applied to MRI data in which the conductivity is known in each voxel. It consists in a three layer sphere of radii 0.87, 0.92 and 1. The conductivity is assumed isotropic in the innermost layer (representing the brain), radially anisotropic in the layer representing the skull and isotropic in the outermost layer (that represents the scalp). The conductivity ratio between the brain and the scalp is $1/15$ and the ratio between the radial and tangential conductivity in the skull is $1/10$. We start from a volume mesh and extract a surface mesh according to these values of conductivity as explained in the remark 2.1. To achieve a higher accuracy, we selected a very low difference in the conductivity between two adjacent tetrahedra that are to be merged : two tetrahedra with respective index i and j where merged if $||\bar{\bar{sigma}}_i - \bar{\bar{sigma}}_j|| < 10^{-3}$. In this fashion, no tetrahedron of the skull layer will be merged with its neighbour while the tetrahedra in

the brain and scalp layers will be gathered to form only two domains. Figure 2.12 shows the volume mesh and the surface mesh obtained. We show in Figure 2.13 that while refining the mesh, the relative error with the analytical solution described in [107] for radial anisotropy decreases. This shows the correctness of the approach. In this numerical experiment, the skull conductivity was chosen 15 times smaller than the conductivity of the brain and the scalp. The anisotropic conductivity was set in the skull layer by applying equation (2.28) in each tetrahedra, with a ratio of $1/10$ between the radial and tangential conductivity.

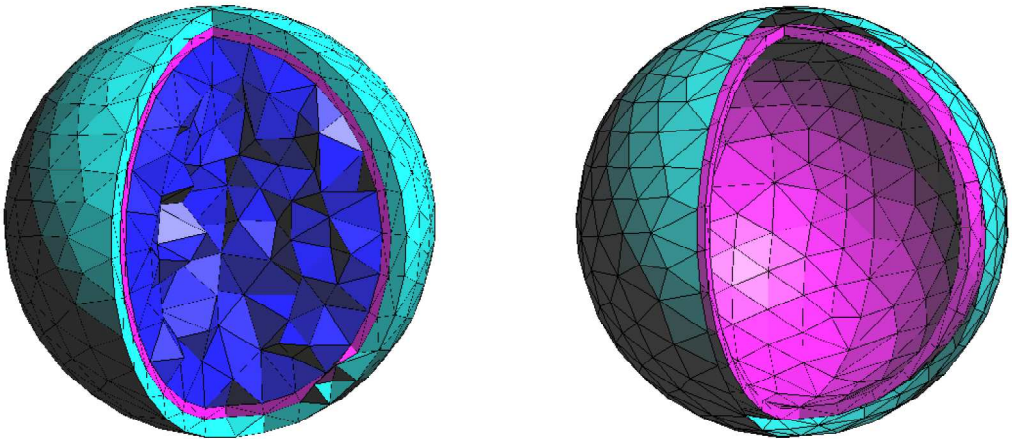

(a) Volume mesh.

(b) Surfacic mesh obtained after preprocessing, according to the conductivity value of the tetrahedra.

Figure 2.12: Volume mesh before (a) and after preprocessing (b)

This method can easily be applied to realistic data. From grey scale data given by MRI, it is possible to extract volume meshes (see for example [29]) that are usually used in FEM simulations. From this volumetric mesh, our method can extract surfaces that delimit domains with the same conductivity (up to a chosen relative error) and run the proposed BEM anisotropic formulation. We applied this to MRI data obtained from the adult brain atlas [20]. The first mesh generation done by [28] results in a tetrahedral mesh. From this volume mesh, shown in Figure 2.14a, the preprocessing subroutine provides a surface mesh presented in Figure 2.14b for which we can directly apply the proposed method. The

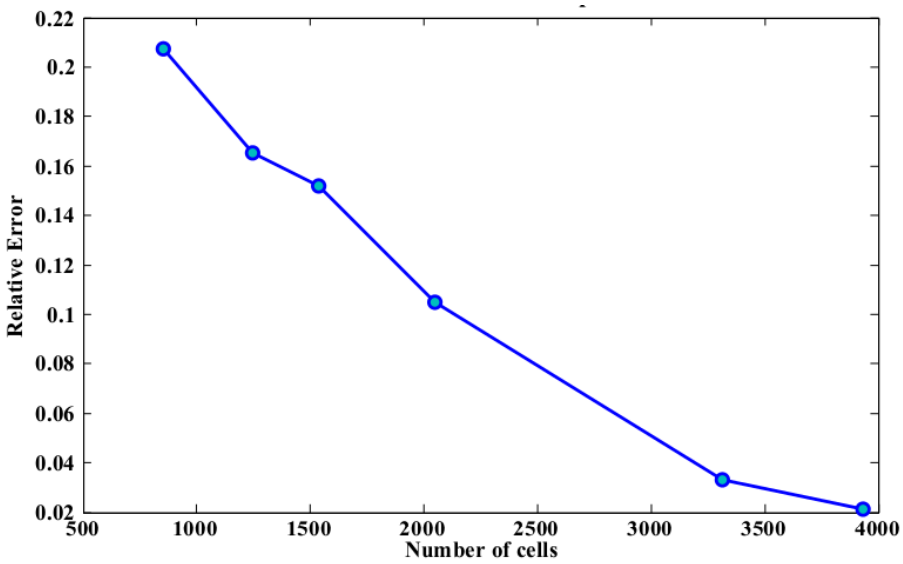

Figure 2.13: Relative error of the new anisotropic solution with respect to the analytical solution

number of tetrahedra was reduced from 423345 to 119554 triangular cells. The potential computed with the proposed method is shown Figure 2.15.

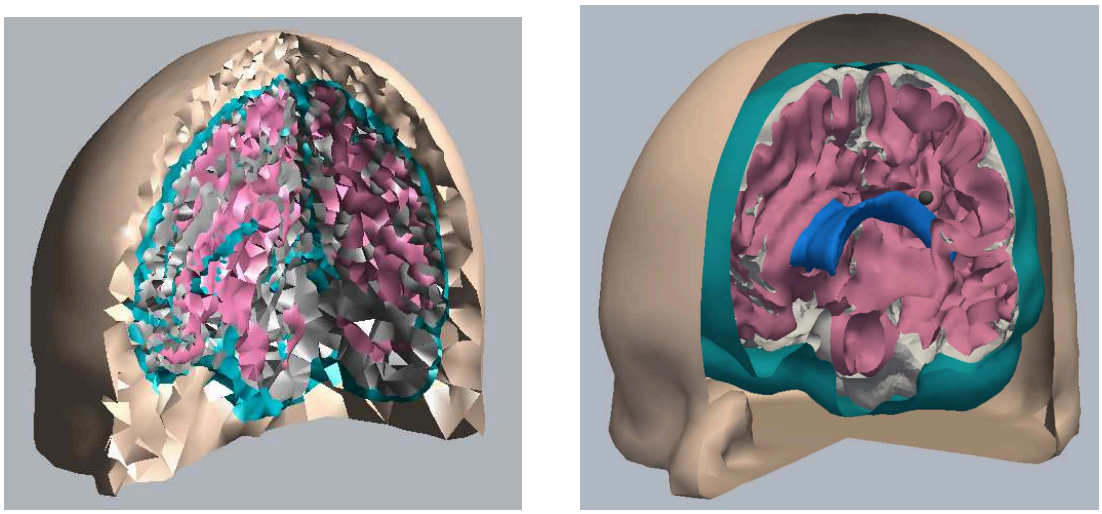

(a) Volume mesh.

(b) Surface mesh obtained after preprocessing, according to the conductivity value of the tetrahedra.

Figure 2.14: Realistic Volume mesh before (a) and after preprocessing (b).

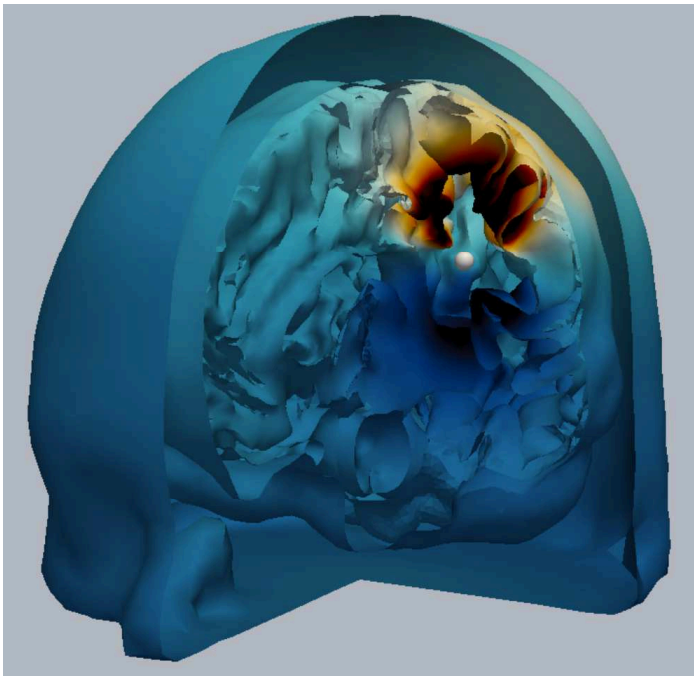

Figure 2.15: Simulation of the potential generated by a dipole in the realistic head mesh using the proposed formulation. The dipole source is represented by a white sphere.

2.6 Discussion and Conclusion

In this chapter, a new integral formulation for the EEG forward problem that takes into account anisotropic conductivity profiles was presented. The integral formulation is obtained by leveraging on an indirect approach and can naturally take into account non-nested domains. Implementations details are provided and explain in particular the mixed discretization strategy.

The numerical results show the correctness of the formulation. The parameter used to assess the accuracy of the new integral formulation is the relative error with respect to a reference solution. When the geometry is a layered isotropic sphere, the reference solution is an analytical solution. For all the other cases, the reference solution is a FEM solution computed on a very refined mesh. The first numerical test studies the convergence of the proposed formulation with respect to the mesh refinement both with isotropic and anisotropic conductivity profiles (Figure 2.6). It clearly shows that the relative errors of the

proposed formulation decreases with the increase of the number of unknowns. The second test compares the new formulation with existing integral equations for solving the EEG forward problems. It shows that the accuracy of the proposed approach is comparable to the accuracy of the existing formulations both when the dipole is moved towards a boundary (Figure 2.7) and for different values of conductivity ratio between the brain and the skull (Figure 2.8). The third test reproduced a study case proposed by [75] in which a cylindrical anisotropic conductive volume is introduced in the innermost medium of a nested three layers geometry. The results of these simulations (Figure 2.11a and Figure 2.11b) show that the accuracy of the approach is preserved in the presence of anisotropic conductivity and confirms the ability of the proposed formulation to handle anisotropic conductivity profile. The last test case scenario shows the ability of the proposed method to handle realistic MRI obtained head models.

Summarising, the new integral equation is able to handle anisotropic conductivity profiles using only surface elements. The proposed formulation is at least as accurate as the existing BEM formulation for the EEG forward problem. A limitation of the proposed formulation, reminiscent of similar limitations of other surface schemes for isotropic profiles, is that it can handle only piecewise constant anisotropic conductivity profiles. As shown in our results however, this drawback can be effectively mitigated by the capability of our scheme of easily handling non nested domains and tetrahedral meshes with inhomogeneous conductivity.

Chapter 3

EEG Brain Source Reconstruction Based on Mixed Discretization

This chapter will assess the impact of mixed forward EEG formulations in the EEG inverse problem. Its contribution is twofold : (i) to merge the mixed forward formulation with the inverse algorithm in a stable way, effectively decreasing the error which is traditionally observed when the source approaches the boundary; (ii) we will show by means of extensive numerical assessments that mixed discretization BEM formulation compares favorably with previously existing techniques and that this technique can be easily adapted to real case scenarios.

3.1 Background and Notations

3.1.1 The EEG Forward Problem

The EEG forward problem is based on the solution of the Poisson equation [85] that reads

$$\nabla \cdot \sigma \nabla \Phi = f \text{ in } \mathbb{R}^3 \tag{3.1}$$

where Φ stands for the electrical potential generated in the medium, σ for the medium conductivity and f represents the electrical sources. It is generally accepted that these sources can be represented by dipoles [27] [72].

The head is modelled by N nested compartments Ω_i, where i denotes the domain index, $i \in \{1, 2, ..N+1\}$. Ω_{N+1} is the external unbounded domain. We denote Γ_i the boundary

of Ω_i : $\Gamma_i = \partial_{\Omega_i}$. These domains usually stand for the brain, the skull and the scalp. Furthermore, the conductivity is considered homogeneous and isotropic in each region. It can then be represented with a piecewise constant function σ_i in each Ω_i with $\sigma_{N+1} = 0$. Setting f_i as the source in Ω_i with $f_{N+1} = 0$, ((3.1)) becomes, in each domain

$$\sigma_i \Delta \Phi = f_i \tag{3.2}$$

where we have : $\sum_i f_i = f$. Associating to ((3.2)) the boundary conditions on ∂_{Ω_i} that stand for the continuity requirement of the potential and its conormal derivative, we obtain the so-called EEG forward problem [54] [85] :

$$\sigma_i \Delta \Phi = f_i \ \ \forall i = 1, \ldots, N \tag{3.3}$$

$$[\Phi]_i = 0 \ \ \forall i = 1, \ldots, N-1 \tag{3.4}$$

$$[\sigma \partial_{\hat{\mathbf{n}}} \Phi]_i = 0 \ \ \forall i = 1, \ldots, N \tag{3.5}$$

with $\hat{\mathbf{n}}$ the outward normal to the surface ∂_{Ω_i} and where $[\cdot]_i$ defines the jump of a function g at the surface ∂_{Ω_i} such that $[g]_i = g_i^- - g_i^+$, where g_i^- and g_i^+ are respectively the inner and outer limit of the function g at the boundary Γ_i.

3.1.2 Boundary Integral Formulations

A common way to solve ((3.1)) is to divide the solution Φ into two parts [54]: a harmonic part ϕ_h which gives the solution of ((3.3)) with a source term equal to zero and which takes into account the boundary conditions ((3.4)) ((3.5)), and a function ϕ_s which will account for the source term f_i in an unbounded medium. Thus we have: $\Phi = \phi_h + \phi_s$. Given that we model the electric sources using dipoles [27] [72], ϕ_s is built using a dipolar potential $v_{dip}(\mathbf{r}) = \frac{\mathbf{q} \cdot (\mathbf{r}_0 - \mathbf{r})}{4\pi ||\mathbf{r} - \mathbf{r}_0||^3 \sigma}$, where $\mathbf{q}$ is the dipole moment and r_0 is the position of the dipole.

By selecting the boundary conditions that are naturally respected by the source term solution ϕ_s, different solutions are obtained [5] [54]: the double layer formulation, the

symmetric formulation and the adjoint double layer formulation. We will define the following operators:

- the double layer operator:

$$D\Psi(\mathbf{r}) = \int_\Gamma \Psi(\mathbf{r}')\partial_{\bar{n}'}G(\mathbf{r}-\mathbf{r}')d\mathbf{r}',\ D : H^{1/2}(\Gamma) \to H^{1/2}(\Gamma), \tag{3.6}$$

- the adjoint double layer operator:

$$D^*\Psi(\mathbf{r}) = \int_\Gamma \Psi(\mathbf{r}')\partial_{\bar{n}}G(\mathbf{r}-\mathbf{r}')d\mathbf{r}',\ D^* : H^{-1/2}(\Gamma) \to H^{-1/2}(\Gamma), \tag{3.7}$$

- the single layer operator:

$$S\Psi(\mathbf{r}) = \int_\Gamma \Psi(\mathbf{r}')G(\mathbf{r}-\mathbf{r}')dr',\ S : H^{-1/2}(\Gamma) \to H^{1/2}(\Gamma) \tag{3.8}$$

where $H^s(\Gamma), s \in \{-1/2, 1/2\}$ denotes the Sobolev space of order s, and where G is the Green's function associated to ((3.2))

$$G(\mathbf{r}-\mathbf{r}') = \frac{1}{4\pi||\mathbf{r}-\mathbf{r}'||}\ . \tag{3.9}$$

The next paragraph of this section will briefly review the adjoint double layer and double layer BEM formulation. For the sake of conciseness, the development will be superficial. For a more elaborate approach, the reader can refer to [54].

The adjoint double layer formulation arises by enforcing the condition of continuity of the derivative ((3.5)) at the boundary. It starts by defining the source contribution as

$$\phi_{s1} = \sum_{i=1}^{N} \frac{v_{dip,\Omega_i}}{\sigma_i}. \tag{3.10}$$

This gives $[\phi_{s1}] = 0$. As $[\Phi] = 0$, we directly have $[\phi_{h1}] = 0$. This means that one of the boundary condition is naturally enforced with the choice of the dipole contribution. It remains to enforce the continuity of the conormal derivative. This is given by ((3.5)), we need $[\sigma\partial_{\bar{n}}\phi]_i = [\sigma\partial_{\bar{n}}\phi_{h1} + \sigma\partial_{\bar{n}}\phi_{s1}]_i = 0$. Solving the following integral equation

$$\partial_{\bar{n}}\phi_{s_1,\Gamma_i} = \frac{\sigma_i + \sigma_{i+1}}{2(\sigma_{i+1} - \sigma_i)}\xi_{\Gamma_i} - \sum_{j=1}^{N} D^*_{ij}\xi_{\Gamma_j} \tag{3.11}$$

where $\xi_{\Gamma_i} = [\partial_{\hat{\mathbf{n}}}\phi_{h1}]_i$ is the unknown permits to find, in a second step, the potential ϕ

$$\phi = \phi_{s1} + \sum_{i=1}^{N} S_i \xi_{\Gamma_i}. \tag{3.12}$$

The double layer is obtained in a similar fashion, setting:

$$\phi_{s_2} = \sum_{i=1}^{N} \phi_{s,\Omega_i} \tag{3.13}$$

where ϕ_{s,Ω_i} is the unknown potential in Ω_i, the condition ((3.4)) is now the condition to be enforced, it eventually gives rise to

$$\phi_{s_2,\Gamma_i} = \frac{\sigma_i + \sigma_{i+1}}{2}\phi_{\Gamma_i} - \sum_{j=1}^{N}(\sigma_{j+1} - \sigma_j) D_{ij} \phi_{\Gamma_j} \tag{3.14}$$

that provides directly ϕ.

3.2 Mixed EEG formulations

In order to obtain a numerical solution to the EEG forward problem, discretization of the geometry and of the solution must be considered. The geometry is discretized through the meshing of the surface $\Gamma = \bigcup_i \Gamma_i$ into N_t triangular cells and N_v vertices. We denote $\mathscr{M}_\Omega$ the mesh defined on Ω such that: $\mathscr{M}_\Omega^2 = \{t_i\}_{i=1}^{N_t}$ is the subset of $\mathscr{M}_\Omega$ of the triangular cells, $\mathscr{M}_\Omega^0 = \{v_i\}_{i=1}^{N_v}$ is the subset of $\mathscr{M}_\Omega$ containing the vertices or nodes. On $\mathscr{M}_\Omega$, basis functions a_i and testing functions b_i are defined.

Integrating the operators against the testing function b_i permits to discretize the equations. We then denote

$$[\mathbf{Z}]_{ij} = \langle b_i, Z a_j \rangle = \int_{\mu_i} b_i(r) Z a_j(r) dr \tag{3.15}$$

the system matrix that derives from the discretization of the operator Z with the basis function a_j and the testing function b_i, where μ_i is the support of b_i.

Patch basis functions or piecewise constant functions $P_0 = span\{P_{0i}\}_{i=1}^{N_t}$ and pyramid functions or piecewise linear functions $P_1 = span\{P_{1i}\}_{i=1}^{N_v}$ are two sets of boundary elements commonly used either for basis or testing functions. In our approach, we

used $P_{0i} = 1$ on t_i and 0 elsewhere. $P_{1i} = 1$ on v_i and linearly decreases to 0 in all other vertices. For P_0 functions, we have $\mu_i = t_i$ and for P_1 functions we have $\mu_i = \{t_j : v_i \text{ is a vertex of } t_j\}$.

The standard formulations [5] [54] are usually discretized using the Galerkin method, this means that testing and basis functions are in the same functional space. When the operator is discretized and tested with P_0 functions, ((3.15)) becomes

$$[Z]_{ij} = \int_{t_i} P_{0i}(r) Z P_{0j}(r) dr \tag{3.16}$$

However, Petrov-Galerkin theory states that the testing should be performed in the dual space of the operator [94]. This means in particular that $D^* : H^{-1/2} \rightarrow H^{-1/2}$ should be tested with functions in $H^{1/2}$. The usual choice of piecewise constant functions $P_0 \subset H^{-1/2-\epsilon}$, $\epsilon > 0$, does not abide by the regularity requirements of $H^{1/2}$. Galerkin discretization using $P1$ basis function could be performed but this requires a higher computational cost.

A solution to discretize and test correctly the previous equations is to resort to the mixed formulations introduced by our team [88] in the context of EEG. These formulations provide a way to merge in the same integral formulation functions in $H^{-1/2}$ or in $H^{1/2}$ either as basis or testing functions. In particular for the adjoint double layer formulation, it proposes to use $P_0 \subset H^{-1/2}$ functions for the discretization of the potential and $\tilde{P}_1 \subset H^{1/2}$ functions as testing functions.

One should note that P_1 functions are defined with respect to vertices, as $N_t \neq N_v$, it is not possible to use directly P_1 functions for the testing : the system matrix would be rectangular. The dual mesh $\mathscr{M}_\Omega^*$ of $\mathscr{M}_\Omega$ must then be used. This mesh has been defined in Chapter 2, section 2.4. We just recall here the definition of the dual functions that are used. We denote $P_1^* = \{P_{1i}^*\}_{i=1}^{N_v*}$ the set of piecewise linear functions defined on the barycentric refined mesh. The dual pyramid functions, also known as the as the Buffa-Christiansen

basis functions [18] , are $\tilde{P}_1 = span\{\tilde{P}_{1i}\}_{i=1}^{N_t}$, obtained by linear combination of seven P_1^* functions : $\tilde{P}_{1i} = \sum_{j=1}^{7} \alpha_j P_{1j}^*$.

We then obtain, for the usual discretizations and testing :

$[D]_{ij} = \langle P_{0_i}, DP_{0_j} \rangle$

$[D^*]_{ij} = \langle P_{0_i}, D^* P_{0_j} \rangle$

and for the mixed adjoint double layer formulation:

$\left[\tilde{D}^*\right]_{ij} = \langle \tilde{P}_{1_i}, D^* P_{0_j} \rangle$.

label	Formulation	basis	testing
D*P0P0	Standard single layer	P_0	P_0
DP0P0	Standard double layer	P_0	P_0
D*P0P1	Mixed single layer	P_0	$\tilde{P}_1$

Table 3.1: labels of testing and basis functions of the EEG Integral formulations studied

3.3 A mixed Discretization Based Inverse Problem

In the integral equations (3.11) and (3.14) the unknowns $\xi_{\partial\Omega_i}$ and $\phi_{\partial\Omega_i}$ respectively, are discretized using P_0 basis functions. Denoting X_i the unknown for both formulation, we obtain:

$$X_i = \sum_{j}^{N_t} x_{i,j} P_{0_i} \tag{3.17}$$

The known source potential ϕ_{s,Γ_i} on Γ_i and its derivative $\partial_{\hat{\mathbf{n}}}\phi_{s,\Gamma_i}$ are used in the double layer and respectively in the adjoint double layer to obtain the solution of the integral equation. We denote this known term Ψ_s in both cases.

Using (3.17) and testing against the chosen testing functions b_i, (P_{0i} in the usual formulations and $\tilde{P}_{1i}$ for the mixed adjoint double layer formulation), the equations (3.11) and (3.14), we obtain the discretized equations that can be written in a matrix form

$$\mathbf{ZX} = \mathbf{\Phi_s} \tag{3.18}$$

with $\mathbf{X}$ the vector containing the unknown coefficients $x_{i,j}$, and $[\mathbf{\Psi_s}]_j = \langle b_j, \Psi_s \rangle$. $\mathbf{Z}$ is the system matrix. It contains the $[Z]_{ij}$ terms plus a term $[I]_{ii}$ on the diagonal. In the adjoint double layer formulations $[I]_{ii} = \frac{\sigma_i + \sigma_{i+1}}{2(\sigma_{i+1} - \sigma_i)} \langle b_i, P_{0_i} \rangle$ and in the double layer formulation $[I]_{ii} = \frac{\sigma_i + \sigma_{i+1}}{2} \langle b_i, P_{0_i} \rangle$.

Solving this system of equations allows to compute the desired potential. In the context of the inverse problem, solving (3.18) enables to compute the potential generated by known brain electric sources at the electrodes location. The inversion permits to find the active source knowing the potential. This problem is ill-posed : there are much more unknown than measurements. That means that the solution is not unique.

The next paragraph ((3.3.1)) will present the merging of the inverse EEG problem and the forward problem.

3.3.1 Solving the Inverse Problem

Given a set of EEG measurments, the solution of the EEG inverse problems is the source configuration that generated the measured potential. Solving this problem can be done in two fashions [37]. Parametric solutions look for the position and the amplitude of the sources while distributed solutions make assumptions on the source positions and seek only their amplitude. In what follows, we tackle the EEG inverse problem from this distributed point of view. In this approach, the solution of the forward problem is computed for each position of grid with unitary dipole moment in the three cartesian directions. Note that the orientation can also be enforced for the sources. We will denote with d the number of orientations for which the forward solution is computed ($d = 3$ or 1). We further assume that the measurements are a linear combination of the sources placed in this grid. Then, from this perspective and denoting with M the number of points in this grid (sources) and with N the number of measurement points (electrodes), solving the EEG inverse problem

amounts to solving the following equation

$$\mathbf{GJ} = \mathbf{\Phi}. \tag{3.19}$$

where $\mathbf{J}$ is a $dM \times 1$ vector that contains the source amplitude for each chosen directions; $\mathbf{\Phi}$ is a $N \times 1$ vector containing the measured potentials; and $\mathbf{G}$ is a $N \times dM$ matrix often called lead-field matrix that contains the solution of the forward problem. Since the number of measurements is small with respect to the number of unknowns ($M \gg N$), the inverse problem is ill-posed. One of the consequence of this ill-poseness is that the solution is not unique. A particular solution is obtained by choosing a cost function. The solution will then be given by computing the minimum of this cost function. Different assumptions on the source model will give rise to different functions (and solutions) [79] [37] [12]. The simplest approach consists in assuming that the solution will be given by the minimum energy solution. This approach is called the minimum norm estimate. By regularizing the solution using its variance reference [80] developed sLORETA. This algorithm is known to provide in a noiseless and single source localization context, an exact solution to the localization problem. Given these properties, it is this algorithm that we chose to assess the effect of mixed discretization on brain source reconstruction.

The solution of (3.19) using sLORETA [80] is obtained in several steps. The first step is to solve the minimum norm problem given by the minimum of the following function:

$$F_\lambda(\mathbf{J}) = \left(||\Phi - \mathbf{GJ}||^2 + \lambda||\mathbf{J}||^2\right) \tag{3.20}$$

where λ is a regularization parameter that controls the trade-off between the fidelity to the measurements and the norm of the solution. Its minimum gives the estimated current distribution $\hat{\mathbf{J}}$ such that

$$\hat{\mathbf{J}} = \mathbf{T\Phi} \tag{3.21}$$

where

$$\mathbf{T} = \mathbf{G}^T[\mathbf{GG}^T + \lambda\mathbf{I}_M]^{-1}. \tag{3.22}$$

This solution actually corresponds to the minimum norm estimate [37]. In sLORETA, a second step is performed that consists in standardizing the computed current distribution $\hat{\mathbf{J}}$ with the estimated variance of the data $S_{\hat{\mathbf{J}}} = \mathbf{G}^T[\mathbf{G}\mathbf{G}^T + \lambda \mathbf{I}_M]^{-1}\mathbf{G}$. Then in the l^{th} point of the grid, the estimated current density is given by

$$\hat{\mathbf{J}}_l^T([S_{\hat{\mathbf{J}}}]_{ll})^{-1}\hat{\mathbf{J}}_l. \tag{3.23}$$

3.4 Numerical Results

This section studies the influence of the choice of the forward formulation in solving the EEG inverse source problem. It presents the impact of the previously presented BEM formulations for localizing a single dipole, in the presence of noise, for different source positions and using a realistic head mesh.

3.4.1 Methodology

We first consider spherical head mesh. Indeed, a layered sphere can provide a simple model of the head anatomy in a first approximation and has the advantage that for such a head model, the analytical solution [40] is available and can be used as benchmark. In this scenario, 256 electrodes were placed on the outermost layer of the head model. The measured potential for each of the electrodes has been computed using the analytical solution. The layered sphere is made of three nested spheres whose respective radius are 0.87, 0.92 and 1 according to Rush's spherical head model [90] and represent respectively the brain, the skull and the scalp. Each sphere is meshed into 500 triangular cells. The reference electrode was arbitrarily chosen to be the average of the measurements since [68] stated that the reference electrode would not influence the spatial distribution of the electrodes potential and thus the source reconstruction.

The last part of this section 3.4.4, presents the results obtained in the case of a realistic mesh. In both cases, we consider the conductivity σ_i of the different compartments Ω_i

in arbitrary units. The conductivity of the brain and of the scalp is set equal to 1. In this framework, the conductivity of the skull is equal to the conductivity ratio $\sigma_{skull}/\sigma_{brain}$. This parameter is controversial and its value varies upon the study between $1/15$ [76] and $1/80$ [50]. As in [75], we chose a conductivity ratio of $1/30$. Since this parameter influences the performances of the forward method, the localization error with respect to the conductivity ratio will also be studied. To assess the performance of the forward formulations, we will use the following relative localization error:

$$E_{loc} = \frac{|r_d - r_e|}{r_{brain}} \tag{3.24}$$

in spherical cases, where r_brain is the radius of the brain representing the brain layer, r_d is the true dipole position and r_e is the estimated dipole position. Furthermore, in spherical cases, the measurements will be generated using the analytical solution. The estimated dipole position is selected using $r_e = \max_{\mathbf{r}} \left(\hat{\mathbf{J}}(\mathbf{r}) \right)$. In this work, the error in the moment estimation has not been carried out.

3.4.2 Localization Ability in Noisy Context

One of the major problem in scalp EEG is the low signal-to-noise ratio (SNR) that makes the task of distinguishing between the signal that carries useful information and the other signals (system noise, muscle artifacts, background neuronal activity) difficult.

As sLORETA gives exact results for single dipole localization in a noiseless context, and has resulted in having the lowest localization error in noisy simulations [25], it is the inverse algorithm chosen here. White noise is added to the simulated data. The relative localization error ((3.24)) is computed for the usual and the mixed BEM methods. A unique dipole is placed in the center of the innermost sphere. The Signal-to-Noise Ratio (SNR) is increased from 0 dB to 18 dB in 1-dB increments. The SNR was defined as :

$$SNR = 20\, log(\frac{A(\Phi)}{\zeta}) \tag{3.25}$$

where $A(\Phi)$ stands for the root mean square amplitude of the noiseless simulated potential on the scalp surface and ζ is the standard deviation of the noise. The localization error is averaged over 200 simulations. The results presented below (Fig. 3.1) show that the new

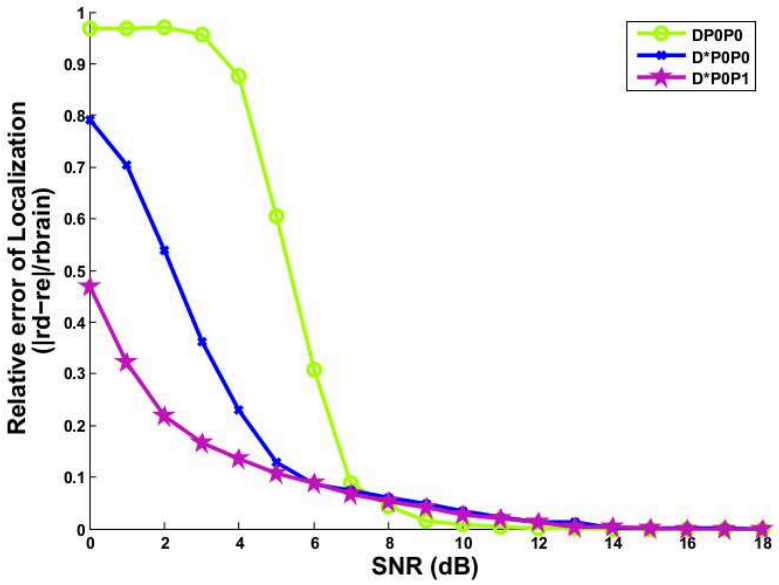

Figure 3.1: Localization error with respect to SNR, localization error is defined as $|r_d - r_e|$ where r_d stands for the true dipole position and r_e for the estimated dipole position

mixed discretization formulation is more resistant to noise than the usual ones.

3.4.3 Influence of the Active Region Parameters

3.4.3.1 Single Dipole Localization

We consider the case when only one region of the brain is active. This area is represented by a single active dipole of the dipoles grid. No noise was added to the simulated data. The estimation of the current distribution is obtain using sLORETA for the same reasons as before [80]. The active dipole is selected using : $r_e = \max_{\mathbf{r}} \left(\hat{\mathbf{J}}(\mathbf{r}) \right)$, if the dipole is away from a boundary, the exact dipole position can be found for every forward method.

3.4.3.2 Dipole Position

The BEM solutions to the forward problem presented in the section 3.1 have different behaviours in terms of accuracy when the dipole is moved closer to the surface of the

conducting body [101] and as can be also seen in Fig. 2.9. It could thus be expected that these differences impact the localization of the active region of the brain. We investigate here the ability to correctly detect a single active dipole whose position is moved to every point of the grid. Figures 3.2a, 3.2b and 3.2c, shows the localization error ((3.24)) for each dipole position when the source distribution is recovered using the different BEM forward methods to build the lead-field matrix $\mathbf{G}$. The inversion is done using sLORETA.

The source space is then divided into three subspaces containing respectively deep sources, mid-deep sources and surface sources. The sphere radius used to delimit the subspaces are 0.35 and 0.7. Table 3.2 shows the average localization error $\bar{E}_{loc}$ in each of these subspaces.

Formulation	$\bar{E}_{loc,deep}$	$\bar{E}_{loc,mdeep}$	$\bar{E}_{loc,surf}$	$\bar{E}_{loc}$
DP0P0	0	0.0313	0.1117	0.0670
D*P0P0	0	0.0089	0.1044	0.0532
D*P0P1	0	0	0.0186	0.0087

Table 3.2: Mean relative error of localization $\bar{E}_{loc}$ for deep sources (*deep*), mid-deep sources (*mdeep*), surfacic sources (*surf*) and overall error of localization.

3.4.3.3 Conductivity Ratio Between the Brain and the Scalp

As mentioned previously, the conductivity ratio $\sigma_{brain}/\sigma_{skull}$ is not an established parameter [56] [49]. Recent studies shows that a realistic conductivity ratio would be $1/15$ [76] whereas a ratio of $1/80$ is commonly used [50]. Yet, it has to be taken into account when the forward solution is built. We thus examine the localization ability of the different forward model for a single dipole localization case. The error of localization (3.24) is computed for every position of the grid and then averaged for every conductivity ratio. The brain and scalp conductivity is taken equal to 1. The values of σ_{skull} for which the study is carried out are $\{1/15;\ 1/30;\ 1/50;\ 1/80\}$. The inverse algorithm is sLORETA. The results are shown in Fig. 3.3.

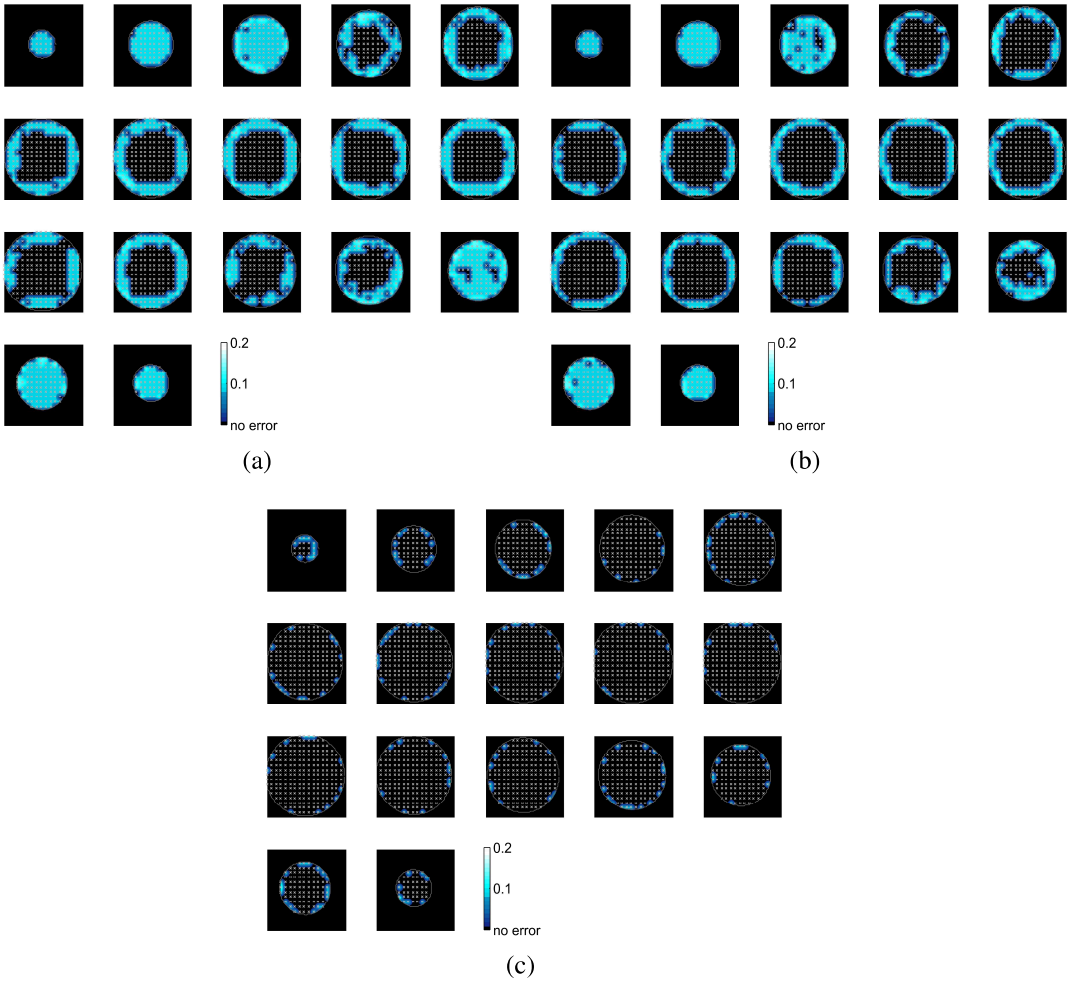

Figure 3.2: error of localization with respect to the dipole position using (a), DP_0P_0, (b), $D^*P_0P_0$, and (c), $D^*\tilde{P}_0\tilde{P}_1$ for the leadfield matrix construction. The dipole grid is displayed in grid points the brightest color designs the highest error of localization.

3.4.4 Source Reconstruction Using a Realistic Mesh

Finally, the performance in source localization are tested with a nested mesh obtained using simulated MRI data available from [20]. It consists of three layers standing for the brain, the skull and the scalp with respectively 5996, 5996, and 13426 triangular cells. The dipole grid that represents the potential solution lies in a layer that could be assimilated to the gray matter, situated 6 mm below the brain external interface. It was obtained by rescaling the brain layer. It contains 5996 dipoles oriented along the normal of the triangular mesh cells. The conductivity ratio $[\sigma_{brain} : \sigma_{skull} : \sigma_{scalp}]$ is taken equal to $[1 : 1/15 : 1]$ as in [76].

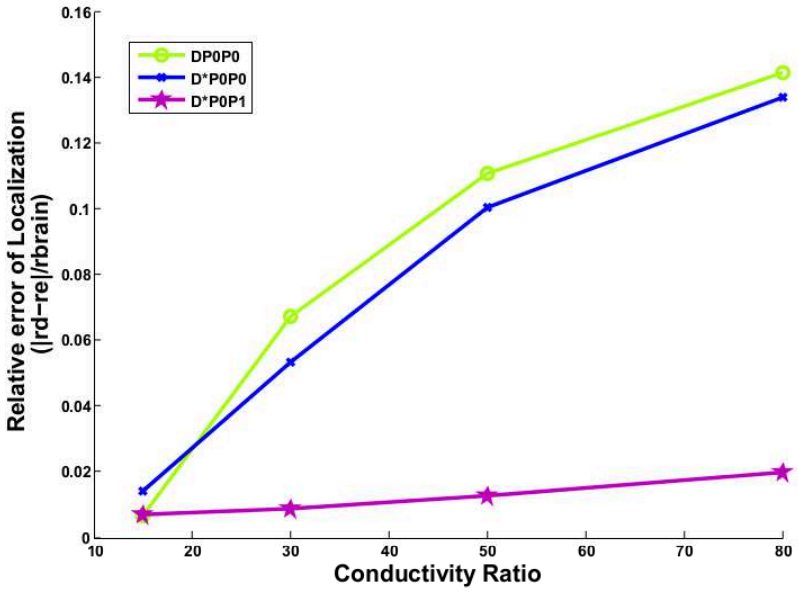

Figure 3.3: Mean error of localization with respect to the conductivity ratio for the different forward method

Measures are simulated at 256 points placed on the scalp and correspond to the potential generated by 3 active dipoles lying on the solution grid. Fig. 3.4a shows the considered geometry configuration: the brain, the skull and scalp layers as well as the electrodes positions. The measures are obtained by solving the forward problem using the standard adjoint double layer approach on the same geometry but with a denser mesh, composed of 43992 triangular cells in total. Fig. 3.4b shows the simulated potential on the brain surface. After solving the inverse problem with the three described leadfield methods, the potential on the brain is computed using the estimated source configuration. This potential that would be obtained if the recovered source would be the underlying source is displayed Fig. 3.5b, 3.5a and 3.5c for the methods D^*P0P0, $DP0P0$ and D^*P0P1 respectively.

3.5 Discussion and Conclusion

3.5.1 Localization in noisy environment

The figure Fig. 3.1 shows that the mixed discretization method gives a lower error of localization than the standard formulations when the SNR decreases. This difference begins

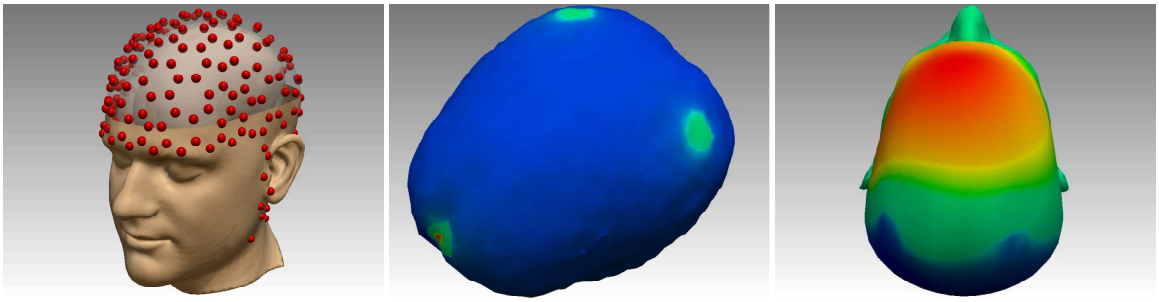

(a) (b) (c)

Figure 3.4: (a) : Three layers head with 256 electrodes, (b) and (c): simulated potential on the brain and on the scalp using the true source configuration.

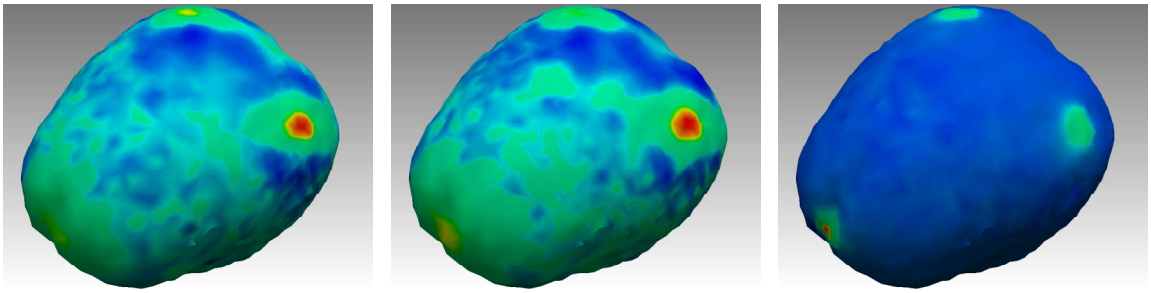

(a) (b) (c)

Figure 3.5: Estimated potential on the brain using (a) D^*P0P0, (b), $DP0P0$ and (c) D^*P0P1

to appear when the SNR becomes smaller than $15dB$. The SNR in scalp EEG can be very low, [93] estimates that it can reach 0.08. In this context having a forward formulation more stable in a noisy environment would be an asset for brain source investigation.

3.5.2 Influence of the Dipole Position

In section 3.4.3.2, the error of localization for all dipole positions of the grid has been computed, when only one dipole was active at a time. Fig. 3.2a, 3.2c and 3.2b show the distribution of this error on the dipole grid. It appears that, in average, for all dipole positions situated next to the boundary, i.e. at the brain surface, the active dipole is incorrectly localized, with a minimum relative error of localization ranging from 2% to 12%. When investigating the average error for three groups of dipoles : surface, mid-deep and deep dipoles, we find that all the methods are able to localize a unique dipole situated in the

”deep group”, and that the lowest error for surface dipoles is obtained when using the mixed single layer. The mixed-discretization scheme is the method that gives the lowest average error in total and for each group of sources. It then seems to be the best method to compute, in this case, the leadfield matrix.

3.5.3 Conductivity Ratio

The mean relative error of localization was investigated for different conductivity ratio between the brain and the skull. For all cases, the mixed single layer formulation showed better performances. We also note that while the average error rises considerably with the conductivity ratio for the double layer and mixed double layer formulation, the mean error of localization is nearly constant for the mixed formulation.

3.5.4 Conclusion

This chapter assessed the effect of mixed discretization for the EEG forward problem in solving the EEg inverse problem. The choice of this type of discretization is motivated by the spectral properties of the involved operators. It is shown that for localizing dipole sources close to the boundary, the mixed discretized double layer formulation is providing a better accuracy. When studying the resistance to noise, it can be seen that the mixed discretized formulation provides a lower localization error. Those results suggests that the choice of mixed discretization in solving the EEG forward problem would allow to get a better localisation ability in the case of single dipole localization. Results should be extended to the case of multiple sources localisation.

è

Chapter 4

A Proof of the Preconditioning Effect of Calderon Strategies for Multilayered Media

High resolution brain imaging necessitates to solve with a high accuracy the EEG forward problem. This means that the mesh used to model the geometry of the head should be very dense. Without any fast direct techniques, the high dimensions of the problem prevent the use of direct solvers and iterative solvers must be used. The precision of the solution obtained with an iterative solver as well as the rapidity of computation of the solution directly depends on the condition number of the system matrix. The contribution of this chapter is the introduction of Calderon preconditioning technique for multilayered media, and in particular the head. This technique enables to get a stable condition number with the mesh refinement by multiplying the system matrix with an operator which is spectrally equivalent to its inverse. The chapter will show how this well-known technique in high frequency can be extended to multilayered media for solving the Poisson's equation associated to the EEG forward problem.

4.1 Multiplicative Preconditioning Techniques and Calderon Identities

A common and efficient strategy to obtain high accuracy in solving an equation with numerical techniques is to increase the number of unknowns. Indeed, in this case more degrees of freedom are added both for describing the geometry and for expanding the solution and if correctly discretized, we can prove that the discrete solution tends to the continuous solution when the mesh refinement parameter goes to zero. However, for large numbers of unknowns, without any fast direct technique, the solution of a numerical system $\mathbf{Ax} = \mathbf{b}$ can only be obtained with iterative solvers. Indeed, denoting with N the number of unknowns, the complexity of a direct inversion is N^3 whereas for iterative solvers, this complexity is in the order of kN^2, where k is the number of iterations. When using an iterative solver, like conjugate gradient methods, the number of iterations necessary to obtain the solution for a given accuracy depends on the condition number of the matrix [94]. The condition number κ of a matrix $\mathbf{A}$ is the ratio of its highest singular value λ_{max} over its smallest singular value λ_{min}

$$\kappa(\mathbf{A}) = \frac{\lambda_{max}}{\lambda_{min}}. \tag{4.1}$$

This condition number usually depends on the mesh size. However, if it exists a symmetric and positive definite matrix $\mathbf{C}$ such that

$$a(\mathbf{Cu}, \mathbf{u}) \leqslant (\mathbf{Au}, \mathbf{u}) \leqslant b(\mathbf{Cu}, \mathbf{u}) \tag{4.2}$$

with a and b two constants independent from the mesh size then, $\kappa(\mathbf{C^{-1}A})$ will also be independent from the mesh size as can be seen using the Rayleigh quotient of $\tilde{\mathbf{A}} = \mathbf{C^{-1/2}AC^{-1/2}}$:

$$\lambda_{min}(\tilde{\mathbf{A}}) = min\frac{(\tilde{\mathbf{A}}\tilde{\mathbf{u}}, \tilde{\mathbf{u}})}{(\tilde{\mathbf{u}}, \tilde{\mathbf{u}})} \leqslant max\frac{(\tilde{\mathbf{A}}\tilde{\mathbf{u}}, \tilde{\mathbf{u}})}{(\tilde{\mathbf{u}}, \tilde{\mathbf{u}})} = \lambda_{max}(\tilde{\mathbf{A}})$$

with $\tilde{\mathbf{u}} = \mathbf{C^{1/2}u}$ we get

$$\lambda_{min}(\tilde{\mathbf{A}}) = min\frac{(\mathbf{Au}, \mathbf{u})}{(\mathbf{Cu}, \mathbf{u})} \leqslant max\frac{(\mathbf{Au}, \mathbf{u})}{(\mathbf{Cu}, \mathbf{u})} = \lambda_{max}(\tilde{\mathbf{A}}). \tag{4.3}$$

Hence, if $\mathbf{C}$ satisfies (4.2), then the system $\tilde{\mathbf{A}}\tilde{\mathbf{u}} = \mathbf{C^{-1/2}AC^{-1/2}}\tilde{\mathbf{u}} = \mathbf{C^{-1/2}b}$ has a condition number independent of the mesh size, majored by b/a. This remains true for $\tilde{\mathbf{A}} = \mathbf{C^{-1}A}$ since $\kappa(\mathbf{C^{-1/2}AC^{-1/2}}) = \kappa(\mathbf{C^{-1}A})$. It is very intuitive from (4.1) and (4.2) that if it is possible to find a matrix $\mathbf{C}$ spectrally equivalent to $\mathbf{A}$ then $\kappa(\mathbf{C^{-1}A})$ will be independent from the mesh size.

4.1.1 Compact Operators

In a closed domain Ω, with Lipschitz boundary Γ and outward pointing normal $\vec{n}$, consider the following differential equation

$$Lu = f \tag{4.4}$$

where L is the differential operator, u is the unknown function and f the datum. We also associate to (4.4) boundary conditions. The Green function associated to L will be denoted by G. As seen previously, in the introduction, we can associate to (4.4) an integral equation given by the second Green identity [94]

$$u(x) = \int_\Gamma G(x, x')\gamma_1^- u(x')dx' - \int_\Gamma \gamma_1^- G(x, x')u(x')dx' + \int_\Omega G(x, x')f(x')dx' \tag{4.5}$$

$\forall x \in \Omega$. It characterises u using only its boundary value $\gamma_0^- u$ and $\gamma_1^- u$. This integral equation gives rise to the integral formulation of the EEG forward problem when L is identified with the Laplace operator Δ. For the following developments, we need to define the integral operators [94]:

- the single layer operator $S : H^{-1/2}(\Gamma) \to H^{1/2}(\Omega)$

$$S\phi(r) = \int_\Gamma G(r, r')\phi(r')dr', \tag{4.6}$$

- the double layer operator $D : H^{1/2}(\Gamma) \to H^{1/2}(\Omega)$

$$D\psi(r) = \int_\Gamma \vec{n'}.\nabla G(r,r')\psi(r')dr', \tag{4.7}$$

- the adjoint double layer operator $D^* : H^{-1/2}(\Gamma) \to H^{-1/2}(\Omega)$

$$D^*\phi(r) = \int_\Gamma \vec{n}.\nabla G(r,r')\phi(r')dr', \tag{4.8}$$

- the hypersingular operator $N : H^{1/2}(\Gamma) \to H^{-1/2}(\Omega)$

$$N\psi(r) = \vec{n}.\nabla \int_\Gamma \vec{n'}.\nabla G(r,r')\psi(r')dr', \tag{4.9}$$

with $G(r,r') = \frac{1}{4\pi||r-r'||}$that arise naturally from (4.5). We also need the following definition [1]

Definition 4.1. The *spectrum* $\sigma(T)$ of a bounded operator $T : X \to X'$ is the set of all complex numbers λ such that the operator $\lambda\mathcal{I} - T$ is not invertible on X; with $\mathcal{I}$ the identity operator.

Definition 4.2. The complex number λ is an *eigenvalue* of T whenever there exist a non-zero vector x (*eigenvector*) such that $Tx = \lambda x$. We define σ_p the *point spectrum* of T such that $\sigma_p = \{\lambda \in \sigma(T) : Tx = \lambda x \text{ for some } x \neq 0\}$.

The set of all eigenvalues of a square matrix representing an operator in $\mathbb{R}^N$ (or $\mathbb{C}^N$) coincides with the point spectrum of the operator in $\mathbb{R}^N$ (or $\mathbb{C}^N$) that consists of the eigenvalues of the matrix.

Definition 4.3. An operator $T : X \to Y$ between Banach spaces is called *compact* if T carries norm bounded subsets of X to norm totally bounded subsets of Y.

It has the following properties

Proposition 4.1. *A bounded operator $T : X \to Y$ is compact iff for every bounded sequence $\{x_n\}$ of X, the sequence $\{Tx_n\}$ has a convergent subsequence in Y.*

Proposition 4.2. *If $T \in \mathcal{L}(x)$ is a compact operator then, for each $\epsilon > 0$ the set of all eigen values of T with modulus greater than ϵ (i.e. the set $\{\lambda \in \sigma_p : |\lambda| > \epsilon\}$) is finite.*

Proofs of the above properties can be found in [1]. It follows from proposition 4.2 that the set of eigen values of a compact operator is bounded and that it accumulates at zero.

We now describe some properties of the integral operators defined above. The single layer operator S is a compact operator of order -1 (acting like an integral), the condition number associated to its stiffness matrix $\mathbf{S}$ is then proportional to $1/h$ [94], with h the mesh parameter. Indeed, its highest singular value is stable while its smallest decreases with h. The hypersingular operator N is an operator of order $+1$ (acting like a derivative), this means that the smallest singular value of its stiffness matrix $\mathbf{N}$ is stable with the mesh refinement while its largest singular value increases with $1/h$ [94]. Summarizing, $\kappa(\mathbf{S}) = O(1/h)$ and $\kappa(\mathbf{N}) = O(1/h)$, this means that none of the stiffness matrix of these operators is well conditioned with respect to the mesh parameter. However, D and its adjoint D^* are compact operators [94], their spectrum is bounded and accumulates at zero. Their stiffness matrix would be ill-conditioned if they were used alone. However, D and D^* always appear in second kind integral equation. Since their spectrum is bounded, the matrix associated to the equation is always well conditioned. Indeed, the spectrum of the operator $\mathcal{I} + D$ or $\mathcal{I} + D^*$ will be bounded away from zero thanks to the identity operator. Moreover, given that D and D^* are bounded (by proposition 4.2), the spectra of $\mathcal{I} + D$ and $\mathcal{I} + D^*$ are also bounded. As a consequence, the associated system matrix is expected to be well conditioned (provided that the discrete basis used to build the matrices has some properties, as will be discussed in paragraph 4.1.3).

4.1.2 Calderon Identities

Applying the trace operators $\gamma_0^{\pm}$ and $\gamma_1^{\pm}$to the single layer potential S_Ω and the double layer potential D_Ω, defined such that $S_\Omega : H^{-1/2}(\Gamma) \to H^1(\Omega), S_\Omega\phi(r) = \int_\Gamma G(r,r')\phi(r')dr'$; and $D_\Omega : H^{1/2}(\Gamma) \to H^1(\Omega), D_\Omega\psi(r) = \int_\Gamma \vec{n'}.\nabla G(r,r')\psi(r')dr'$, we get

$$\gamma_0^{\pm} S_\Omega = \quad S \tag{4.10}$$

$$\gamma_0^{\pm} D_\Omega = \quad \pm\tfrac{1}{2}\mathcal{I} + D \tag{4.11}$$

$$\gamma_1^{\pm} S_\Omega = \quad \mp\tfrac{1}{2}\mathcal{I} + D^* \tag{4.12}$$

$$\gamma_1^{\pm} D_\Omega = \quad -N \tag{4.13}$$

Taking the trace of (4.5) and choosing u L-harmonic (i.e $Lu = 0$), we obtain

$$\gamma_0^{-} u = S\gamma_1^{-} u - \left(\frac{-1}{2}\mathcal{I} + D\right)\gamma_0^{-} u \tag{4.14}$$

and

$$\gamma_1^{-} u = \left(\frac{1}{2}\mathcal{I} + D^*\right)\gamma_1^{-} u + N\gamma_0^{-} u \tag{4.15}$$

In matrix form, this is equivalent to

$$\begin{pmatrix} \gamma_0^{-} u \\ \gamma_1^{-} u \end{pmatrix} = \begin{pmatrix} \frac{1}{2}\mathcal{I} - D & S \\ N & \frac{1}{2}\mathcal{I} + D^* \end{pmatrix} \begin{pmatrix} \gamma_0^{-} u \\ \gamma_1^{-} u \end{pmatrix} \tag{4.16}$$

then we can write

$$\begin{aligned} \begin{pmatrix} \gamma_0^{-} u \\ \gamma_1^{-} u \end{pmatrix} &= \begin{pmatrix} \frac{1}{2}\mathcal{I} - D & S \\ N & \frac{1}{2}\mathcal{I} + D^* \end{pmatrix} \begin{pmatrix} \gamma_0^{-} u \\ \gamma_1^{-} u \end{pmatrix} \\ &= \begin{pmatrix} \frac{1}{4}\mathcal{I} - D + D^2 + SN & S - DS + SD^* \\ N - ND + D^*N & \frac{1}{4}\mathcal{I} + D^* + D^{*^2} + NS \end{pmatrix} \begin{pmatrix} \gamma_0^{-} u \\ \gamma_1^{-} u \end{pmatrix} \end{aligned} \tag{4.17}$$

By identification of the coefficients, we obtain the so-called Calderon identities [92]

$$SN = \frac{1}{4}\mathcal{I} - D^2 \tag{4.18}$$

$$NS = \frac{1}{4}\mathcal{I} - D^{*2} \tag{4.19}$$

$$DS = SD^* \tag{4.20}$$

$$ND = D^*N. \tag{4.21}$$

The first two identities ((4.18) and (4.19)) can be used to build a well conditioned system matrix : by multiplying the hypersingular operator N with the single layer operator S,(or vice-versa), one can build an operator spectrally equivalent to an identity and thus the discrete system associated to SN (or NS) can be well conditioned.

4.1.3 Discretization

Solving integral equations obtained using the above operators, is carried out using numerical techniques. This means that we will actually never face the continuous operator $A : V \to W$ but always its discrete version $\mathbf{A}$, a square matrix which entries are given by the duality product:

$$[\mathbf{A}]_{ij} =< \psi_i, A\phi_j > \tag{4.22}$$

with $\{\phi_k\} = V_h$ and $\{\psi_k\} = W_h'$ two suitably chosen sets of basis functions. When doing this discretization as said in previous chapters, one must first ensure that V_h belongs to the domain of A and that W_h' is in the dual of the range of A [94]. Moreover, if $\mathbf{A}$ is to be preconditioned with $\mathbf{C^{-1}}$, the set of basis functions $\{\Psi_k\} = W_h$ used to discretize $C^{-1} : W \to V$ to build $\mathbf{C^{-1}}$ should also be chosen carefully : the pairing connecting W_h and V_h must be stable [47]. Denoting with $\mathbf{G}$ the gram matrix associated to this pairing

$$[\mathbf{G}]_{ij} =< \phi_i, \Psi_j >, \tag{4.23}$$

the previous idea can be formalized with the following theorem [47]

Theorem 4.1. *Under the assumptions that*

$$\sup_{\phi_k \in V_h} \frac{| < \psi_k, A\phi_k > |}{||\phi_k||} \geqslant c_A ||\psi_k|| \quad \forall \psi_k \in W_h \tag{4.24}$$

$$\sup_{\psi_k \in V_h} \frac{| < \phi_k, C^{-1}\psi_k > |}{||\psi_k||} \geqslant c_{C^{-1}} ||\phi_k|| \quad \forall \phi_k \in V_h \tag{4.25}$$

$$\sup_{\Psi_k \in T_h} \frac{| < \psi_k, \Psi_k > |}{||\Psi_k||} \geqslant c_G ||\psi_k|| \quad \forall \psi_k \in W_h \tag{4.26}$$

and provided that $dim(W_h) = dim(T_h)$*, we have*

$$\kappa(\mathbf{G^{-1}C^{-1}G^{-1}A}) \leqslant c_1 \tag{4.27}$$

with c_A*,* $c_{C^{-1}}$*,* c_G *and* c_1 *real constants independent of the mesh parameter* h*.*

This shows that suitable sets of basis functions are also necessary to ensure good preconditioning of a system matrix.

Now that the basic theory on preconditioning is set up, we can present the preconditioning strategy for multilayer domains.

4.2 Preconditioning of Integral Equations associated to Multilayer Domains

We have previously presented the general strategy for preconditioning an operator $A : V(\Gamma) \to W(\Gamma)$, when Γ is made of a unique surface. We will now show that the same idea can be extended to multilayer domains by considering a closed domain $\Omega = \cup_{i=1}^{N} \Omega_i$ with Lipschitz boundary $\Gamma = \partial\Omega = \cup_{i=1}^{N} \Gamma_i$ where $\Gamma_i = \partial\Omega_i$. The strategy will be the following:

- (i) Since the geometric domain is decomposed into different boundaries Γ_i, we will first show that if $\mathcal{K}_{12} : Y \to X$ and $\mathcal{K}_{21} : X \to Y$ are two compact operators then $\mathcal{K} = \begin{pmatrix} 0 & \mathcal{K}_{12} \\ \mathcal{K}_{21} & 0 \end{pmatrix} : X \oplus Y \to X \oplus Y$ is a compact operator.
- (ii) For our operators, S and N, we will build, using the Calderon identities, an endomorphism $C^{-1}A : V(\Gamma) \to V(\Gamma)$ such that $C^{-1}A = \alpha\mathcal{I} + \mathcal{K}$, where $\mathcal{K}$ is a compact operator and α a real constant. This will show that the Calderon identities (4.18) and (4.19) can be extended to multilayer domains.

4.2.1 Compactness of the 2 X 2 block operator

The *direct sum normed space* is the cartesian product of the normed spaces $X_1 \times X_2 ... \times X_N$ equipped with the norm $||(x_1, x_2, ..., x_n)|| = (\sum_{i=1}^{N} ||x_i||_{X_i}^2)^{1/2}$ [1]. It is denoted with $X_1 \oplus X_2 ... \oplus X_N$. In particular, a norm in the space $X \oplus Y$ is given by $(||x||_X^2) + ||y||_Y^2)^{1/2}$.

Proposition 4.3. *If $\mathcal{K}_{12} : Y \to X$ and $\mathcal{K}_{21} : X \to Y$ are two compact operators then $\mathcal{K} = \begin{pmatrix} 0 & \mathcal{K}_{12} \\ \mathcal{K}_{21} & 0 \end{pmatrix} : X \oplus Y \to X \oplus Y$ is a compact operator.*

Proof. Let $\{u_n\}$ be a bounded sequence in $X \oplus Y$: $||u_n||_{X \oplus Y} \leq c$ with c a real positive constant. $\{u_n\} = \{(x_n, y_n)\}$ with $x_n \in X$ and $y_n \in Y$.

$||u_n||_{X \oplus Y} \leq c$

$\Leftrightarrow ||(x_n, y_n)||_{X \oplus Y} \leq c$

$\Leftrightarrow ||x_n||_X^2 + ||y_n||_Y^2 \leq c^2$

$\Leftrightarrow \{x_n\}$ and $\{y_n\}$ are bounded in X and Y respectively (otherwise the above inequality would not be true).

Using proposition 4.1, as $\mathcal{K}_{12}$ is compact and $\{y_n\}$ is bounded, the sequence $\{\mathcal{K}_{12} y_n\}$ has a convergent subsequence $\{\mathcal{K}_{12} y_r\}$, $\mathcal{K}_{12} y_r \xrightarrow[r \to \infty]{} l_x \in X \Leftrightarrow \forall \epsilon > 0 \ \exists N$ such that $\forall r > N \ ||\mathcal{K}_{12} y_r - l_x||_x < \epsilon$.

Then, consider x_r bounded. By proposition 4.1 again, since K_{21} is compact, $\{\mathcal{K}_{21} x_r\}$ has a convergent subsequence $\{K_{21} x_{rr'}\}$, $\mathcal{K}_{21} x_{rr'} \xrightarrow[rr' \to \infty]{} l_y \in Y \Leftrightarrow \forall \epsilon > 0 \ \exists \ N'$ such that $\forall rr' > N' \ ||\mathcal{K}_{21} x_{rr'} - l_y||_y < \epsilon$.

As a consequence, for the two subsequences $\{\mathcal{K}_{12} y_{rr'}\}$ and $\{\mathcal{K}_{21} x_{rr'}\}$, we have, $\forall \epsilon > 0 \ \exists \ N''(= max(N, N'))$ such that $\forall rr' > N''$, $||\mathcal{K}_{12} y_{rr'} - l_x||_x < \epsilon$ and $||\mathcal{K}_{21} x_{rr'} - l_y||_y < \epsilon$. This remains true for $\epsilon' = \sqrt{2}\epsilon/2$.

Then, for all $\{u_n\}$ bounded in $X \oplus Y$, there exists a subsequence $\{u_{rr'}\} = \{x_{rr'}, y_{rr'}\}$

such that $\forall \epsilon > 0\ \exists N''$ such that $\forall rr' > N''$

$$\begin{aligned}
||\mathcal{K}u_{rr'} - \begin{pmatrix} l_x \\ l_y \end{pmatrix}||_{X\oplus Y} &= ||(\mathcal{K}_{12}y_{rr'} - l_x, \mathcal{K}_{21}x_{rr'} - l_y)||_{X\oplus Y} \\
&= (||\mathcal{K}_{12}y_{rr'} - l_x||_X^2 + ||\mathcal{K}_{21}x_{rr'} - l_y||_Y^2)^{1/2} \\
&< ((\sqrt{2}\epsilon/2)^2 + (\sqrt{2}\epsilon/2)^2)^{1/2} \\
&= (2\epsilon^2/4 + 2\epsilon^2/4)^{1/2} \\
&= \epsilon
\end{aligned}$$

(as $\forall \epsilon' = \sqrt{2}\epsilon/2 > 0\ \exists N''$ such that $\forall rr' > N''$, $||\mathcal{K}_{12}y_{rr'} - l_x||_X < \epsilon' = \sqrt{2}\epsilon/2$ and $||\mathcal{K}_{21}x_{rr'} - l_y||_Y < \epsilon' = \sqrt{2}\epsilon/2$)

And so, $\forall \{u_n\}$ bounded in $X \oplus Y$, there exists a subsequence $\{\mathcal{K}u_{rr'}\}$ that converges in $X \oplus Y \Leftrightarrow \mathcal{K}$ is compact, by proposition 4.1. □

By induction proposition 4.3 can be extended to $N \times N$ block operators since the sum of two compact operators is compact. We then have the following result:

Proposition 4.4. *The block operator $\mathcal{K} : X_1 \oplus X_2 ... \oplus X_N \to X_1 \oplus X_2 ... \oplus X_N$ with 0 on its diagonal and whose off-diagonal blocks $\mathcal{K}_{ij}$, $i \neq j$ are compact operators, is a compact operator.*

4.2.2 Calderon identities for multilayers domains

In this paragraph, we show that the Calderon identities (4.18) and (4.19) can be extended to precondition the operators $\mathcal{S} : \bigoplus_{i=1}^N H(\Gamma_i)^{-1/2} \to \bigoplus_{i=1}^N H(\Gamma_i)^{1/2}$ and $\mathcal{N} : \bigoplus_{i=1}^N H(\Gamma_i)^{1/2} \to \bigoplus_{i=1}^N H(\Gamma_i)^{-1/2}$. In the following, the operator T_{ij} will denote an operator $T : X(\Gamma_i) \to Y(\Gamma_j)$, acting between two surfaces Γ_i and Γ_j.

Proposition 4.5. *For the block operators $\mathcal{S} : \bigoplus_{i=1}^N H(\Gamma_i)^{-1/2} \to \bigoplus_{i=1}^N H(\Gamma_i)^{1/2}$ and $\mathcal{N} : \bigoplus_{i=1}^N H(\Gamma_i)^{1/2} \to \bigoplus_{i=1}^N H(\Gamma_i)^{-1/2}$ the following equalities holds*

$$\mathcal{S}\mathcal{N} = \frac{1}{4}\mathcal{I} - \mathcal{K} \tag{4.28}$$

$$\mathcal{N}\mathcal{S} = \frac{1}{4}\mathcal{I} - \mathcal{K}^*, \tag{4.29}$$

with $\mathcal{K} : \bigoplus_{i=1}^{N} H(\Gamma_i)^{1/2} \to \bigoplus_{i=1}^{N} H(\Gamma_i)^{1/2}$ *and* $\mathcal{K}^* : \bigoplus_{i=1}^{N} H(\Gamma_i)^{-1/2} \to \bigoplus_{i=1}^{N} H(\Gamma_i)^{-1/2}$ *two compact operators.*

Proof. We only prove (4.28) since the reasoning for (4.29) is the same exchanging $\mathcal{S}$ and $\mathcal{N}$. Let's decompose the block operators $\mathcal{S}$ and $\mathcal{N}$ into diagonal blocks (subscript $_D$) and non diagonal blocks (subscript $_{ND}$):

$$\mathcal{S} = \mathcal{S}_{\mathcal{D}} + \mathcal{S}_{\mathcal{ND}}$$

$$\mathcal{N} = \mathcal{N}_{\mathcal{D}} + \mathcal{N}_{\mathcal{ND}}$$

then

$$\mathcal{SN} = \mathcal{S}_{\mathcal{D}}\mathcal{N}_{\mathcal{D}} + \mathcal{S}_{\mathcal{ND}}\mathcal{N}_{\mathcal{D}} + \mathcal{S}_{\mathcal{D}}\mathcal{N}_{\mathcal{ND}} + \mathcal{S}_{\mathcal{ND}}\mathcal{N}_{\mathcal{ND}}$$

Since the Green function is analytic away from the origin, S_{ij}, $i \neq j$ has eigenvalues which accumulate at zeros and is compact. By proposition 4.4, $\mathcal{S}_{\mathcal{ND}}$ and $\mathcal{N}_{\mathcal{ND}}$ are compact operators. Moreover, given that the product of two linear operators in which at least one factor is compact is compact [92, Lemma 2.1.29], we have that $\mathcal{S}_{\mathcal{ND}}\mathcal{N}_{\mathcal{D}}$, $\mathcal{S}_{\mathcal{ND}}\mathcal{N}_{\mathcal{ND}}$ and $\mathcal{S}_{\mathcal{D}}\mathcal{N}_{\mathcal{ND}}$ are compacts.We hence just need to study the term $\mathcal{S}_{\mathcal{D}}\mathcal{N}_{\mathcal{D}}$. Using the Calderon identity (4.18), we have:

$$S_{ii}N_{ii} = \frac{1}{4}\mathcal{I}_{ii} - D_{ii}^2 \Leftrightarrow \mathcal{S}_{\mathcal{D}}\mathcal{N}_{\mathcal{D}} = \frac{1}{4}\mathcal{I} - {\mathcal{D}_{\mathcal{D}}}^2$$

where $\mathcal{D}_{\mathcal{D}}$ is a block diagonal operator whose entries are given by D_{ii} and is therefore compact. Then

$$\mathcal{SN} = \frac{1}{4}\mathcal{I} - {\mathcal{D}_{\mathcal{D}}}^2 + \mathcal{S}_{\mathcal{ND}}\mathcal{N}_{\mathcal{D}} + \mathcal{S}_{\mathcal{D}}\mathcal{N}_{\mathcal{ND}} + \mathcal{S}_{\mathcal{ND}}\mathcal{N}_{\mathcal{ND}}$$

$$\mathcal{SN} = \frac{1}{4}\mathcal{I} - \mathcal{K}$$

with $\mathcal{K} = {\mathcal{D}_{\mathcal{D}}}^2 - \mathcal{S}_{\mathcal{ND}}\mathcal{N}_{\mathcal{D}} - \mathcal{S}_{\mathcal{D}}\mathcal{N}_{\mathcal{ND}} - \mathcal{S}_{\mathcal{ND}}\mathcal{N}_{\mathcal{ND}}$. As a consequence, $\mathcal{K}$ is compact as a sum of compact operators. □

4.3 Application to the Calderon Preconditioning of the EEG forward problem

In solving the EEG forward problem, many integral formulations have been proposed. In particular, the symmetric formulation presented in [54], shows a high accuracy with respect to the other usual BEM formulations, like the double layer, the adjoint double layer [43] and the isolated skull approach [96]. It is now implemented in many EEG softwares like [77, 36, 97, 23]. However, different from other integral equations which are by nature of second kind, the symmetric formulation is a first kind integral equation. This means that the number of iterations necessary for the iterative solver to solve the matrix system associated to the problem increases with the mesh refinement parameter. This could prevent the use of this accurate formulation for high mesh density such as those that can be obtained directly from MRI data which have hundreds of thousands of unknowns [3]. However, as a part of his PhD work, Mr. J.E. Ortiz Guzman has proposed a Calderon formula to precondition the symmetric formulation. The new theory developed in this chapter can be used to rigorously prove the effectiveness of such an approach which will be briefly reported here for the sake of the understanding. It should be noted that, while the theory proving the preconditioned effect is one of the original contributions of this Thesis, the numerical results have been obtained by Mr. J.E. Ortiz Guzman.

4.3.1 The symmetric formulation for the EEG forward Problem

In order to model the head media, we consider a three layer nested domain $\Omega = \bigcup_{i=1}^{3} \Omega_i$ whose boundaries $\partial\Gamma_i = \Omega_i \cap \Omega_{i+1}$ are Lipschitz and have an outwards pointing normal $\vec{n}$. The external domain is given by $\Omega^c = \Omega_4$. The considered geometry is depicted in Figure 4.1. This geometry usually represents the brain, the skull and the scalp [43].

As we dealt with the EEG forward problem in the previous chapters, we recall here only succinctly the main technical information that is necessary to present the preconditioner.

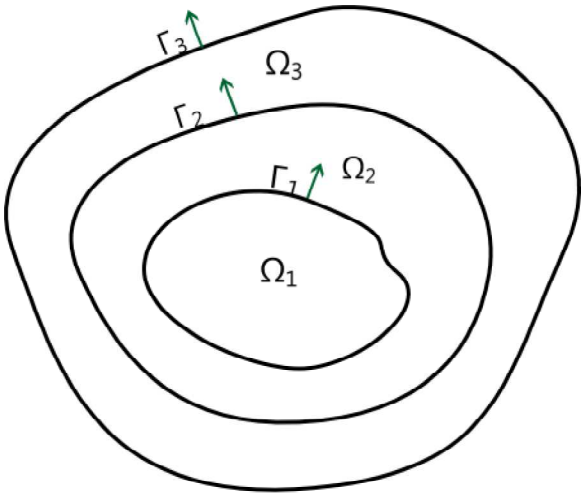

Figure 4.1: Geometry under consideration.

For isotropic conductivities, the EEG forward problems reads [91]

$$\sigma \Delta V = \nabla \cdot j \tag{4.30}$$

where σ is the conductivity and j the current sources. The isotropic conductivity is assumed to be piecewise homogeneous: in Ω_i, $\sigma = \sigma_i$. Furthermore, following [72], we model the current sources with dipoles. We then have $\nabla \cdot j = q_j \cdot \nabla \delta_{r_j}$, where q_j is the electric dipole moment and r_j is the position of the dipolar source. The following boundary conditions [91]:

$$[V]_i = 0 \ \forall i < N \tag{4.31a}$$

$$[\sigma \vec{n} \nabla V]_i = 0 \ \forall i \leq N \tag{4.31b}$$

that enforce the continuity of the potential and of its normal derivative between the different layers of the domain Ω, assure the solvability of (4.30).

The fundamental solution associated to (4.30) is [94]

$$G(r - r') = \frac{1}{4\pi ||r - r'||} \tag{4.32}$$

This is the Green's function that should be used to derive the operators S (4.6), D (4.7), D^* (4.8) and N (4.9) in this application scenario.

The symmetric formulation leverages on the existence of a harmonic function u such that $u = V - v_i/\sigma_i$ in Ω_i and $u = -v_i/\sigma_i$ in $R^3 \setminus \Omega_i$, where v_i is the solution of (4.30) in an unbounded medium. This is given by $v_i(r) = \int_{\Omega_i} f(r')G(r,r')dr'$. The representation theorem combined with the boundary conditions (4.31a) and (4.31b) gives rise to two integral equations [54]. They read:

$$\begin{aligned}\sigma_{i+1}^{-1}\left(v_{i+1}\right)_{\Gamma_i} - \sigma_i^{-1}\left(v_i\right)_{\Gamma_i} = D_{i,i-1}V_{i-1} - 2D_{ii}V_i + D_{i,i+1}V_{i+1} - \sigma_i^{-1}S_{i,i-1}p_{i-1} \\ + \left(\sigma_i^{-1} + \sigma_{i+1}^{-1}\right)S_{ii}p_i - \sigma_{i+1}^{-1}S_{i,i+1}p_{i+1}\end{aligned} \tag{4.33}$$

$$\begin{aligned}\left(\partial_n v_{i+1}\right)_{\Gamma_i} - \left(\partial_n v_i\right)_{\Gamma_i} = \sigma_i N_{i,i-1}V_{i-1} - \left(\sigma_i + \sigma_{i+1}\right)N_{ii}V_i + \sigma_{i+1}N_{i,i+1}V_{i+1} \\ - D^*_{i,i-1}p_{i-1} + 2D^*_{ii}p_i - D^*_{i,i+1}p_{i+1}.\end{aligned} \tag{4.34}$$

In the above equations, V_i is the unknown potential on the surface Γ_i and p_i is the jump of its derivative accross the surface Γ_i, $p_i = \sigma_i\left[\vec{n}\nabla V\right]_i$. A detailed explanation on the formulation is provided in [5].

Following the derivation of the integral equations, the numerical solution is obtained within the usual framework of the boundary element method : each surface Γ_i of the geometry is discretized into N_{t_i} triangles $\{t_k\}_{k=1}^{N_{t_i}}$ and N_{v_i} vertices $\{v_k\}_{k=1}^{N_{v_i}}$. On the surface Γ_i the unknowns V_i is discretized with patch basis functions P_0, $V_i = \sum_l^{N_v} a_k P_{1l}$ and the second unknown p_i is expanded with piecewise linear basis functions P_1, $p_i = \sum_l^{N_t} b_l P_{0l}$. The operators matrices we obtain are given by

$$[\mathbf{D}_{ij}]_{kl} =< P_{0k}, D_{ij}(P_{1l}) > \tag{4.35a}$$

$$[\mathbf{S}_{ij}]_{kl} =< P_{0k}, S_{ij}(P_{0l}) > \tag{4.35b}$$

$$[\mathbf{N}_{ij}]_{kl} =< P_{1k}, N_{ij}(P_{1l}) > \tag{4.35c}$$

$$[\mathbf{D^*}_{ij}]_{kl} =< P_{1k}, D^*_{ij}(P_{0l}) > \tag{4.35d}$$

Note that the expansion and testing functions $\{P_{0_i}\}$ and $\{P_{1_i}\}$ are in the domain and in the the dual of the range of the operators (4.6), (4.7), (4.8) and (4.9). Finally, we obtain the following system : $\mathbf{Zx} = \mathbf{b}$ with $\mathbf{Z}$ usually given by

$$\mathbf{Z} = \begin{pmatrix} (\sigma_1+\sigma_2)\mathbf{N}_{11} & -2\mathbf{D}^*{}_{11} & -\sigma_2\mathbf{N}_{12} & \mathbf{D}^*{}_{12} & 0 \\ -2\mathbf{D}_{11} & \left(\sigma_1^{-1}+\sigma_2^{-1}\right)\mathbf{S}_{11} & \mathbf{D}_{12} & -\sigma_2^{-1}\mathbf{S}_{12} & 0 \\ -\sigma_2\mathbf{N}_{21} & \mathbf{D}^*{}_{21} & (\sigma_2+\sigma_3)\mathbf{N}_{22} & -2\mathbf{D}^*{}_{22} & -\sigma_3\mathbf{N}_{23} \\ \mathbf{D_{21}} & -\sigma_2^{-1}\mathbf{S}_{21} & -2\mathbf{D}_{22} & \left(\sigma_2^{-1}+\sigma_3^{-1}\right)\mathbf{S}_{22} & \mathbf{D}_{23} \\ 0 & 0 & -\sigma_3\mathbf{N}_{32} & \mathbf{D}^*{}_{32} & (\sigma_3+\sigma_4)\mathbf{N}_{33} \end{pmatrix} \tag{4.36}$$

and where

$$[\mathbf{x}]_{2l-1} = a_l \tag{4.37a}$$

$$[\mathbf{x}]_{2l} = b_l \tag{4.37b}$$

$$[\mathbf{b}]_{2k-1} = -\int_{t_k} \left(\partial_n v_{k+1} - \partial_n v_k\right) P_{0k} dr \tag{4.38a}$$

$$[\mathbf{b}]_{2k} = \int_{\mu_k} \left(\sigma_{k+1}^{-1} v_{k+1} - \sigma_k^{-1} v_k\right) P_{1k} dr. \tag{4.38b}$$

We are now equipped to present the application of the Calderon preconditioner the EEG symmetric formulation.

4.3.2 Calderon Multiplicative Preconditioner

It is evident from (4.33), (4.34) that the integral equation associated to the symmetric formulation is of first kind. This means that its system matrix (4.36) suffers from ill-conditioning that can lead to the non-convergence of the employed iterative solver used to compute the solution [8]. The analysis of the operators carried out in section 4.1.1 shows that the single layer operator S and the hypersingular operator N have a condition number that increases with the inverse of the mesh length h. Since these operators constitute the diagonal blocks of the system matrix $\mathbf{Z}$, and that the off-diagonal blocks of the matrix (made of the compact operators D_{ij}, D_{ij}^* S_{ij}, N_{ij} cf sections 4.1.1 and 4.2) are

smoother, the overall condition number of the matrix $\mathbf{Z}$ will increase with the mesh refinement. However, we have seen in section 4.2 that we can precondition the operators $S : \bigoplus_{i=1}^{N} H(\Gamma_i)^{-1/2} \to \bigoplus_{i=1}^{N} H(\Gamma_i)^{1/2}$ and $N : \bigoplus_{i=1}^{N} H(\Gamma_i)^{1/2} \to \bigoplus_{i=1}^{N} H(\Gamma_i)^{-1/2}$ using the Calderon identities (4.28) and (4.29). This property can be exploited to build a left preconditioner for the symmetric operator Z.

Reorganizing the matrix $\mathbf{Z}$ permits to separate the contribution of each block operator.

$$\mathbf{Z} = \begin{pmatrix} (\sigma_1+\sigma_2)\mathbf{N}_{11} & -\sigma_2\mathbf{N}_{12} & 0 & -2\mathbf{D^*}_{11} & \mathbf{D^*}_{12} \\ -\sigma_2\mathbf{N}_{21} & (\sigma_2+\sigma_3)\mathbf{N}_{22} & -\sigma_3\mathbf{N}_{23} & \mathbf{D^*}_{21} & -2\mathbf{D^*}_{22} \\ 0 & -\sigma_3\mathbf{N}_{32} & (\sigma_3+\sigma_4)\mathbf{N}_{33} & 0 & \mathbf{D^*}_{32} \\ -2\mathbf{D}_{11} & \mathbf{D}_{12} & 0 & \left(\sigma_1^{-1}+\sigma_2^{-1}\right)\mathbf{S}_{11} & -\sigma_2^{-1}\mathbf{S}_{12} \\ \mathbf{D_{21}} & -2\mathbf{D}_{22} & \mathbf{D}_{23} & -\sigma_2^{-1}\mathbf{S}_{21} & \left(\sigma_2^{-1}+\sigma_3^{-1}\right)\mathbf{S}_{22} \end{pmatrix} \tag{4.39}$$

Since the conductivity factors are constant, we can say that the mapping properties of the matrix $\mathbf{Z}$ are equivalent to the mapping properties of the following block operator:

$$Z' = \begin{pmatrix} \mathcal{N} & \mathcal{D}^* \\ \mathcal{D} & \mathcal{S} \end{pmatrix} \tag{4.40}$$

Then, multiplying (4.40) with

$$C' = \begin{pmatrix} \mathcal{S} & \mathcal{D} \\ \mathcal{D}^* & \mathcal{N} \end{pmatrix} \tag{4.41}$$

we obtain:

$$C'Z' = \begin{pmatrix} \mathcal{S}\mathcal{N} + \mathcal{D}\mathcal{D} & \mathcal{S}\mathcal{D}^* + \mathcal{D}\mathcal{S} \\ \mathcal{D}^*\mathcal{N} + \mathcal{N}\mathcal{D} & \mathcal{D}^*\mathcal{D}^* + \mathcal{N}\mathcal{S} \end{pmatrix} \tag{4.42}$$

Using the identities (4.28) and (4.29), we can deduce that $\mathcal{S}\mathcal{N}$ and $\mathcal{N}\mathcal{S}$ are well conditioned. The remaining terms, $\mathcal{D}\mathcal{D}$, $\mathcal{S}\mathcal{D}^*$,$\mathcal{D}\mathcal{S}$, $\mathcal{D}^*\mathcal{N}$, and $\mathcal{D}^*\mathcal{D}^*$ are compact operators (as product of operators in which one factor at least is compact). As a consequence, $\mathcal{S}\mathcal{N} + \mathcal{D}\mathcal{D}$ and $\mathcal{D}^*\mathcal{D}^* + \mathcal{N}\mathcal{S}$ are compact as well as $\begin{pmatrix} 0 & \mathcal{S}\mathcal{D}^* + \mathcal{D}\mathcal{S} \\ \mathcal{D}^*\mathcal{N} + \mathcal{N}\mathcal{D} & 0 \end{pmatrix}$ by using proposition 4.3. It follows that $C'Z$ is well conditionned. In the implementation, we reorganized the terms in C' to match those of (4.36). The preconditioner is then given by

$$C = \begin{pmatrix} c_{11}S_{11} & c_{12}D_{11} & c_{13}S_{12} & c_{14}D_{12} & 0 & 0 & 0 \\ c_{21}D^*_{11} & c_{22}N_{11} & c_{23}D^*_{12} & c_{24}N_{12} & 0 & 0 & 0 \\ c_{31}S_{21} & c_{32}D_{21} & c_{33}S_{22} & c_{34}D_{22} & c_{35}S_{23} & c_{36}D_{23} & 0 \\ c_{41}D^*_{21} & c_{42}N_{21} & c_{43}D^*_{22} & c_{44}N_{22} & c_{45}D^*_{23} & c_{46}N_{23} & 0 \\ 0 & 0 & c_{53}S_{32} & c_{54}D_{32} & c_{55}S_{33} & c_{56}D_{33} & \cdots \\ 0 & 0 & c_{63}D^*_{32} & c_{64}N_{32} & c_{65}D^*_{33} & c_{66}N_{33} & \cdots \\ 0 & 0 & 0 & 0 & \vdots & \vdots & \ddots \end{pmatrix}. \tag{4.43}$$

where the coefficients c_{ij} are constant taking into account the conductivity and are the same as in (4.36). To abide by theorem 4.1, the proposed Calderon preconditioner is discretized in the dual of the range of the involved operators (this choice also allows to perform the matrix multiplication correctly). This means that in (4.43), the operator matrices will be given by

$$[\mathbf{D}_{ij}]_{kl} =< \widetilde{P}_{0k}, D_{ij}(\widetilde{P}_{1l}) > \tag{4.44a}$$

$$[\mathbf{S}_{ij}]_{kl} =< \widetilde{P}_{0k}, S_{ij}(\widetilde{P}_{0l}) > \tag{4.44b}$$

$$[\mathbf{N}_{ij}]_{kl} =< \widetilde{P}_{1k}, N_{ij}(\widetilde{P}_{1l}) > \tag{4.44c}$$

$$[\mathbf{D^*}_{ij}]_{kl} =< \widetilde{P}_{1k}, D^*_{ij}(\widetilde{P}_{0l} > \tag{4.44d}$$

where $\widetilde{P}_0$ and $\widetilde{P}_1$ are respectively the dual patch basis functions and the dual pyramid functions, defined on the dual mesh. Dual patch basis functions are the piecewise constant basis functions defined on the dual mesh. This is also the choice that allows to perform the desired matrix multiplication. The preconditioned system is then given by

$$\mathbf{C}\mathbf{G}^{-1}\mathbf{Z}\mathbf{x} = \mathbf{C}\mathbf{G}^{-1}\mathbf{b} \tag{4.45}$$

where $\mathbf{C}$ is the matrix that corresponds to the discretization of the proposed preconditioner C using (4.44) and $\mathbf{G}$ is the Gram matrix linking the standard and dual basis functions.

4.3.3 Numerical Results

The new Calderon regularized symmetric formulation proposed in this work has been first tested on the canonical scenario of three homogeneous and concentric spheres of radii 0.8, 0.9, and 1 respectively. Indeed, in the case of homogeneous nested spheres, an analytical solution is available as a reference [26, 106], this solution will be denoted with V_{ref}. In these simulations, a single dipole source is placed in (0, 0, 0.5) with a dipole moment of (0, 0, 1). As a complement to these results, to validate the new formulation on a real case

scenario, the new formulation has been tested also on a realistic head model obtained from MRI data.

The first numerical experiments, whose results are plotted in Figure 4.2, shows that the proposed preconditioner provides the same solution as the unpreconditioned formulation. On this figure, we can also see that the symmetric formulation provides a more accurate solution than the double layer and adjoint double layer formulation.

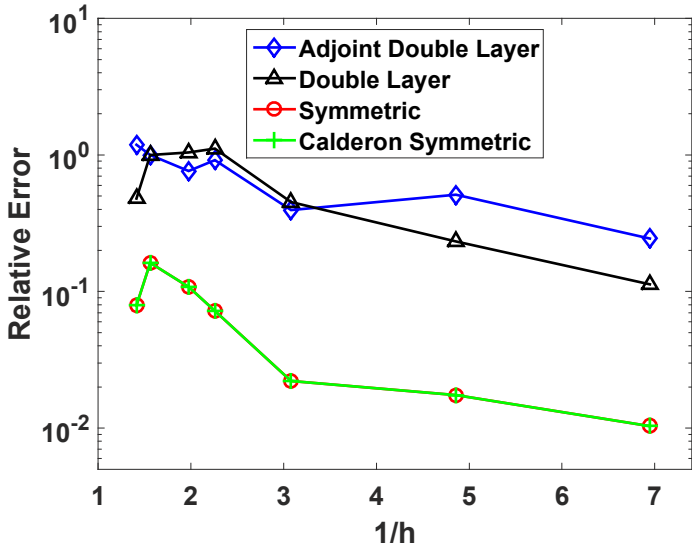

Figure 4.2: Relative error with respect to the mesh refinement. the average length of a cell is given by h.

4.3.3.1 Condition Number Assessments

We performed another set of numerical experiments to check the efficiency of the Calderon preconditioning technique. We used the same spherical three layers mesh and the source configuration as in the previous experiment for different level of refinement of the mesh and we compared the condition number of the system matrix. The results are shown Figure 4.3. It can be seen that for all levels of refinement, the condition number of the preconditioned solution stays stable whereas the condition number of the standard symmetric formulation is increasing with the mesh parameter (as expected).

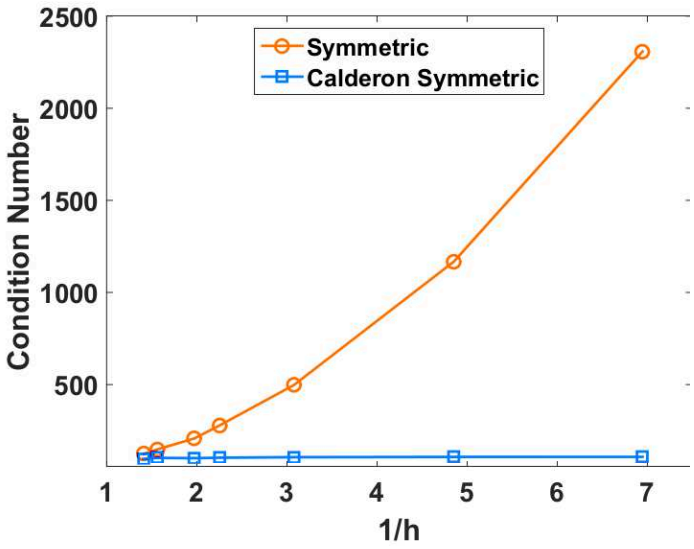

Figure 4.3: Condition Number with respect to the mesh refinement.

4.3.3.2 Assessments on a MRI-obtained head model

The last simulation shows the performances of the Calderon preconditioner in a realistic scenario. The mesh is obtained from MRI data using [77], it models the brain, the skull and the scalp. The potential is computed in 256 electrodes. Figure 4.4 shows the computed potential and the electrodes positions. The solution has been computed both with the standard symmetric formulation and the preconditioned formulation. The obtained potential is exactly the same as can be seen in Figure 4.5. Figure 4.6 shows the convergence of the residual error of the iterative solver (conjugate gradient square) with respect to the number of iterations. It can be seen that the Calderon symmetric approach converges 40 times faster than the non-preconditionned symmetric approach. This proves the effectiveness of the proposed Calderon preconditioner.

4.3.4 Discussion

This section proposes a Calderon preconditioner for the symmetric formulation of the EEG forward problem. the proposed preconditioner allows to accelerate the computation of the solution. However it should be noted that a trade off should be made between the time

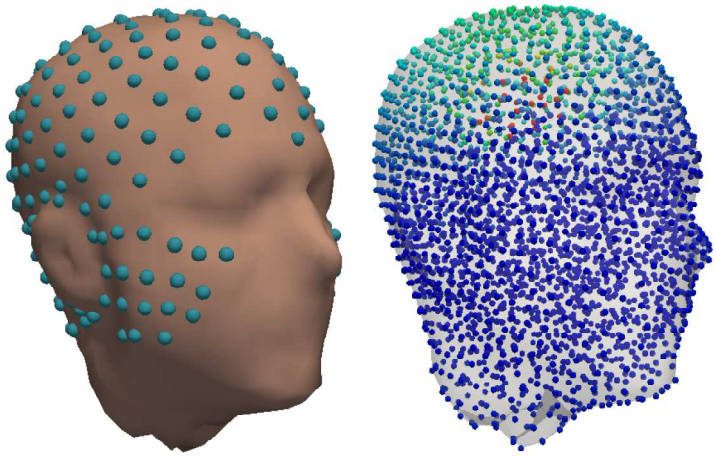

(a) Head model and EEG electrodes.

(b) Calculated electric potential.

Figure 4.4: MRI-obtained head model

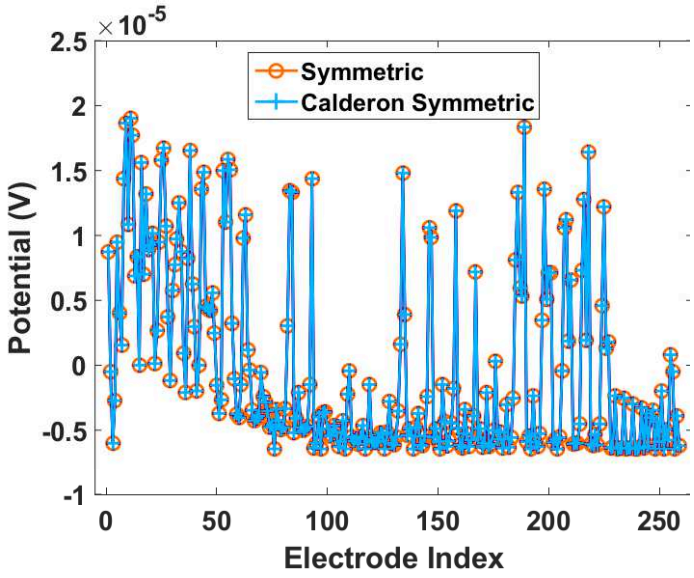

Figure 4.5: Validation of the new formulation via a potential comparison at the EEG electrodes' position (dipolar source).

necessary to build the proposed Calderon preconditioner and the gain in the computation of the solution. The size of the matrix associated to the preconditioner is the same as the size of the system matrix, therefore, the timing for building the whole preconditioned system is doubled (the gram matrices are block diagonal matrices and their computation is straightforward). The advantages of such a preconditioner may be more visible if a fast

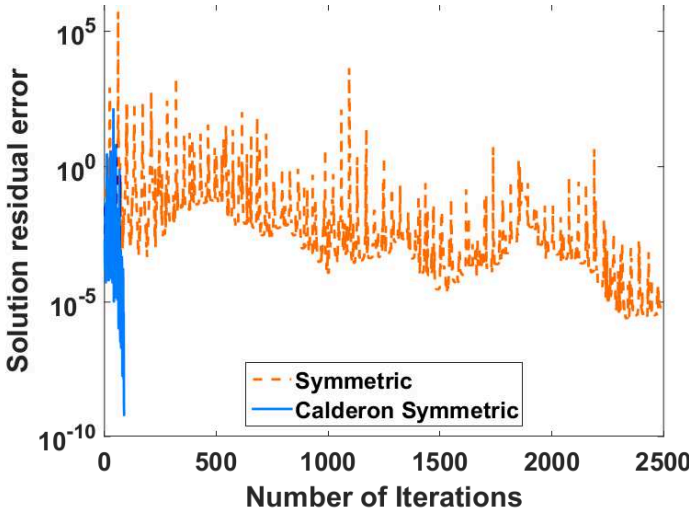

Figure 4.6: Convergence of the iterative solver for the preconditionned and not preconditioned symmetric approach

solver is used when building the overall system. Indeed in this case, the time associated to the building is less important and the crossing point, that is the size of the system from which it is interesting to use the preconditioned system should be smaller.

4.4 Conclusion

In this chapter we have shown that the Calderon identities traditionally used in high frequency problems such as in preconditioning the Electric Field Integral Equation can be used in static propblems. The chapter also contributes to prove theoretically that these identities can be extended to multilayers media. The application scenario, in the framework of solving the EEG forward problem demonstrates the efficiency of the proposed multilayer Calderon preconditioner. Future work intends to apply the multilayer Calderon identities to high frequency problems dealing with multi-compartments media.

Chapter 5

Wire Integral Equations : Preconditioning and Modelling of the White Matter Fiber

A Calderon preconditioner is introduced for the wire Electric Field Integral Equation. The idea of modelling wires with 1-D curves is extended to the brain. The chapter hence also presents a new integral equation for the EEG forward problem to take into account the anisotropy of the white matter fibers.

In modelling structures made of thin wires, the Electric Field Integral Equation (EFIE) [33] can be simplified into a one dimensional integral assuming that the current is constant in the azimuthal direction and that it flows parallel to the wire axis. The obtained equation inherits the properties of the surface EFIE. It is ill-conditioned both with respect to the frequency [22] (this phenomena is known as "low-frequency breakdown"), and with the mesh parameter ("dense discretization breakdown") since the two operators that compose the EFIE have singular values that accumulates at zeros and at infinity [70]. Quasi-helmholtz projectors, presented in [7], can be used to solve the low frequency breakdown for surface meshes. The idea was very recently and successfully extended to 1-D structures in [87]. To handle the ill-conditioning due to the mesh refinement in 2-D structures a multiplicative Calderon preconditioner have been proposed in [6]. The resulting integral equation has a

condition number that is constant with the mesh refinement. As said in the previous chapter, the idea behind Calderon preconditioning is to build an operator spectrally equivalent to an identity using operators of "opposite derivative strength". However, for thin wires, it can be shown that the usual Calderon preconditioning technique cannot be applied [14]. The rational behind this failure is that the spectral properties of the EFIE operator in 1D are not the same as in 2D. It can be shown that the 1-D EFIE operator has a spectral behavior that is equivalent to the Laplacian's one, see for example [14]. In other words, by losing one dimension, the EFIE operator gained one derivative order. After setting up definitions, we begin this chapter by studying the spectral properties of the wire EFIE. Special attention will be drawn to open curves. Indeed, in this case, using simply operators of "opposite order" is not sufficient anymore to build a system matrix whose condition number is stable with the mesh refinement parameter[63]. Taking into account the spectral properties of the 1-D EFIE operators in closed and open curves, a new Calderon preconditioning strategy is proposed. This Calderon preconditioner also takes care of the extremities effect. To build it, we used the modified single layer and hypersingular operators proposed by [51]. We show that our preconditioner can achieves a growth of the condition number of the wire EFIE in the order of $O(log(h))$ where h is the mesh parameter instead of $O(h^2)$.

5.1 Background on the wire EFIE

Let S denote the interface of a Perfect Electric Conductor (PEC) and $\hat{\boldsymbol{n}}$ its outwards pointing normal. The considered geometry and notations are shown in Figure 5.1. When illuminated by an incident electromagnetic field, the continuity of the tangential component of the total electric field gives the following equation

$$\hat{\boldsymbol{n}}(r) \times \boldsymbol{E}^s(r) = -\hat{\boldsymbol{n}}(r) \times \boldsymbol{E}^i(r) \tag{5.1}$$

where $\boldsymbol{E}^i$ is the incident electric field and $\boldsymbol{E}^s$ is the scattered field. Using Maxwell's equations the scattered field can be expressed in terms of scalar potential (V), vector potential

($\boldsymbol{A}$) and angular frequency (ω)

$$\boldsymbol{E}^s = -j\omega\boldsymbol{A} - \nabla V. \tag{5.2}$$

Using the Lorentz gauge

$$\nabla \cdot \boldsymbol{A} + j\omega\mu\epsilon V = 0, \tag{5.3}$$

we obtain

$$\boldsymbol{E}^s = -j\omega\boldsymbol{A} - \frac{j}{\omega\mu\epsilon}\nabla\nabla \cdot A. \tag{5.4}$$

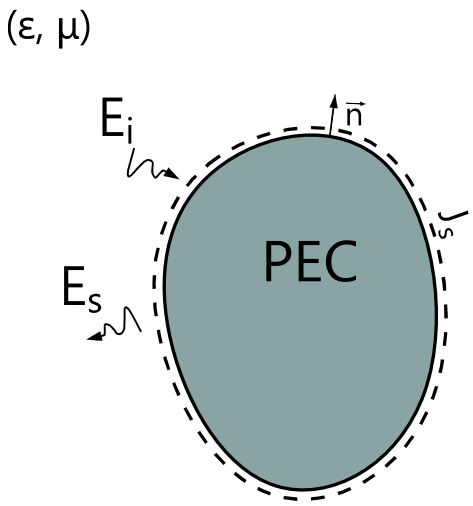

Figure 5.1: Description of the geometry for deriving the EFIE in the general case

Given that the vector potential is the solution of the Helmholtz equation (see [33] for example), we can express it using the associated Green's function,

$$\boldsymbol{A}(r) = \mu \int_S G(\mathbf{r} - \mathbf{r}')\boldsymbol{J}^s(\mathbf{r}')d\mathbf{r}' \tag{5.5}$$

where $\boldsymbol{J}^s$ are the surface currents created by the incident field and where the Green's function is given by (1.18)

$$G(\mathbf{r}) = \frac{e^{-jk|\mathbf{r}|}}{4\pi|\mathbf{r}|}. \tag{5.6}$$

This allows to obtain the scattered field given the surface currents. The obtained integral equation is known as the EFIE. Here, we assume that the considered PEC object can be

modelled by a thin wire. Under the assumption that the radius of the wire is small enough with respect to the wave length, ($a < 0.01\lambda$), the current can be assumed to vary only along the wire direction. This means that the structure can be simplified in a three dimensional curve. We denote this curve with Γ and by $\hat{\boldsymbol{t}}(\mathbf{r})$ the tangent to the curve in r. The curvilinear abscissa will be denoted with t (hence $\hat{\boldsymbol{t}}(\mathbf{r})$ depends only on t and we simplify the notation as $\hat{\boldsymbol{t}}(\mathbf{r}) = \hat{\boldsymbol{t}}(\mathbf{t}) = \hat{\boldsymbol{t}}$). The geometry is described Figure 5.2. Since we assume that the current is oriented along the wire $\boldsymbol{J}^s(\mathbf{r}) = \frac{I(t)\hat{\boldsymbol{t}}(\mathbf{r})}{2\pi a}$ with a the radius of the wire. Then using (5.4), the tangential component of the scattered electric field, denoted $\boldsymbol{E}_t^s$, can be rewritten as

$$\boldsymbol{E}_t^s = -j\omega\mu \int_\Gamma \int_0^{2\pi} G(\mathbf{r}-\mathbf{r}')d\theta \frac{I(t')\hat{\boldsymbol{t}'}}{2\pi}dt' - \frac{j}{\omega\mu\epsilon}\nabla\nabla\cdot \int_\Gamma \int_0^{2\pi} G(\mathbf{r}-\mathbf{r}')d\theta \frac{I(t')\hat{\boldsymbol{t}'}}{2\pi}dt' \quad (5.7)$$

$$\Leftrightarrow \boldsymbol{E}_t^s = -\left[j\omega\mu + \frac{j}{\omega\mu\epsilon}\nabla\nabla\cdot\right] \int_\Gamma \int_0^{2\pi} G(\mathbf{r}-\mathbf{r}')d\theta \frac{I(t')\hat{\boldsymbol{t}}}{2\pi}dt'. \quad (5.8)$$

The EFIE for thin wire now reads

$$\boldsymbol{E}_t^i = \left[j\omega\mu + \frac{j}{\omega\mu\epsilon}\nabla\nabla\cdot\right] \int_\Gamma K(\mathbf{r}-\mathbf{r}')\frac{I(t')\hat{\boldsymbol{t}'}}{4\pi}dt' \quad (5.9)$$

where $\boldsymbol{E}_t^i$ is the tangential component of the incident electric field, and where $K(\mathbf{r})$ is the kernel of the EFIE operator given by

$$K(\mathbf{r}-\mathbf{r}) = \frac{1}{2\pi}\int_0^{2\pi} \frac{e^{-jkR(\mathbf{r}-\mathbf{r})}}{R(\mathbf{r}-\mathbf{r}')}d\theta \quad (5.10)$$

with

$$R(\mathbf{r}-\mathbf{r}') = \sqrt{(t-t')^2 + \rho^2 + a^2 - 2\rho a\cos(\theta-\theta')} \quad (5.11)$$

in the cylindrical coordinate system described in Figure 5.2, ($\mathbf{r} = (\rho, \theta, t)$) if the wire is straight or simply

$$R(\mathbf{r}-\mathbf{r}') = ||\mathbf{r}-\mathbf{r}'|| \quad (5.12)$$

in general. Assuming that a is very small, $K(\mathbf{r}-\mathbf{r}')$ can be simplified to get the so-called reduced kernel [33]:

$$K_r(\mathbf{r}-\mathbf{r}') = \frac{e^{-jk||\mathbf{r}-\mathbf{r}'||}}{||\mathbf{r}-\mathbf{r}'||} \tag{5.13}$$

Two operators appear in the wire EFIE; the single layer operator

$$\mathcal{S}f(\mathbf{r}) = \int_\Gamma K(\mathbf{r}-\mathbf{r}')f(t')dt', \tag{5.14}$$

and the hypersingular operator

$$\mathcal{N}f(r) = \nabla \int_\Gamma K(\mathbf{r}-\mathbf{r}')\nabla\cdot f(t')dt'. \tag{5.15}$$

Boundary conditions enforce that the current vanishes at the extremities of the wire (if Γ is open). They read

$$I(\partial\Gamma) = 0 \tag{5.16}$$

Remark 5.1. In the context of boundary element methods, the observation point $\mathbf{r}'$ will be the point in which the testing function is evaluated. For the singular terms, the reduced kernel then becomes $K_r(\mathbf{r}-\mathbf{r}') = \frac{e^{jk||t-t'||}}{||t-t'||}$. It is well-known that $1/r$ is not an integrable function in one dimension. This is circumvented by placing the testing functions inside the center of the wire. In this way, the reduced kernel becomes $K_r(\mathbf{r}-\mathbf{r}') = \frac{e^{jk\sqrt{(t-t')^2+a^2}}}{\sqrt{(t-t')^2+a^2}}$. But this term does not contain singularity. From this point, it becomes self-evident that the EFIE operator in 1D with the reduced kernel cannot behave as the EFIE operator when the support of the operators is a smooth 2D manifold.

Remark 5.2. The low frequency breakdown of the EFIE can easily be seen by writing the EFIE operator such that

$$\mathcal{T} = \mathcal{T}_A + \mathcal{T}_\phi = j\omega\mu\mathcal{S} + \frac{j}{\omega\mu\epsilon}\mathcal{N} \tag{5.17}$$

where it is manifests that the two operators $\mathcal{T}_A$ and $\mathcal{T}_\phi$ scale differently with the frequency $f = \omega/2\pi$.

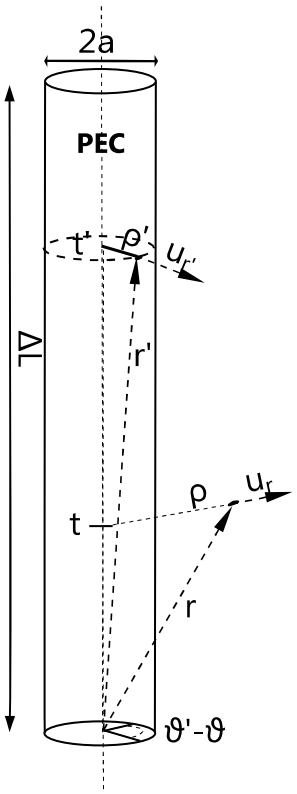

Figure 5.2: Notations for the cylindrical coordinates in case of a thin wire

In order to assess the spectral behavior of the wire EFIE operator, the following section analyses the spectral behaviour of those two operators for the two different kernels.

5.2 Analysis of the Spectral Behaviour

By computing the eigenvalues of the EFIE operator, [15] showed that the mapping properties of the EFIE operator with reduced kernel are approximately the same as the mapping properties of $-j\omega\mu\mathcal{I} + \frac{j}{\omega\mu\epsilon}\frac{d^2}{dt}$ that is to say $\mathcal{T} \approx +j\omega\mu\mathcal{I} + \frac{j}{\omega\mu\epsilon}\Delta$, where Δ is the Laplacian operator. We seek to elaborate this result rigorously.

We begin by studying the operators defined with the reduced kernel. The first of our

operator is $\mathcal{S}$ that reads

$$\begin{aligned}\mathcal{S}f(r) &= \int_\Gamma G(\mathbf{r},\mathbf{r}')f(\mathbf{r}')d\mathbf{r}' \\ &= \frac{1}{4\pi}\int_\Gamma \frac{e^{-jkR(\mathbf{r},\mathbf{r}')}}{R(\mathbf{r}-\mathbf{r}')}f(\mathbf{r}')d\mathbf{r}' \\ &= \frac{1}{4\pi}\int_\Gamma \frac{1}{R(\mathbf{r}-\mathbf{r}')}f(\mathbf{r}')d\mathbf{r}' + \frac{1}{4\pi}\int_\Gamma \frac{e^{-jkR(\mathbf{r}-\mathbf{r}'')}-1}{R(\mathbf{r}-\mathbf{r}')}f(\mathbf{r}')d\mathbf{r}'\end{aligned} \tag{5.18}$$

The second term on the right hand side of the above equation is continuous and has continuous derivatives. Therefore, it is a compact operator and it will not influence the mapping properties of the $\mathcal{S}$ operator. We therefore restrict our study to the term $S_1 = \int_\Gamma \frac{1}{R(r,r')}f(r')dr'$. Let $G_1(r) = \frac{1}{R(r,r')}$.

Definition 5.1. We define the *Fourier transform* $\mathcal{F}$ of a function f by $\mathcal{F}[f(x)] = \hat{f}(\xi) = \int_{-\infty}^{+\infty} f(x)e^{-j\xi x}dx$ and its inverse $\mathcal{F}^{-1}\left[\hat{f}(\xi)\right] = \frac{1}{2\pi}\int_{-\infty}^{+\infty}\hat{f}(\xi)e^{j\xi x}d\xi$.

Let's consider an infinite straight wire along the $z-$axis. In this case, S_1 is given by

$$\begin{aligned}S_1 f(z) &= \int_{-\infty}^{+\infty}\frac{1}{R(z,z')}f(z')dz' \\ \Leftrightarrow S_1 f(z) &= \frac{1}{R(z)} * f(z)\end{aligned}$$

where $*$ denotes the convolution. Then,

$$S_1 f(z) = \mathcal{F}^{-1}\left[\mathcal{F}\left[\frac{1}{R(z)}\right]\mathcal{F}[f(z)]\right]$$

Let's denote with ζ the eigen values of the operator S_1. To define the spectrum of S_1 we are looking for ζ such that

$$\begin{aligned}S_1 f &= \zeta f \\ \Leftrightarrow \mathcal{F}^{-1}\left[\mathcal{F}\left[\frac{1}{R(z)}\right]\mathcal{F}[f(z)]\right] &= \zeta f(z) \\ \Leftrightarrow \mathcal{F}\left[\frac{1}{R(z)}\right]\mathcal{F}[f(z)] &= \zeta\mathcal{F}[f(z)] \\ \Leftrightarrow \mathcal{F}\left[\frac{1}{R(z)}\right] &= \zeta\end{aligned}$$

This shows that the eigen values of the operator S_1 are given by the Fourier transform of its kernel (the Green's function). Actually, this reasoning can be generalized to integral operators defined with a kernel. We will apply it to the remaining operators in the following of the discussion.

Reminding that the Green's function $G_1(r,r') = \frac{1}{||z-z'||}$ is not integrable, we will not be able to perform the testing of the equation of the self terms in the usual manner, see also remark 5.1. In [33], this testing is performed in the centre of the wire. In this situation, the kernel of the operators is given by

$$G_{r1} = \frac{1}{\sqrt{(z-z')^2 + a^2}} \tag{5.19}$$

To obtain this, it is sufficient to replace in (5.11) the observation point $\mathbf{r} = (\rho, \theta, z)$ with $(0, \theta, z)$ while the source point, (where the currents are), lies on the surface of the wire, i.e $\mathbf{r}' = (a, \theta', z')$. The Fourier transform of (5.19) is given by

$$\mathcal{F}\left[G_{r1}(z)\right] = 2K_0\left(2a\xi\right) \tag{5.20}$$

where K_0 denotes the modified Bessel function of second kind of zero order. The spectral index $1/h$ is equivalent to the Fourier variable ξ and we are interested in the behaviour when $h \to 0$ i.e when $\xi \to \infty$. The asymptotic expansion of K_0 gives [2]

$$K_0\left(2a\xi\right) \sim \sqrt{\frac{\pi}{4a\xi}} e^{-2a\xi} \left(1 + \frac{-1}{16a\xi} + \frac{9}{2!(16a\xi)^2} + \frac{-225}{3!(16a\xi)^3} + \cdots\right) \tag{5.21}$$

If $a \ll \xi$, when $\xi \to \infty$, $K_0(2a^2\xi)$ goes exponentially to 0. As a consequence, S_1 is compact operator. If $a \propto h = \frac{1}{\xi}$, $K_0\left(2a\xi\right)$ is constant for all ξ, that is independent of the mesh refinement parameter. In this condition, we expect $\mathcal{S}$ to be an identity.

We have $\mathcal{N} = \nabla\nabla\cdot\mathcal{S}$. Let's decompose it as we did for $\mathcal{S}$,

$$\begin{aligned}
&\mathcal{N} = \nabla\nabla\cdot\mathcal{S} \\
\Leftrightarrow\ &\mathcal{N}(f(r)) = \nabla\nabla\cdot\int_\Gamma G(r,r')f(r')dr' \\
&= \nabla\nabla\cdot\frac{1}{4\pi}\int_\Gamma \frac{1}{R(r,r')}f(r')dr' + \nabla\nabla\cdot\frac{1}{4\pi}\int_\Gamma \frac{e^{-jkR(r,r)}-1}{R(r,r')}f(r')dr'
\end{aligned} \tag{5.22}$$

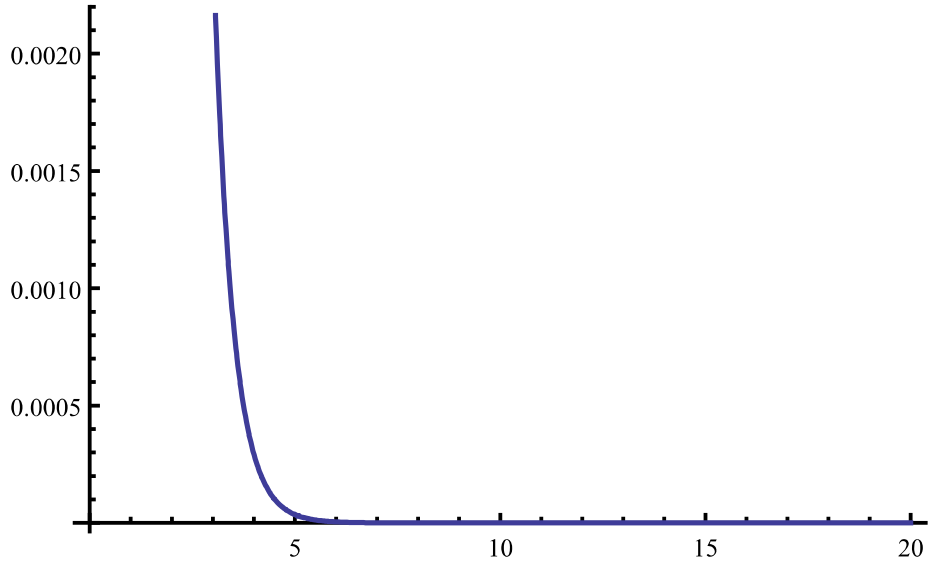

Figure 5.3: Graph of the modified Bessel Function of second kind of order zero, K_0

The same reasoning as in (5.18) holds for the second term of the right hand side in the above equation, since there is no singularity, it is compact. Denote with N_1 the singular part of $\mathcal{N}$, $N_1 f(r) = \nabla\nabla \cdot \int_\Gamma G(r, r')f(r')dr'$. Therefore, on the considered infinite wire, the Fourier transform of the kernel of N_1 is given by $\xi^2 \mathcal{F}[G_{r1}(z)]$, When $\xi \to \infty$,

$$\xi^2 K_0(2a\xi) \sim \xi^2 \sqrt{\frac{\pi}{4a\xi}} e^{-2a\xi} \left(1 + \frac{-1}{16a\xi} + \frac{9}{2!(16a\xi)^2} + \frac{-225}{3!(16a\xi)^3} + \cdots\right) \tag{5.23}$$

which means that if $a \propto h$, $\xi^2 \mathcal{F}[G_{r1}(z)] \approx \xi^2$. It follows that the maximum eigen value of $\mathcal{N}$ will increase proportionally to $1/h^2$. This means that $\mathcal{N}$ will be an operator of order $+2$, in other words, equivalent to a Laplacian.

We now repeat the previous reasoning with the full kernel

$$K(\mathbf{r} - \mathbf{r}') = \frac{1}{2\pi} \int_0^{2\pi} \frac{e^{-jkR(\mathbf{r}-\mathbf{r})}}{R(\mathbf{r} - \mathbf{r}')} d\theta. \tag{5.24}$$

It has been established that the singularity of this kernel is a logarithmic one [16], [53]. On the infinite wire this gives

$$K(z) = K_1(z) - \log(|z|) \frac{1}{\pi a}. \tag{5.25}$$

Where K_1 is a continuous function with bounded derivatives. In this situation, $\mathcal{S}$ becomes

$$\begin{aligned}\mathcal{S}f(z) &= \int_\Gamma (K_1(z-z') - \log(|z-z'|)\frac{1}{\pi a} f(z')dz' \\ &= \int_\Gamma K_1(z-z')f(z')dz' - \int_\Gamma \log(|z-z'|)\frac{1}{\pi a} f(z')dz'\end{aligned} \tag{5.26}$$

Where the first term on the left is compact. We then just need to study $\int_\Gamma \log(|z-z'|)\frac{1}{\pi a} f(z')dz'$. Given that $\mathcal{F}[\log(|z|)] = -2\pi\gamma_e\delta\xi - \frac{\pi}{|\xi|}$, [100, 2.5], we get that the Fourier transform of the kernel of the singular part of $\mathcal{S}$ is proportional to

$$\frac{1}{|\xi|a} \tag{5.27}$$

which means that $\mathcal{S}$ is in the general case an operator of order -1. Multiplying by ξ^2, we deduce that $\mathcal{N}$ is an operator of order $+1$. However, if a is in the order of h then $\mathcal{S}$ will be equivalent to an identity while $\mathcal{N}$ will be equivalent to an operator of order $+2$.

Summarizing, using the reduced kernel, on an infinite wire, assuming that $a \propto h$, S maps from $H^{-1/2}(\Gamma)$ to $H^{-1/2}(\Gamma)$ and $N : H^{1/2}(\Gamma) \to H^{-3/2}(\Gamma)$. Observing that the singularity appearing at the extremities of the wire are not present if the wire is infinite, or that we can pull-back the real axis to a loop, this result can be extended to closed structures. If Γ is open, the Sobolev spaces to consider are slightly different. Indeed, the boundary condition (5.16) that enforces the current to vanish at the extremities of the wire make that the domain of $\mathcal{T}$ must be $\widetilde{H}^{1/2}(\Gamma)$ which is the space of distributions whose extension by zeros over a closed domain belongs to $H^{1/2}$. Formally, for all Sobolev space of fractional order s,

$$\widetilde{H}^s(\mathcal{O}) = \{f \in H^s(\mathbb{R}) : supp f \subseteq \bar{\mathcal{O}}\}$$

where $\bar{\mathcal{O}}$ denotes the closure of the set $\mathcal{O}$. We also have the following duality relations

$$\begin{aligned}\widetilde{H}^s(\mathcal{O})' &= H^{-s}(\mathcal{O}) \\ H^s(\mathcal{O})' &= \widetilde{H}^{-s}(\mathcal{O})'\end{aligned} \tag{5.28}$$

Note that in case of closed domains, $\widetilde{H}^{\pm s}(\mathcal{O}) = H^{\pm s}(\mathcal{O})$.

5.2.1 Discretization of the EFIE

To solve (5.9) numerically using the boundary element method (as described in [33]), we discretize Γ into N_s segments $\{s_k\}_{k=1}^{N_s}$ and N_v vertices $\{v_k\}_{k=1}^{N_v}$. We use as basis and testing functions oriented hat basis functions $\Lambda_h = \{\boldsymbol{\lambda_k}(r)\}$ whose support μ_k are the segments $s_k = (v_k, v_{k+1})$ and $s_{k+1} = (v_{k+1}, v_{k+2})$ defined by

$$\boldsymbol{\lambda_k}(r) = \begin{cases} \dfrac{z_k(r)}{l_k}\hat{\boldsymbol{t}}(r) & \text{if } r \in s_k \\ \dfrac{1 - z_{k+1}(r)}{l_{k+1}}\hat{\boldsymbol{t}}(r) & \text{if } r \in s_{k+1} \\ 0 & \text{elsewhere} \end{cases} \tag{5.29}$$

with $z_k(r) = ||r - v_k||$, the distance to the first extremity of the segment, and $l_k = ||v_{k+1} - v_k||$, the length of the segment s_k. We use uniform meshes, so that $l_k = h$, the mesh parameter, for all k. The boundary condition that states that there is no current flowing outside the wire at the extremities is enforced by placing no basis function on those points. Figure 5.4 presents the geometric definitions and the hat basis functions.

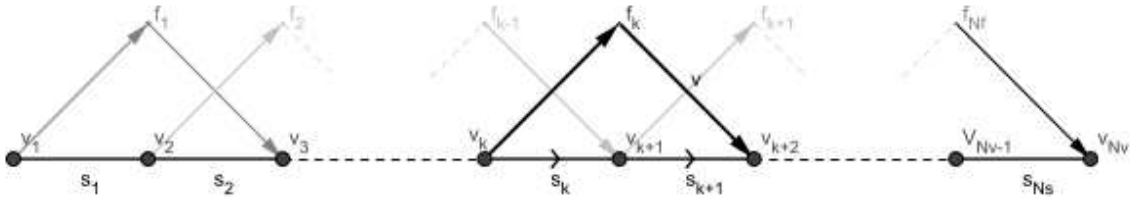

Figure 5.4: Hat functions $\boldsymbol{\lambda_k}$ used to discretize the unknown and to test the wire EFIE

We define the duality product as $< f|g >= \int_\Gamma f(r) \cdot g(r) dr$. Testing and expanding the unknown with the hat functions, the EFIE equation becomes

$$\mathbf{Zx} = \mathbf{b} \tag{5.30}$$

with $\mathbf{Z}$ the impedance matrix whose entries are given by [33]

$$\mathbf{Z}_{mn} = \int_{\mu_m} \boldsymbol{\lambda_m}(r) \cdot \left\{ \left[-j\omega\mu - \frac{j}{\omega\mu\epsilon} \nabla\nabla\cdot \right] \int_{\mu_n} K(r, r') \frac{\boldsymbol{\lambda_n}(r')}{4\pi} dr' \right\} dr \tag{5.31}$$

$$\mathbf{Z}_{mn} = Z_A + Z_\Phi \tag{5.32}$$

where

$$Z_A = j\omega\mu \int_{\mu_m} \boldsymbol{\lambda_m}(r) \cdot \int_{\mu_n} K(r,r') \frac{\boldsymbol{\lambda_n}(r')}{4\pi} dr'dr \tag{5.33}$$

and

$$Z_\Phi = -\frac{j}{\omega\mu\epsilon} \int_{\mu_m} \boldsymbol{\lambda_m}(r) \cdot \nabla\nabla \cdot \int_{\mu_n} K(r,r') \frac{\boldsymbol{\lambda_n}(r')}{4\pi} dr'dr.$$

Using integration by part and the fact that the function λ_k vanishes at the extremities of the segment,

$$Z_\Phi = \frac{j}{\omega\mu\epsilon} \int_{\mu_m} \nabla \cdot \boldsymbol{\lambda_m}(r) \nabla \cdot \int_{\mu_n} K(r,r') \frac{\boldsymbol{\lambda_n}(r')}{4\pi} dr'dr$$

The divergence can be put inside the integrand leading

$$Z_\Phi = -\frac{j}{\omega\mu\epsilon} \int_{\mu_m} \nabla \cdot \boldsymbol{\lambda_m}(r) \int_{\mu_n} \nabla \cdot (K(r,r') \frac{\boldsymbol{\lambda_n}(r')}{4\pi}) dr'dr$$

$$\Leftrightarrow Z_\Phi = -\frac{j}{\omega\mu\epsilon} \int_{\mu_m} \nabla \cdot \boldsymbol{\lambda_m}(r) \int_{\mu_n} K(r,r') \frac{\nabla' \boldsymbol{\lambda_n}(r')}{4\pi} dr'dr. \tag{5.34}$$

In the presented numerical result, we used the reduced kernel (5.13). The singularity extraction is carried out as in [33]. For the self terms in Z_A and Z_ϕ, the testing is done in the center of the wire. In this situation, $||r - r'|| = \sqrt{(t-t')^2 + a^2}$ and semi-analytical integration can be done. We always assume that $a << h$, (we fixed $a = 10^{-4} h_{min}$, were h_{min} is the smallest mesh parameter of all the numerical experiments). Elsewhere, the integration is performed using Gaussian quadrature. The right hand side of (5.30) is given by

$$\mathbf{b} = \int_{\mu_m} \boldsymbol{\lambda_m}(r) \cdot \boldsymbol{E}^i(r) dr \tag{5.35}$$

and $\mathbf{x}$ is the unknown vector that contains the expansion coefficients of $I(r')\hat{\boldsymbol{t}}$ in terms of hat functions. Future investigations should include numerical results on the full kernel to check the theoretical developments and draw conclusions.

5.2.2 Numerical Results

A first test was performed to check that our implementation of the EFIE is correct in the case of a thin straight dipole; since in this case the analytical solution is known [10]. The impinging field has a frequency of $70.5MHz$. The radius of the wire is set to $1\times10^{-4}m$ and its length is $2\,m$. The current obtained using numerical and analytical approach are shown in Figure 5.5. It can be seen that our solution matches the analytical solution. The relative error between the computed currents and the theoretical currents is 3%. A similar test was done in the case of a loop antenna and we obtained a relative error of 0.1% with respect to the analytical solution in computing the radiated far field whose radiation pattern in shown Figure 5.6. We also checked that the relative error for both situations was decreasing when refining the mesh.

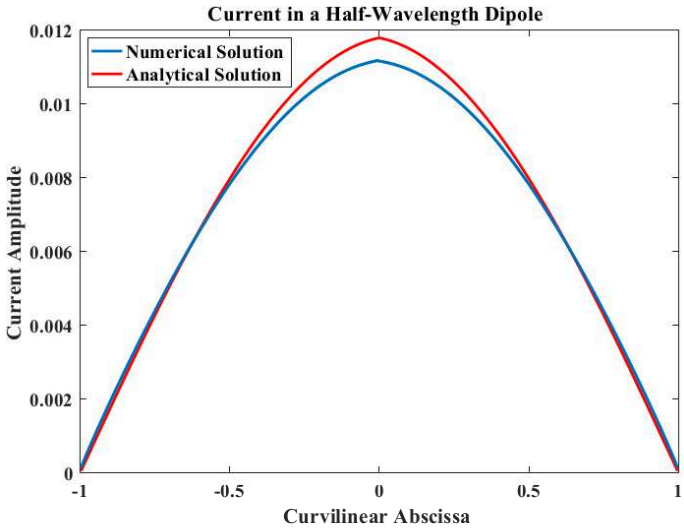

Figure 5.5: Simulated current and reference solution on a half-wavelength dipole antenna.

To confirm the results of the previous section, the condition number of the EFIE operator $\mathcal{T}$ as well as the condition number of $\mathcal{S}$ and $\mathcal{N}$, respectively denoted with κ_{EFIE}, $\kappa_{\mathcal{S}}$ an $\kappa_{\mathcal{N}}$ are studied in the case of the two previous geometries. We see, as expected, in Figure 5.7 that the condition number of $\mathcal{T}$ and $\mathcal{N}$ is increasing as well as the condition number of $\mathcal{S}$ is the case of the straight wire. Both in the case of the straight wire and

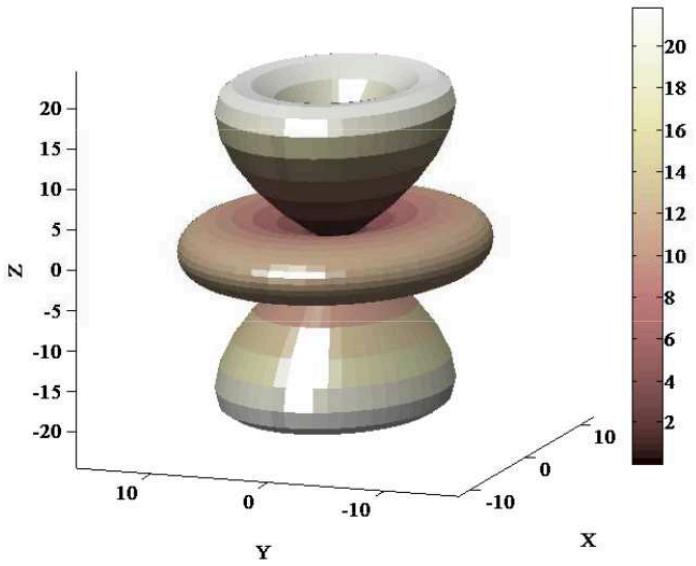

Figure 5.6: Radiation pattern of the loop antenna.

the loop, the condition numbers of the EFIE operator and of $\mathcal{N}$ grow like $1/h^2$. This is checked figure 5.8 where we plot the square root of the curves of Figure 5.7 have been rectified. However, the condition number of the $\mathcal{S}$ behaves differently in the case of the loop and the straight wire. For the loop it seems to be an identity (its condition number is stable with the mesh refinement) while in the case of the straight wire, the condition number increases with the mesh refinement. When studying the behavior of its minimum and maximum eigen value, Figure 5.10, we see that its maximum singular values is stable with the mesh refinement while its minimum singular value decreases exponentially. This behavior is typical for compact operator, as expected. In the same fashion, the study of the singular values of the operator $\mathcal{N}$ is conformed to what is expected: the maximum value of $\mathcal{N}$ grows like $1/h^2$ while its minimum is stable as can be seen Figure 5.9.

5.3 Proposed Calderon Preconditioner

In this section, we propose a Calderon preconditioner for the EFIE operator in the case of thin wires. The Calderon preconditioner is built by seeking to construct an operator

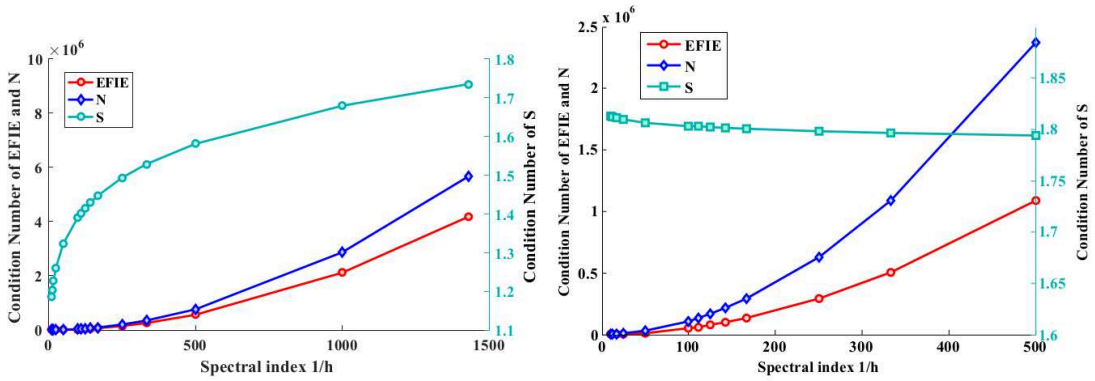

(a) (b)

Figure 5.7: Condition Number of $\mathcal{T}$, $\mathcal{S}$ and $\mathcal{N}$ versus the spectral index $1/h$ for a straight antenna (a) and a loop antenna (b).

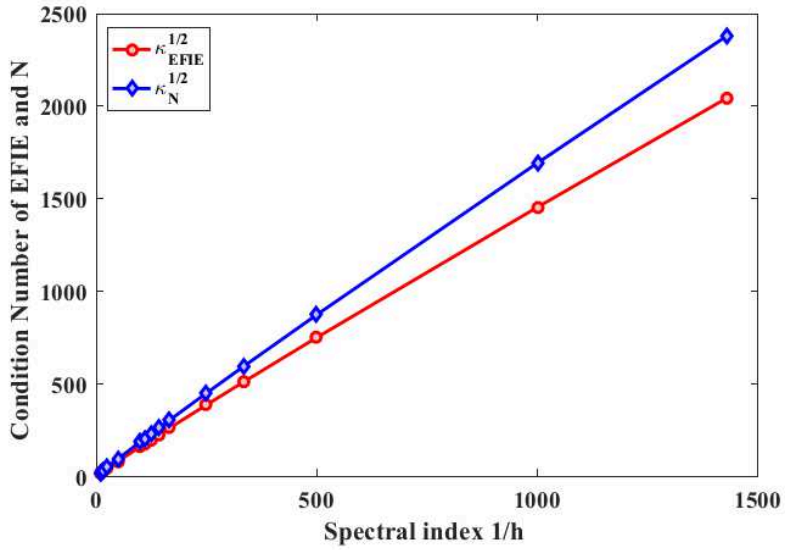

Figure 5.8: Condition Number of $\mathcal{T}$, $\mathcal{S}$ and $\mathcal{N}$ versus the spectral index $1/h$ for a straight antenna.

spectrally equivalent to an identity, as explained in Chapter 4. We show that the presented strategy allows to have a condition number that grows only with $\log(h)$ instead of h^2 in the case of open strutures. Numerical results corroborate the theoretical developments.

5.3.1 Theoretical Developments

Recall from section 5.2 that the condition number of $\mathcal{T}$ is controlled by the condition number of $\mathcal{N}$. As a consequence, we seek to build an operator spectrally equivalent to the

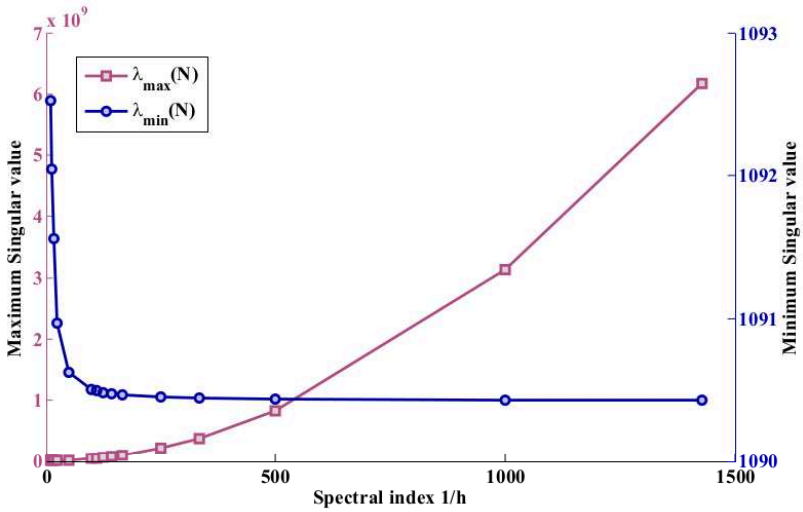

Figure 5.9: Maximum and minimum singular values of $\mathcal{N}$ with respect to the spectral index $1/h$ for a straight antenna.

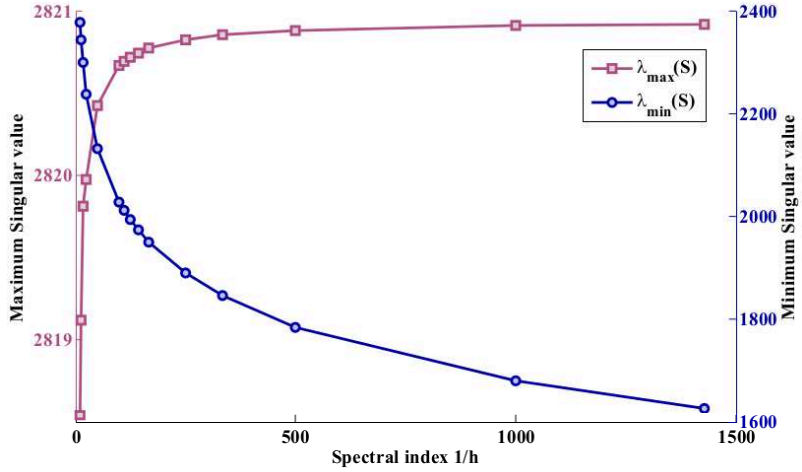

Figure 5.10: Maximum and minimum singular values of $\mathcal{S}$ with respect to the spectral index $1/h$ for a straight antenna.

inverse of $\mathcal{N}$. Such an inverse will be of order -2. Lets call $\mathcal{N}^{-1}$ this operator. Applying it to the EFIE operator (without taking into account the factors showing the dependency to the frequency), we obtain

$$\mathcal{N}^{-1}\mathcal{T} = \mathcal{N}^{-1}\mathcal{S} + \mathcal{N}^{-1}\mathcal{N}$$

$$\Leftrightarrow \mathcal{N}^{-1}\mathcal{T} = \mathcal{N}^{-1}\mathcal{S} + \mathcal{I}.$$

Since $\mathcal{S}$ is of order 0, $\mathcal{N}^{-1}\mathcal{S}$ will be of order -2. It is then a smoothing operator and is therefore compact. It follows that both $\mathcal{N}^{-1}\mathcal{S}$ and $\mathcal{I}$ have a bounded maximum singular

values. Since the singular values of a compact operator accumulate at zero, both the maximum and minimum singular value of $\mathcal{N}^{-1}\mathcal{T}$ will be bounded. As a consequence, $\mathcal{N}^{-1}\mathcal{T}$ is well conditioned.

In two dimensions, the usual operators we deal with are [51]

$$\mathcal{V}f(r) = -\int_\Gamma \log(|r-r'|)f(r')dr', \quad \mathcal{V} : \widetilde{H}^{-1/2}(\Gamma) \to H^{1/2}(\Gamma) \tag{5.36}$$

and

$$\mathcal{W}f(r) = \frac{d}{dr}\int_\Gamma \log(|r-r'|)\frac{d}{dr'}f(r')dr', \quad \mathcal{W} : \widetilde{H}^{1/2}(\Gamma) \to H^{-1/2}(\Gamma) \tag{5.37}$$

We have the following norm equivalence [63]

$$< u, \mathcal{V}u >= ||f||_{\widetilde{H}^{-1/2}}(\Gamma) \quad \forall u \in \widetilde{H}^{-1/2} \tag{5.38}$$

$$< v, \mathcal{W}v >= ||f||_{\widetilde{H}^{1/2}}(\Gamma) \quad \forall v \in \widetilde{H}^{1/2} \tag{5.39}$$

We can show that

$$< x, \nabla\nabla\cdot x >=< \nabla\cdot x, \nabla\cdot x >= ||x||_{\widetilde{H}^1(\Gamma)}$$

and as a consequence of (5.39)

$$< x, \mathcal{W}^2 x >= ||x||_{\widetilde{H}^1(\Gamma)}. \tag{5.40}$$

Therefore, $\mathcal{W}^2$ is equivalent to $\mathcal{N}$ and $\sqrt{\mathcal{N}} = \mathcal{W}$. (This can also easily be seen by looking at the symbol of the operators : the symbol of $\mathcal{N}$ is $\sigma_{\mathcal{N}} = \xi^2$ and the symbol of W is $\sigma_{\mathcal{W}} = \xi$ therefore $\sigma_{\mathcal{W}^2} = \xi^2 = \sigma_{\mathcal{N}}$). The equivalence $\sqrt{\mathcal{N}} = \mathcal{W}$ means that an efficient preconditioner for $\mathcal{T}$ can be obtained by building the inverse of $\mathcal{W}$.

Let's first consider the case of closed curves. If Γ is closed, $\mathcal{T} : H^{1/2}(\Gamma) \to H^{-3/2}(\Gamma)$, $\mathcal{W} : H^{1/2}(\Gamma) \to H^{-1/2}(\Gamma)$ and $\mathcal{V} : H^{-1/2}(\Gamma) \to H^{1/2}(\Gamma)$. In this case, we have the standard Calderon identities [95]

$$\mathcal{V}\mathcal{W} = \frac{1}{4}I_{H^{1/2}(\Gamma)} - K_D^2 \tag{5.41}$$

$$\mathcal{W}\mathcal{V} = \frac{1}{4} I_{H^{-1/2}(\Gamma)} - K_D'^2 \tag{5.42}$$

with K_D and K_D' the double layer and adjoint double layer operators in 2D which are compact. The two equations (5.41) and (5.42) mean that $\mathcal{V}$ is a good preconditioner for $\mathcal{W}$ and vice versa. In particular, $\mathcal{V}\mathcal{N}\mathcal{V} \asymp \mathcal{V}\mathcal{W}^2\mathcal{V} \asymp \mathcal{I}_{H^{1/2}(\Gamma)}$ and

$$\mathcal{V}\mathcal{T}\mathcal{V} \asymp \mathcal{K} + \mathcal{I}_{H^{1/2}(\Gamma)} \tag{5.43}$$

where $\mathcal{K} = \mathcal{V}\mathcal{S}\mathcal{V}$ is a smoothing operator of order -2, compact. Therefore $\mathcal{V}\mathcal{T}\mathcal{V}$ is a well conditioned operator.

In the case of open curves, the duality relation between the Sobolev spaces degenerates into (5.28), that depends on the extensibility of the considered Sobolev spaces by zero. As a consequence, the identities (5.41) and (5.42) do not hold and the operator spectrally equivalent to the inverse of $\mathcal{W}$ is not given by $\mathcal{V}$ anymore. Preconditioning $\mathcal{W}$ with $\mathcal{V}$ in this case leads to a condition number that still grows with $\log(1/h)$ [63], and would not work for preconditioning $\mathcal{T}$. In this situation, boundary effects must be taken into account, as those operators present a singularity in $1/\sqrt{d}$, where d is the distance to the end point of the curve [65]. Rokhlin in [52] proposed a numerical algorithm to build the inverse of $\mathcal{W}$ and $\mathcal{V}$. It is only recently that [51] introduced explicit inverse of $\mathcal{W}$ and $\mathcal{V}$ of for open curves. On $\Gamma_0 = (-1, 1) \in \mathbb{R}$, they introduced the following modified operators

$$\widetilde{V} f(r) = \int_{\Gamma_0} \log(\frac{M(r,r')}{||r-r'||}) f(r') dr', \quad \widetilde{V} : H^{-1/2}(\Gamma_0) \to \widetilde{H}^{1/2}(\Gamma_0) \tag{5.44}$$

and

$$\widetilde{\mathcal{W}} f(r) = -\frac{d}{dr} \int_{\Gamma_0} \log(\frac{M(r,r')}{||r-r'||}) \frac{d}{dr'} f(r') dr', \quad \widetilde{\mathcal{W}} : H^{1/2}(\Gamma_0) \to \widetilde{H}^{-1/2}(\Gamma_0). \tag{5.45}$$

with

$$M(x,y) = \frac{1}{2}\left((x-y)^2 + (\sqrt{1-x^2} + \sqrt{1-y^2})^2\right) \tag{5.46}$$

They derived the following Calderon identities

$$\widetilde{\mathcal{V}}\mathcal{W} = \mathcal{I}_{\widetilde{H}^{1/2}(\Gamma_0)} \tag{5.47a}$$

$$\widetilde{\mathcal{W}}\mathcal{V} = \mathcal{I}_{\widetilde{H}^{-1/2}(\Gamma_0)} \tag{5.47b}$$

$$\mathcal{V}\widetilde{\mathcal{W}} = \mathcal{I}_{H^{1/2}(\Gamma_0)} \tag{5.47c}$$

$$\mathcal{W}\widetilde{\mathcal{V}} = \mathcal{I}_{H^{-1/2}(\Gamma_0)} \tag{5.47d}$$

Confirming their results, [48] showed that these identities can be extended to a general curve Γ and can be used for preconditioning $\mathcal{W}$, $\widetilde{\mathcal{W}}$, $\mathcal{V}$ or $\widetilde{\mathcal{V}}$ on a general curve. Slightly abusing, we keep the same notation for all the operators defined on Γ_0 and Γ. The latter can be obtained using appropriate parametrization and lifting from Γ_0 to Γ.

We showed, (5.40) that if we can precondition $\mathcal{W}$ then we can precondition $\mathcal{T}$ in a close curve. If we do the same in an open curve, using the modified single layer operator, $\widetilde{\mathcal{V}}$ we obtain:

$$\widetilde{\mathcal{V}}\mathcal{T}\widetilde{\mathcal{V}} = \widetilde{\mathcal{V}}\mathcal{S}\widetilde{\mathcal{V}} + \widetilde{\mathcal{V}}\mathcal{N}\widetilde{\mathcal{V}}. \tag{5.48}$$

While $\widetilde{\mathcal{V}}\mathcal{S}\widetilde{\mathcal{V}}$ is still a smooth operator, we have:

$$H^{1/2}(\Gamma) \xrightarrow{\widetilde{\mathcal{V}}} \widetilde{H}^{3/2}(\Gamma) \xrightarrow{\mathcal{N}} H^{-1/2}(\Gamma) \xrightarrow{\widetilde{\mathcal{V}}} \widetilde{H}^{1/2}(\Gamma) \tag{5.49}$$

and we actually do not end-up with an identity, indeed, $\widetilde{H}^{1/2}(\Gamma)$ is a proper subspace of $H^{1/2}(\Gamma)$ [63]. In the same paper, the authors show that it is the difference between the $\widetilde{H}^{1/2}(\Gamma)$ and $H^{1/2}(\Gamma)$ that prevents to build a stable system matrix when preconditioning on an open curve $\mathcal{W}$ with $\mathcal{V}$. The same situation is obtained here when preconditioning $\mathcal{T}$ with $\widetilde{\mathcal{V}}$ and thus we can expect the same result : the proposed preconditioner should provide a system matrix whose condition number grows with $\log(1/h)$. Numerical experiments confirm this result. On-going work seeks to rigorously proof it.

5.3.2 Discretization of the Preconditioning Operators

As explained in Chapter 4, paragraph 4.1.3, the discretization of the operators is also an important step in preconditioning. We recall that the pairing between the basis used to discretize the preconditioned operator and the preconditioner must be stable. In our case, denoting with $\Phi_h = \{\phi_i\}$ the set of basis functions used to discretize $\mathcal{V}$ and $\widetilde{\mathcal{V}}$ and $\Lambda_h = \{\lambda_i\}$ the set of basis functions used to discretize $\mathcal{T}$ (as in paragraph 5.2.1) we must have:

$$\sup_{\phi_k \in \Phi_h} \frac{| < \phi_k, f_k > |}{||\lambda_k||} \geqslant c_M ||\lambda_k|| \quad \forall \lambda_k \in \Lambda_h \tag{5.50}$$

(and, of course, $\dim(\Phi_h) = \dim(\Lambda_h)$). Since we want to discretize $\widetilde{\mathcal{V}} : H^{-1/2}(\Gamma) \rightarrow \widetilde{H}^{-1/2}(\Gamma)$, $\Phi_h \subset H^{-1/2}(\Gamma)$. We select Φ_h to be the set of (one-dimensional) dual patch basis functions, indeed, [48] showed that this choice of functions provides a stable pairing with Λ_h. Denote with ν_i the mid-point of the segment s_i,

$$\{s_i'\} = \left\{ \begin{array}{ll} [\nu_i \nu_{i+1}] & \text{if } i \neq 1, N_s - 1 \\ [v_1 \nu_2] & \text{if } i = 1 \\ [\nu_{N_s - 1} v_{N_v}] & \text{if } i = N_s - 1 \end{array} \right\}$$

are the dual cell. Then the dual patch basis functions are defined as

$$\phi_i(r) = \left\{ \begin{array}{l} 1 \text{ if } r \in s_i' \\ 0 \text{ elsewhere} \end{array} \right.$$

. The dual mesh and the dual patches basis functions are shown in Figure5.11.

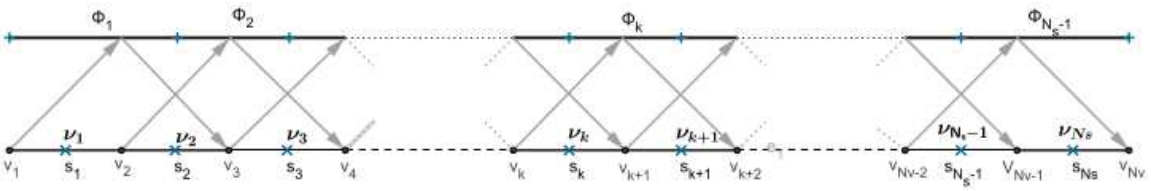

Figure 5.11: Dual mesh and dual patch basis functions ϕ_k used to discretize $\widetilde{\mathcal{V}}$ and $\mathcal{V}$. Hat functions λ_k are shown in grey.

The stiffness matrix associated to $\mathcal{V}$ and $\widetilde{\mathcal{V}}$ are then respectively $\mathbf{V}$ and $\widetilde{\mathbf{V}}$ such that

$$\mathbf{V}_{ij} = \langle \mathcal{V}\phi_i, \phi_j \rangle \tag{5.51}$$

and

$$\widetilde{\mathbf{V}}_{ij} = \langle \widetilde{\mathcal{V}} \phi_i, \phi_j \rangle. \tag{5.52}$$

We denote with $\mathbf{G}$ the Gram matrix that links the two discrete basis F_h and Φ_k. Its entries are given by

$$\mathbf{G}_{ij} = \langle \phi_i, \lambda_j \rangle \tag{5.53}$$

Then, in case of closed curves, the Calderon preconditioned system read

$$\mathbf{V}\mathbf{G}^{-1}\mathbf{Z}\mathbf{G}^{-1}\mathbf{V}\mathbf{y} = \mathbf{V}\mathbf{G}^{-1}\mathbf{b} \tag{5.54}$$

and the unknown $\mathbf{x}$ is given by

$$\mathbf{x} = \mathbf{G}^{-1}\mathbf{V}\mathbf{y} \tag{5.55}$$

In the following, we denote with $\mathbf{Z_c}$ the preconditioned system matrix, $\mathbf{Z_c} = \mathbf{V}\mathbf{G}^{-1}\mathbf{Z}\mathbf{G}^{-1}\mathbf{V}$.

5.3.3 Numerical Results

We present several experiments that show the performances of the proposed Calderon preconditioner. In particular, we study the spectrum and the condition number of the preconditioned system matrix $\mathbf{Z_c}$ for both open and close wire.The frequency is set to 125 MHz and the mesh parameter h varies from 0.1 to 7.10^{-4} m.

In the case of a single loop, Figure 5.12 shows that the proposed Calderon preconditioner, $(\mathbf{V}\mathbf{G}^{-1})$ achieves a stable condition number as expected by the theory. In the case of an open curve, Figure 5.13 shows that preconditioning the EFIE matrix with the standard operator $\mathcal{V}$ is inefficient whereas the condition number of the EFIE matrix the provided by the proposed Calderon preconditioner (using $\widetilde{\mathcal{V}}$) is nearly stable with the mesh refinement parameter. It provides a condition number that grows with $\log(1/h)$, as can be seen in Figure 5.13b, where the scale has been changed to a linear scale and the curve rectified.This result is in accordance with the previous discussion. Indeed, the proposed preconditioner

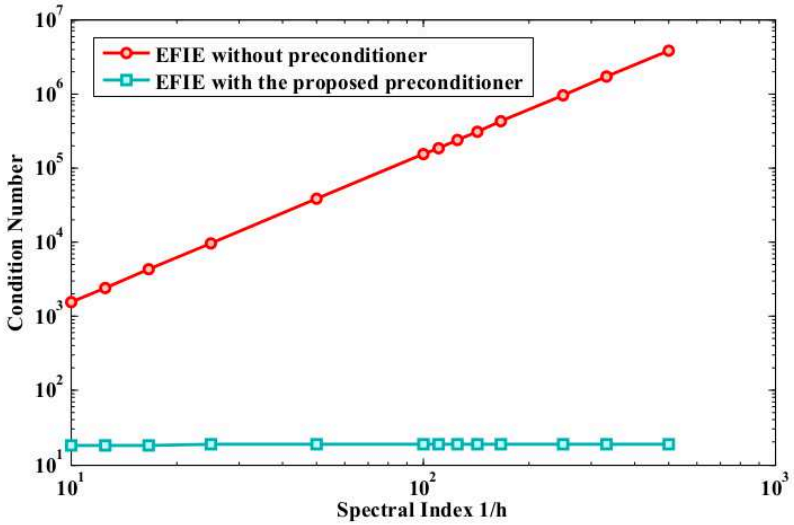

Figure 5.12: Condition Number of the EFIE matrix $\mathbf{Z}$ and of the EFIE matrix preconditioned with $\mathbf{V}$ when the geometry is a loop, it can be observed that the condition number of the preconditioned matrix is independent of the spectral index parameter $1/h$.

can only limit the growth of the maximum value to $O(log(1/h))$ while the minimum singular value remains constant with h. This two properties are verified in Figure 5.14, where the maximum and minimum singular values are plotted for different values of the mesh parameter h.

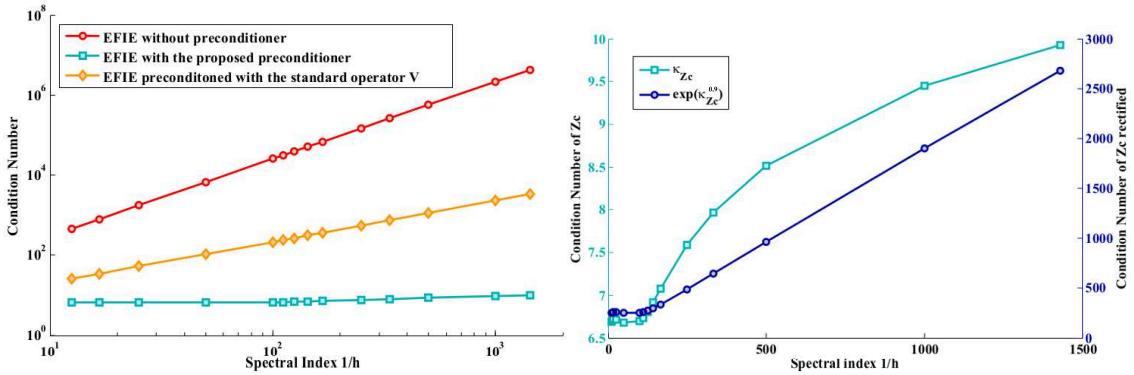

(a) (b)

Figure 5.13: Condition Number of the EFIE matrix $\mathbf{Z}$ and of the EFIE matrix preconditioned with $\widetilde{\mathbf{V}}$ and $\mathbf{V}$ for a straight antenna (a). Figure (b) displays the condition number κ_{Z_c} of the EFIE matrix preconditioned with $\widetilde{\mathbf{V}}$ in linear scale. It can be seen that the preconditioner is not optimal but limits the growth of the condition number to a logarithmic one.

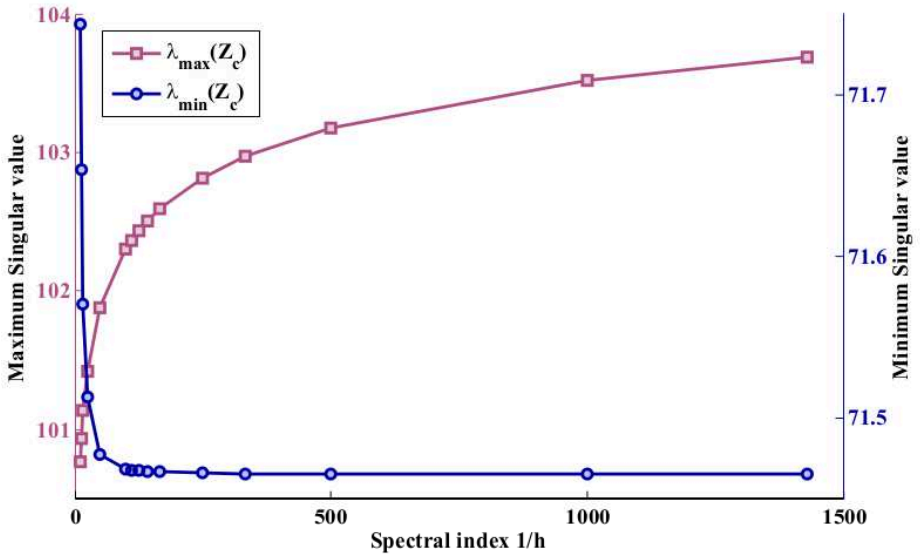

Figure 5.14: Maximum and minimum singular values of the preconditioned system with respect to the spectral index .

5.4 A New Integral Equation for the EEG Forward Problem that Models the White Matter fibers

Starting from the idea that for cylindrical and thin structure, the 3D geometry can be simplified in a one-dimensional curve, we developed a new integral formulation for the EEG forward problem. Indeed, several studies showed the influence of the anisotropic properties of the brain while performing source imaging due to the presence of fibers in the white matter [11], [41], [42], [102], [104]. The anisotropic conductivity tensor can be derived from the diffusion tensor MRI data (see for example [58] and references therein). Indeed it has been shown [98] that the water diffusion tensor is linearly linked to the conductivity tensor. Therefore, for each voxel of the magnetic resonance image, it is possible to estimate the conductivity tensor. This information can be directly used in finite element methods to compute the solution to the EEG forward problem. The information on the water diffusion tensor can also be exploited to obtain the white matter fiber geometry through a tractography process [66]. This results in a set of one dimensional curves that represent the white matter fibers. This treatment is expected to lower the computational burden since only the

layer surrounding the fiber and the fibers themselves have to be discretized. We assume that the head media is represented with only one layer denoted Ω and contains N_f fibers f. The boundary of the domain Ω is denoted with $\partial\Omega$ and its normal n is pointing outwards. The isotropic conductivity of this layer is denoted σ_b while the anisotropic conductivity of the fibers is denoted by $\bar{\bar{\sigma}}_f$.

We start from the EEG forward problem that reads

$$\nabla \cdot \bar{\bar{\sigma}} \nabla V = \nabla \cdot J \tag{5.56}$$

where, as usual, V is the unknown potential, J are the source currents and $\bar{\bar{\sigma}}$ the conductivity tensor.

Add and remove $c\Delta V$ to (5.56), with $c \in \mathbb{R}$,

$$\nabla \cdot \bar{\bar{\sigma}} \nabla V + c\nabla \cdot \nabla V - c\nabla \cdot \nabla V = \nabla \cdot J \tag{5.57a}$$

$$\nabla \cdot \left(\bar{\bar{\sigma}} - cI\right) \nabla V + c\nabla \cdot \nabla V = \nabla \cdot J \tag{5.57b}$$

$$c\Delta V = \nabla \cdot J - \nabla \cdot \left(\bar{\bar{\sigma}} - cI\right) \nabla V \tag{5.57c}$$

$$c\Delta V = -\nabla \cdot \left[\left(\bar{\bar{\sigma}} - cI\right) \nabla V - J\right] \tag{5.57d}$$

$$\Delta V = -\nabla \cdot \left[\frac{\bar{\bar{\sigma}} - cI}{c} \nabla V - \frac{1}{c} J\right] \tag{5.57e}$$

The equation (5.57e) is the Poisson's equation with a source term equal to $-f = -\nabla \cdot \left[\left(\bar{\bar{\sigma}} - cI\right) \nabla V - J\right] / c$. Its solution is given by the representation theorem [70]

$$V(r) = \int_{\partial\Omega} G(r, r') \partial'_n V(r') dr' - \int_{\partial\Omega} \partial'_n G(r, r') V(r') dr' + \int_{\Omega} G(r, r') f(r') dr' \tag{5.58}$$

where G is the Green's function associated to the Poisson equation, i.e.

$$G(r, r') = \frac{1}{4\pi} \frac{1}{||r - r'||} \tag{5.59}$$

Taking the trace γ_0^- and given that the conormal derivative of the potential is continuous at the boundary,

$$V(r) - 1/2V(r) = -\int_{\partial\Omega} \partial'_n G(r, r') V(r') dr' + \int_{\Omega} G(r, r') f(r') dr' \quad \forall r \in \partial\Omega \tag{5.60}$$

Replacing f with its expression and introducing $\chi = (\bar{\bar{\sigma}} - cI)\,\bar{\bar{\sigma}}^{-1}$ and $J_v = \bar{\bar{\sigma}}\nabla V$, we have

$$\frac{1}{2}cV(r) = -c\int_{\partial\Omega}\partial'_n G(r,r')V(r')dr' + \int_\Omega G(r,r')\nabla'\cdot\left[\chi J_v(r') - J(r')\right]dr' \quad \forall r \in \partial\Omega$$

$$\Leftrightarrow \frac{1}{2}cV = -c\int_{\partial\Omega}\partial'_n G(r,r')V(r')dr' + \int_\Omega G(r,r')\nabla'\cdot[\chi J_v(r')]\,dr' - \int_\Omega G(r,r')\nabla'\cdot J(r')dr' \tag{5.61}$$

The constant c can be chosen as we want. Let's take $c = \sigma_b$, the conductivity of the medium surrounding the fibers. Then, (5.61) amounts to

$$\frac{1}{2}\sigma_b V = -\sigma_b\int_{\partial\Omega}\partial'_n G(r,r')V(r')dr' + \sum_{i=1}^{N_f}\int_{f_i} G(r,r')\nabla'\cdot[\chi J_v(r')]\,dr' - \int_\Omega G(r,r')\nabla'\cdot J(r')\,dr' \tag{5.62}$$

Since σ_b is isotropic and $\bar{\bar{\sigma_f}}$ is constant along the fiber, we get

$\chi = (\sigma_l - \sigma_b)/\sigma_l I = kI$, where σ_l is the conductivity along the fibers. Then, (5.62) becomes

$$\frac{1}{2}\sigma_b V = -\sigma_b\int_{\partial\Omega}\partial'_n G(r,r')V(r')dr' + \sum_{i=1}^{N_f}\int_{f_i} G(r,r')k\nabla'\cdot J_v(r') - \int_\Omega G(r,r')\nabla'\cdot J(r')dr' \tag{5.63}$$

Taking the gradient of (5.58), we obtain on the fibers, a second equation

$$\begin{aligned} J_v(k-1) = \sigma_b\nabla V = &-\sigma_b\nabla\int_{\partial\Omega}\partial'_n G(r,r')V(r')dr' + \sum_{i=1}^{N_f}\nabla\int_{f_i} G(r,r')k\nabla' J_v(r')dr' \\ &-\nabla\int_\Omega G(r,r')\nabla'\cdot J(r')\,dr' \end{aligned} \tag{5.64}$$

As a consequence, we end-up with two integral equations for the two unknowns V and J_v.

To solve these two equations, we will use the boundary element method.

5.4.1 Discretization of the Equations

The geometry presented here is made of a surface ($\partial\Omega$) and fibers ($\bigcup_{i=1}^{N_f} f_i$), that we model with cylinders as in [74]. The surface is tessellated into N_t triangles $\{t_i\}_{i=1}^{N_t}$ while the fibers are discretized into N_s smaller cylinder $\{c_i\}_{i=1}^{N_s}$. We assume that the fibers are thin enough (their radius is in the order of the micrometer, while their length is overall comprised between 10 cm and some millimetres [72]) so that the current J_v only flows along the fibers' axis. To take into account this supposition, the expansion functions for J_v will be the hat functions Λ_h defined in (5.29). The potential on the surface is discretized with patch basis functions P_1, as defined in chapter 2. We hence have

$$V = \sum_{i=1}^{N_t} \alpha_i P_{1i}$$

and

$$J_v = \sum_{i=1}^{N_t} \beta_i \lambda_i.$$

Equation (5.63) is tested on the surface while (5.64) is tested on the fibers. The system arising is

$$\mathbf{Z}\mathbf{x} = \mathbf{r} \tag{5.65}$$

with

$$\mathbf{x} = \begin{pmatrix} \mathbf{a} \\ \\ \mathbf{b} \end{pmatrix} \text{ where } \begin{cases} [\mathbf{a}]_j = \alpha_j \\ \\ [\mathbf{b}]_j = \beta_j \,, \end{cases}$$

assuming a dipolar source, $\nabla \cdot J = q.\nabla\delta_{r_0}$,

$$\mathbf{r} = \begin{pmatrix} \mathbf{u} \\ \\ \mathbf{v} \end{pmatrix} \text{ where } \begin{cases} [\mathbf{u}]_j = \displaystyle\int_{t_j} P_{1j} q \cdot \nabla G(r_0, r)/\sigma_b \, dr \\ \\ [\mathbf{v}]_j = \displaystyle\int_{c_j} \nabla \cdot \lambda_j q \cdot \nabla G(r_0, r)/\sigma_b \, dr, \end{cases}$$

and

$$\mathbf{Z} = \begin{pmatrix} \mathbf{D} & \mathbf{S_J} \\ \mathbf{N} & \mathbf{D_J^*} \end{pmatrix}$$

where

$$\begin{cases} [\mathbf{D}]_{ij} = \begin{cases} \sigma_b \displaystyle\int_{t_i} P_{1i}(r) \int_{t_j} P_{1j}(r') \partial'_n G(r,r') dr' dr & \text{if } i \neq j \\ \sigma_b \dfrac{1}{2} \displaystyle\int_{t_i} P_{0i}^2(r) dr & \text{if } i = j \end{cases} \\ [\mathbf{N}]_{ij} = \displaystyle\int_{c_i} \frac{d}{dr} \lambda_i(r) \int_{t_j} P_{1j}(r') \partial'_n G(r,r') dr' dr \\ [\mathbf{S_j}]_{ij} = \displaystyle\int_{t_i} P_{1i}(r) \int_{c_j} G(r,r') \chi \lambda_j(r') dr' dr \\ \left[\mathbf{D_j^*}\right]_{ij} = \displaystyle\int_{c_i} \frac{d}{dr} \lambda_i(r') \int_{c_j} G(r,r') \chi \frac{d}{dr'} \lambda_j(r') dr' dr \end{cases}$$

Note that the integral on the small cylinder c_i are volume integrals. They read

$$\int_{c_i} \frac{d}{dr} \lambda_i(r) g(r) dr = \int_{\rho \in [0,a]} \int_{\theta \in [-\pi,\pi]} \int_{s_i} \frac{d}{dr} \lambda_i(z,\theta,\rho) g(z,\theta,\rho) \rho dz d\theta d\rho \tag{5.66}$$

Assuming that the current is not varying along the radius, and the azimuthal direction,

$$\int_{c_i} \frac{d}{dr} \lambda_i(r) g(r) dr = \pi a^2 \int_{s_i} \frac{d}{dr} \lambda_i(z) g(z) dz \tag{5.67}$$

5.4.2 Numerical Results

The reference solution for all the presented numerical experiments is a finite element method computed with a commercial software, on a very refined mesh. It was also checked that in case of isotropic conductivities, the solution provided by the software gives a relative error smaller than 0.01% with respect to the analytical solution of [26].

We first verify that the proposed solution is able to handle the presence of one fiber in the head. The layer representing the head has an isotropic conductivity of 0.33, it is represented by a sphere of radius 1. To emphasize the anisotropic property of the wire, the conductivity along the fiber is set 100 times higher than the conductivity of the media that surrounds it. The fiber is a cylinder of radius 0.05, oriented along the $z-$axis; it is centered in $(0,\ 0,\ 0)$ and its length is 1.

Figure 5.15 shows that when increasing the number of unknowns, the relative error of the proposed method with respect to the reference solution decreases, confirming the

correctness of the approach. When we do not take into account the presence of the fiber, the relative error increases with the number of unknowns.

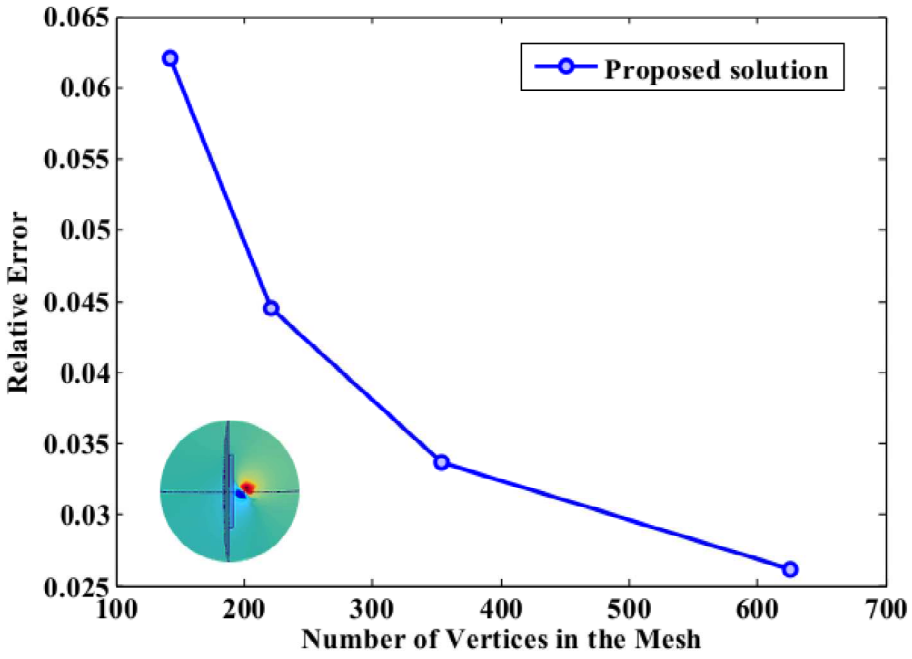

Figure 5.15: Relative error when increasing the number of unknowns with respect to a FEM solution in the presence of one fiber.

Another experiment was carried out in which 12 cylinders are put in the head media. The conductivity of the brain is set to 1 while the conductivity tensor of the fibers is set 10 times higher in the direction of the fibers, as it is commonly admitted to be the case in the white matter fibers [104]. The fibers have a radius of 0.05. The source is a dipole, positioned in the centre of the sphere and whose moment is $[1, 0, 1]$. Figure 5.16a shows the geometry. In this situation again, the proposed solution provides an accurate solution with a relative error in the range of the first simulation (where there was only one fiber). We can also see in Figure 5.16b that the relative error decreases with the number of unknowns

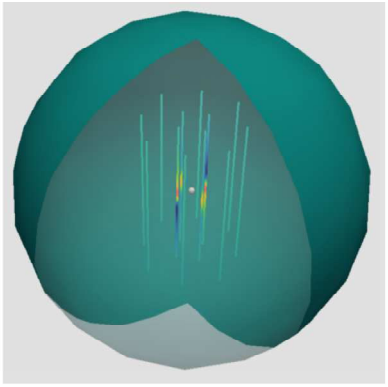

(a) The white sphere represents the dipole. The colors show the amplitude of the current on the wires.

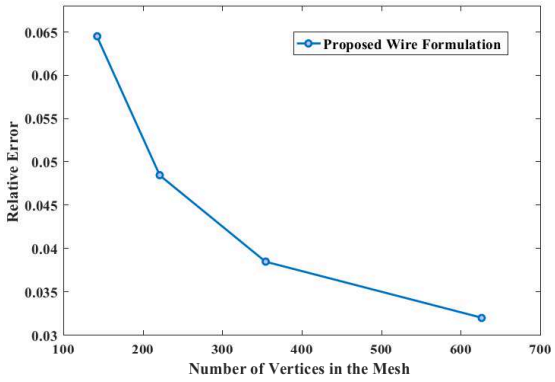

(b) Relative error when increasing the number of unknowns with respect to a FEM solution in the presence of 12 fibers.

Figure 5.16: Simulation with 12 fibers in a one layer spherical head mesh.

5.5 Discussion

This section presents an integral formulation for handling white matter fiber anisotropy. The proposed formulation is valid in a single layer domain containing three dimensional curves. The size of the matrix depends on the size of the mesh used to model the external layer (containing N_v vertices) and the size of the mesh representing the fibers (N_s cylinders). Two integral equations are needed for finding the potential and the generated currents in the fibers. The size of the matrix is then $O\left((N_v + N_s)^2\right)$. The proposed formulation has only been tested in simple cases and time estimates showed that the longest time is spent in computing the terms $[\mathbf{D}^*_{\mathbf{j}}]_{ij}$. Indeed these terms necessitates volumetric integral on the cylinders. In our implementation, only the integral along the fiber was done analytically. Efficient implementation and integration rules should be developed in order to assess correctly the timings with respect to the size of matrices.

5.6 Conclusion

This chapter presented an analysis of the spectral behaviour of wire EFIE. This analysis allowed to build a Calderon preconditioner for this equation. However the obtained pre-

conditioner depends on the geometry of the antenna. For closed structure, the proposed solution provides a constant condition number. For open structures, the Calderon solution is not satisfying since it does not allow to build a matrix spectrally equivalent to the inverse of the hypersingular operator involved. This is due to the property of the considered Sobolev spaces. It still provides a condition number that only grows logarithmically. The numerical experiments presented confirm the theoretical developments. The last part of the chapter introduced a wire integral formulation for dielectric media, namely the head. The formulation can take into account the white matter fiber anisotropy using one dimensional basis functions. It would however gained by being extended to multi-layered head geometry.

Chapter 6

A Fast Direct Solver for the EEG Forward Problem

This chapter studies the impact of a fast direct solver for the EEG forward problem. Such a solver enables to store the inverse of the system matrix in $O(N^{1.5})$ instead of $O(N^2)$ in the case of pure direct solver (where N is the number of unknowns in the system). The time complexity of the algorithm is found to be $O(N^2)$. Since the solution of the EEG inverse problem requires many solutions of the EEG forward problem, the advantage of a fast direct solver can be seen both in computing the solution of the inverse and in the forward EEG problem. This chapter presents preliminary results on the impact of the use of such a solver in forward modelling.

6.1 Introduction

Accurate solutions of the EEG forward problem necessitate high mesh density and the resulting system has a high number of unknowns [3]. Without any direct fast solving technique, only iterative solvers can be used to compute the solution of the EEG forward problem. Denoting with N the number of unknowns and k the number of iterations needed to achieve the desired accuracy, the cost of such a solution is in the order of $k \times N^2$. Moreover, since solving the EEG inverse problem requires many solutions of the EEG forward problem, the cost of solving the inverse problem is directly proportional to the cost of the

forward solution. There exist however many techniques such as multigrid, FFT, or Fast Multiple Methods (FMM) that can *accelerate* the obtention of the solution i.e., obtain the solution with a cost of $O(N\log(N))$. To solve the system, these techniques use iterative solvers which build a sequence of vectors that converge to the solution. This approach has been successfully applied to EEG in [55] for example. On the other hand, *direct* fast solvers provide an alternative to obtain the solution. Instead of iteratively approximating the solution, these fast solvers approximate the inverse of the system matrix. As a consequence, they are deterministic and they have a great advantage when multiple right hand side vectors are present, which is the case when building the leadfield matrix of the EEG inverse problem. This chapter introduces a fast direct solver for solving the EEG forward problem. The proposed fast solver is kernel free and achieves a complexity of $O(N^{1.5})$. The numerical experiments presents preliminary and promising results, for the use of direct fast solver in the context of EEG.

6.2 Inversion of Block Separable Matrices

In order to solve the following system

$$\mathbf{Ax} = \mathbf{b}, \tag{6.1}$$

a fast direct solver seeks to construct an approximation $\widetilde{\mathbf{S}}$ of $\mathbf{A^{-1}}$, the inverse of the matrix $\mathbf{A}$, such that

$$||\mathbf{A^{-1}} - \widetilde{\mathbf{S}}|| < \epsilon \tag{6.2}$$

The approximate solution $\widetilde{\mathbf{x}}$ is then simply obtained by matrix multiplication

$$\widetilde{\mathbf{x}} = \widetilde{\mathbf{S}}\mathbf{b}. \tag{6.3}$$

The matrix $\widetilde{S}$ can be built in a sparse format allowing for fast matrix vector multiplication. In fast direct solver, $\widetilde{\mathbf{S}}$ is built by exploiting low rank approximation. The possibility of

leveraging on this approximation is due to the physical property underlying the building of the system matrix.

6.2.1 Validity of Low Rank Approximation in the EEG Forward Problem

We seek to apply fast direct solver technique to the EEG forward problem when solved with boundary integral equations. In solving Poisson's problem (which governs the isotropic EEG forward problem)

$$\Delta\phi = f \tag{6.4}$$

with the boundary element method, we make use of the fundamental solution given by

$$G(\mathbf{r} - \mathbf{r}') = \frac{1}{4\pi||\mathbf{r} - \mathbf{r}'||}. \tag{6.5}$$

Figure 6.1 shows the graph of this function. It can been seen that the decay is extremely fast away from the origin. Actually this corresponds to the analyticity of the fundamental solutions away from the origin. This means that there is a loss of information over the distance.

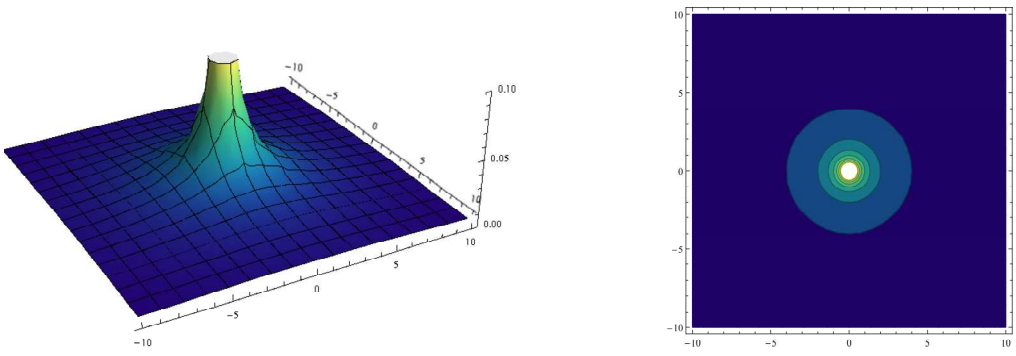

(a) (b)

Figure 6.1: Graph of the fundamental solution for the Laplace operator with a source in the center. The graphs have been truncated since the peak goes to infinity.

In the boundary element method, the system matrix that is built to numerically solve (6.4) is given by

$$[\mathbf{Z}]_{ij} = \langle f_i, Df_j \rangle \tag{6.6}$$

where D is an integral operator whose kernel is given by G as in (6.5) and $\{f_i\}$ is the set of testing functions. The solution is then obtained by solving the following system

$$\mathbf{Z}x = \mathbf{b}. \tag{6.7}$$

Given the analyticity of $G(r)$ away from the sources, we can expect that the eigenvalues of the off diagonal sublocks of the matrix $\mathbf{Z}$ will decay rapidly. This actually means that these off diagonal blocks will have a low (numerical) rank. This can be visualized by referring to Figure 6.2. We see that the interaction between the sources placed in the red square (in the origin) and the observation points placed in the black square, (away from the origin), has an amplitude that varies slowly; while the self interaction of the sources has a rapidly varying amplitude. These interactions are obtained hierarchically and a low rank approximation algorithm is applied to the blocks corresponding to the far interactions. This is the main concept behind the studied fast direct solver.

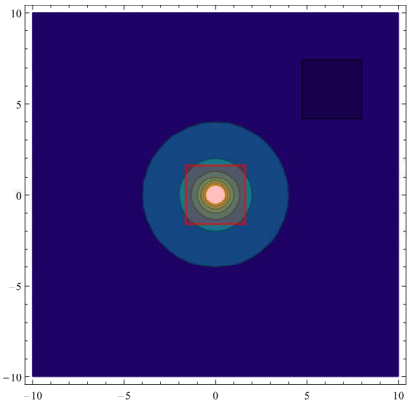

Figure 6.2: Schematic description of the block interaction in building the system matrix. The sources are represented by the red square while the observation points lie in the black square.

6.2.2 Hierarchical Partitioning

The hierarchical division in blocks of the system matrix $\mathbf{Z}$ is achieved with an octree. For didactic purpose we present how to build such a division with a quadtree. In handling 3D structures, this is achieved with an octree but the principle remains the same.

A tree is obtain by recursive partitioning of the index vector of the mesh data. The number of level L in the tree is given by the number of time the operation is performed. The integers $l = 1, ...L$ labels the levels of the tree. The *root* of the tree is the full set of indices. Let I_1 be the initial set of indices, $I_1 = 1, 2, ..., N$ where N is the number of elements. At each level, a subdivision of the sets of indices is performed. The process of subdivion is continued for each interval until it contains a fixed number of elements n. A node that cannot be split further is called a *leaf* of the tree. In a quad tree, a non-leaf node τ has four *children*, σ_1, σ_2, σ_3 and σ_4 such that $I_\tau = I_{\sigma_1} \cup I_{\sigma_2} \cup I_{\sigma_3} \cup I_{\sigma_4}$; τ is called the parent of σ_1, σ_2, σ_3 and σ_4. These notions are illustrated Figure 6.3 that shows the numbering of the indices in a fully populated tree. Note that the geometry usually does not provide ordered indices. A mapping from the ordered indices obtained using hierarchical partitioning to the indices in the geometry should be created.

6.2.3 Block separation of the System Matrix

With the previous notations, the system matrix $\mathbf{Z}$ can be separated into submatrices $\mathbf{Z}_{ij} = \mathbf{Z}_{I_i,I_j}$. The matrix is hierchically separated in blocks, with off diagonal blocks of rank r when

- For each leaf nodes, $\tau \neq \tau'$, the matrix $\mathbf{Z}_{\tau,\tau'}$ admits the decomposition

$$\begin{array}{ccccccc} \mathbf{Z}_{\tau,\tau'} & = & \mathbf{U}_\tau & & \widetilde{\mathbf{Z}}_{\tau,\tau'} & \mathbf{V}_{\tau'} \\ n \times n & & n \times r & & r \times r & r \times n \end{array} \tag{6.8}$$

- For the other non diagonal terms, at the levels $l = 1, \ldots, L-1$, the decompostion of the submatrix , $\mathbf{Z}_{\tau,\tau'}$ is done with respect to its children:

$$\mathbf{Z}_{\tau,\tau'} = \begin{pmatrix} \widetilde{\mathbf{Z}}_{\sigma_1,\sigma'_1} & \widetilde{\mathbf{Z}}_{\sigma_1,\sigma'_2} & \widetilde{\mathbf{Z}}_{\sigma_1,\sigma'_3} & \widetilde{\mathbf{Z}}_{\sigma_1,\sigma'_4} \\ \widetilde{\mathbf{Z}}_{\sigma_2,\sigma'_1} & \widetilde{\mathbf{Z}}_{\sigma_2,\sigma'_2} & \widetilde{\mathbf{Z}}_{\sigma_2,\sigma'_3} & \widetilde{\mathbf{Z}}_{\sigma_2,\sigma'_4} \\ \widetilde{\mathbf{Z}}_{\sigma_3,\sigma'_1} & \widetilde{\mathbf{Z}}_{\sigma_3,\sigma'_2} & \widetilde{\mathbf{Z}}_{\sigma_3,\sigma'_3} & \widetilde{\mathbf{Z}}_{\sigma_3,\sigma'_4} \\ \widetilde{\mathbf{Z}}_{\sigma_4,\sigma'_1} & \widetilde{\mathbf{Z}}_{\sigma_4,\sigma'_2} & \widetilde{\mathbf{Z}}_{\sigma_4,\sigma'_3} & \widetilde{\mathbf{Z}}_{\sigma_4,\sigma'_4} \end{pmatrix} \tag{6.9}$$

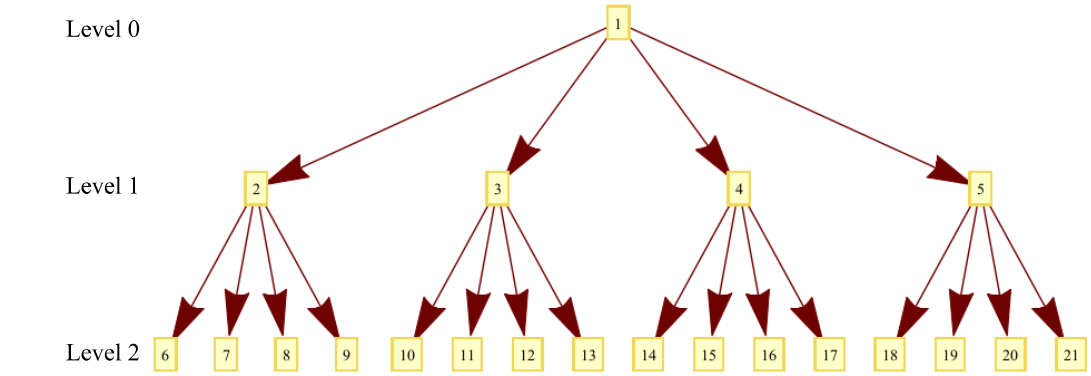

(a)

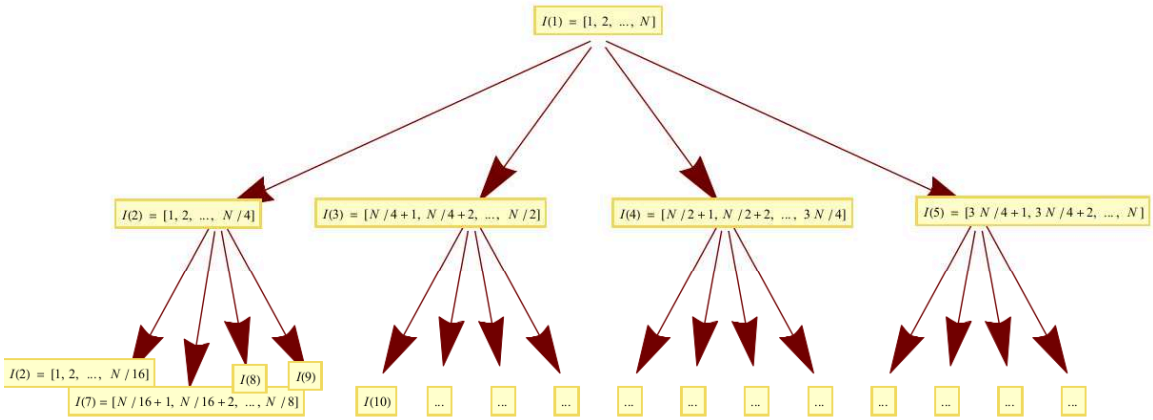

(b)

Figure 6.3: Two levels of a quad tree, showing the root of the tree, I_1, its children I_2, I_3, I_4 and the leaf nodes $\{I_i\}_{i=6}^{21}$. A partition of the indices is presented (b).

such that

$$\begin{array}{cccccc} \mathbf{Z}_{\tau,\tau'} & = & \mathbf{U}_{\tau} & \widetilde{\mathbf{Z}}_{\tau,\tau'} & \mathbf{V}_{\tau'} \\ 4r \times 4r & & 4r \times r & r \times r & r \times 4r \end{array} \tag{6.10}$$

At the first level, the matrix $\mathbf{Z}$ can thus be efficiently represented with

$$\mathbf{Z} = \begin{bmatrix} \mathbf{Z}_{11}^{(1)} & 0 & 0 & 0 \\ 0 & \mathbf{Z}_{22}^{(1)} & 0 & 0 \\ 0 & 0 & \mathbf{Z}_{33}^{(1)} & 0 \\ 0 & 0 & 0 & \mathbf{Z}_{44}^{(1)} \end{bmatrix} + \begin{bmatrix} \mathbf{U}_{11}^{(1)} & 0 & 0 & 0 \\ 0 & \mathbf{U}_{22}^{(1)} & 0 & 0 \\ 0 & 0 & \mathbf{U}_{33}^{(1)} & 0 \\ 0 & 0 & 0 & \mathbf{U}_{44}^{(1)} \end{bmatrix} \begin{bmatrix} 0 & \tilde{\mathbf{Z}}_{12}^{(1)} & \tilde{\mathbf{Z}}_{13}^{(1)} & \tilde{\mathbf{Z}}_{14}^{(1)} \\ \tilde{\mathbf{Z}}_{21}^{(1)} & 0 & \tilde{\mathbf{Z}}_{23}^{(1)} & \tilde{\mathbf{Z}}_{24}^{(1)} \\ \tilde{\mathbf{Z}}_{31}^{(1)} & \tilde{\mathbf{Z}}_{32}^{(1)} & 0 & \tilde{\mathbf{Z}}_{34}^{(1)} \\ \tilde{\mathbf{Z}}_{41}^{(1)} & \tilde{\mathbf{Z}}_{42}^{(1)} & \tilde{\mathbf{Z}}_{43}^{(1)} & 0 \end{bmatrix} \begin{bmatrix} \mathbf{V}_{11}^{(1)} & 0 & 0 & 0 \\ 0 & \mathbf{V}_{22}^{(1)} & 0 & 0 \\ 0 & 0 & \mathbf{V}_{33}^{(1)} & 0 \\ 0 & 0 & 0 & \mathbf{V}_{44}^{(1)} \end{bmatrix} \tag{6.11}$$

$$= \mathbf{D}^{(1)} + \mathbf{U}^{(1)}\mathbf{T}^{(1)}\mathbf{V}^{(1)}$$

Using the previously presented tree, this means that

$$\mathbf{Z} = \mathbf{D}^{(L)} + \sum_{l=1}^{L} \mathbf{U}^{(l)}\mathbf{T}^{(l)}\mathbf{V}^{(l)} \tag{6.12}$$

and it is sufficient for storing the matrix to know the diagonal blocks $\mathbf{D}_\tau = \mathbf{Z}(I_\tau, I_\tau)$ for each leaf node, the basis for the columns $\mathbf{U}_\tau^{(l)}$, the basis for the row $\mathbf{V}_\tau^{(l)}$ and the interaction between the children $\mathbf{T}_\tau^{(l)}$. This decomposition is typical of Hierarchically Off Diagonal Low Rank matrices (HODLR) [62].

6.2.4 HODLR Matrix Construction

It is well known that the optimal approximation of rank r $\widetilde{\mathbf{A_r}}$ of a matrix $\mathbf{A}$ is given by the Singular Value Decomposition(SVD). In other words

$$min\left(||\mathbf{A} - \widetilde{\mathbf{A_r}}||\right) = ||\mathbf{A} - \mathbf{A_r}|| = \sigma_{r+1} \tag{6.13}$$

where $\mathbf{A_r}$ is given by the truncated SVD of $\mathbf{A}$. This is the procedure we would like to use to build the basis U and V. However, direct application of the algorithm is expensive. For this reason, we opted for the the method described in [62] to build the required factorization.

We seek to build the factorization with a rank r approximation of the off-diagonal blocks of the matrix $\mathbf{Z}$. We are looking for the factorisation of $\mathbf{Z}_{\tau,\tau'}$, $\tau \neq \tau'$ such that:

$$\mathbf{Z}_{\tau,\tau'} \approxeq \widetilde{\mathbf{Z}}_{\tau,\tau'} = \mathbf{U}\mathbf{\Sigma}\mathbf{V}. \tag{6.14}$$

We begin presenting the general procedure to obtain the approximate factorization of matrix of rank r. Denote with $\mathbf{Z}_{\alpha,\beta}$ this matrix block. The procedure is decomposed into six steps:

1. Build a random matrix $\mathbf{\Omega}$ of size $N \times r$

2. Sample the range of $\mathbf{Z}_{\alpha,\beta}$ by forming

$$\mathbf{Y} = \mathbf{Z}_{\alpha,\beta}\mathbf{\Omega}$$

3. Orthonormalize the columns of $\mathbf{Y}$, which can be done using QR-decomposition. This means, we need to find $\mathbf{Q}$ and $\mathbf{R}$ such that

$$\mathbf{Y} = \mathbf{Q}_\alpha\mathbf{R}$$

By doing this we obtain an orthonormal basis for range of $\mathbf{Z}_{\alpha,\beta}$.

4. Compute $\mathbf{B} = \mathbf{Q}_\alpha{}^H \mathbf{Z}_{\alpha,\beta}$, an $r \times N$ matrix.

5. Compute the SVD of $\mathbf{B} = \widetilde{\mathbf{U}}\mathbf{\Sigma}_{\alpha\beta}\mathbf{V}_\alpha$

6. Get $\mathbf{U}_\alpha = \mathbf{Q}_\alpha \widetilde{\mathbf{U}}$

After this procedure, we built the factorization of rank r of the matrix block $\mathbf{Z}_{\alpha,\beta} = \mathbf{U}_\alpha \mathbf{\Sigma}_{\alpha\beta} \mathbf{V}_\alpha$. However this procedure necessitates to know the rank r of $\mathbf{Z}_{\alpha,\beta}$ in advance. Error estimates are necessary to select its optimal value. Moreover, the process described is carried out in the context of low rank *approximation*, this means that the rank of $\mathbf{Z}_{\alpha,\beta}$ is not exactly r. Oversampling is necessary (build $r + p$ random vector in the beginning) to decrease the probability of failure. In our approach, we select $p = 5$.

To build the hierarchical decomposition of $\mathbf{Z}$ as in (6.12), we simply need to apply the previous algorithm recursively, starting from the first (coarsest) level of the tree. The diagonal blocks $D^{(l)}$ are not rank deficient and they need to be extracted by computing the difference between $\mathbf{Z}$ and its off-diagonal blocks. The procedure is detailed in [62].

6.2.5 Inversion of the HODLR Matrix

Now that the hierarchical structure of the matrix $\mathbf{Z}$ is known, we can build its inverse efficiently. The key point is the Woodbury formula [46]:

$$(\mathbf{D} + \mathbf{UTV})^{-1} = \mathbf{D}^{-1} - \mathbf{D}^{-1}\mathbf{U}\left(\mathbf{T}^{-1} + \mathbf{VD}^{-1}\mathbf{U}\right)\mathbf{VD}^{-1} \tag{6.15}$$

At the level L, the hierarchical decomposition of $\mathbf{Z}$ is given by

$$\begin{aligned} \mathbf{Z} &= \mathbf{D}^{(L)} + \sum_{l=1}^{L} \mathbf{U}^{(l)}\mathbf{T}^{(l)}\mathbf{V}^{(l)} \\ \Leftrightarrow \mathbf{Z} &= \mathbf{D}^{(L)} \left(\mathbf{I} + \mathbf{D}^{(L)^{-1}} \sum_{l=1}^{L} \mathbf{U}^{(l)}\mathbf{T}^{(l)}\mathbf{V}^{(l)} \right) \end{aligned} \tag{6.16}$$

If we build the matrix $\widetilde{\mathbf{U}}^{(l)} = \mathbf{D}^{(L)^{-1}}\mathbf{U}^{(l)}$, then

$$\mathbf{Z} = \mathbf{D}^{(L)}\left(\mathbf{I} + \widetilde{\mathbf{U}}^{(L)}\mathbf{T}^{(L)}\mathbf{V}^{(L)} + \sum_{l=1}^{L-1}\widetilde{\mathbf{U}}^{(l)}\mathbf{T}^{(l)}\mathbf{V}^{(l)}\right) \tag{6.17}$$

Denoting with $\widetilde{\mathbf{Z}}^{(L)}$ the matrix given by $\mathbf{I} + \widetilde{\mathbf{U}}^{(Ll)}\mathbf{T}^{(L)}\mathbf{V}^{(L)}$, then (6.17) becomes

$$\mathbf{Z} = \mathbf{D}^{(L)}\left(\widetilde{\mathbf{Z}}^{(L)} + \sum_{l=1}^{L-1}\widetilde{\mathbf{U}}^{(l)}\mathbf{T}^{(l)}\mathbf{V}^{(l)}\right) \tag{6.18}$$

And the process can be continued for each level of the tree, by factorizing out $\widetilde{\mathbf{Z}}^{(k)}$ at each level and updating $\widetilde{\mathbf{U}}^{(l)} = \widetilde{\mathbf{Z}}^{(k)^{-1}}\widetilde{\mathbf{U}}^{(l)}$. We then obtain the following factorization of $\mathbf{Z}$

$$\mathbf{Z} = \mathbf{D}^{(L)}\widetilde{\mathbf{Z}}^{(L)}\widetilde{\mathbf{Z}}^{(L-1)}\ldots\widetilde{\mathbf{Z}}^{(2)}\widetilde{\mathbf{Z}}^{(1)} \tag{6.19}$$

The solution to equation (6.7) (and any system $\mathbf{Z}x = \mathbf{b}$ where $\mathbf{Z}$ is a HODLR matrix) can then simply be obtained by

$$x = \widetilde{\mathbf{Z}}^{(1)^{-1}}\widetilde{\mathbf{Z}}^{(2)^{-1}}\ldots\widetilde{\mathbf{Z}}^{(L-1)^{-1}}\widetilde{\mathbf{Z}}^{(L)^{-1}}\mathbf{D}^{(L)^{-1}}\mathbf{b} \tag{6.20}$$

that is by recursively applying the inverse of $\widetilde{\mathbf{Z}}^{(l)}$. Note that $\mathbf{D}^{(L)}$ is a block diagonal matrix of rank r and as a consequence computing its inverse depends only on the size of these blocks, that is the size of the clusters in the leaves of the tree. The inverses $\widetilde{\mathbf{Z}}^{(l)^{-1}} = \left(\mathbf{I} + \widetilde{\mathbf{U}}^{(l)}\mathbf{T}^{(l)}\mathbf{V}^{(l)}\right)^{-1}$ are obtained by direct application of the Woodbury formula (6.15)

6.3 Numerical Results

We applied the presented algorithm to the EEG forward problem solved using the double layer formulation. However since the presented algorithm is kernel free, this choice could be different.

We rapidly recall the double layer formulation and the associated system matrix for solving the EEG forward problem 1.8 using boundary element method. This formulation

has been presented in Chapter 3, for more details the reader is also referred to [54]. Consider a layered domain $\Omega = \cup_{i=1}^{N} \Omega_i$ whose interfaces are given by $\Gamma_i = \partial_{\Omega_i} \cap \partial_{\Omega_{i+1}}$. With these notations, the double layer formulation reads

$$v_{\Gamma_i} = \frac{\sigma_i + \sigma_{i+1}}{2} \phi_{\Gamma_i} - \sum_{j=1}^{N} (\sigma_{j+1} - \sigma_j) D_{ij} \phi_{\Gamma_j} \tag{6.21}$$

where D is the double layer operator:

$$D\Psi(r) = \int_{\Gamma} \Psi(r') \partial_{\vec{n}'} G(r - r') dr', \; D : H^{1/2}(\Gamma) \to H^{1/2}(\Gamma) \tag{6.22}$$

and v_{Γ_i} is the potential computed on Γ_i generated by the dipolar source in an infinite medium. The unknown potential on the interface Γ_i is given by ϕ_{Γ_i}. Using the boundary element methods, after discretization of the geometry into N triangles and expansion of the unknown with piecewise constant basis functions $\{P_{0i}\}_{i=1}^{N_t}$, the system that arises is

$$\mathbf{Z}x = \mathbf{b} \tag{6.23}$$

with

$$[\mathbf{Z}]_{ij} = \begin{cases} \dfrac{\sigma_i + \sigma_{i+1}}{2} \langle P_{0i}, P_{0j} \rangle & \text{if } i = j \\ -(\sigma_{j+1} - \sigma_j) \langle P_{0i}, D_{ij} P_{0j} \rangle & \text{otherwise,} \end{cases} \tag{6.24}$$

and

$$[b]_i = \langle P_{0i}, v_{t_i} \rangle. \tag{6.25}$$

The vector x contains the expansion coefficients.

6.3.1 Relative Error and Low Rank Approximation

The first numerical experiments was performed in a three layered sphere. It aimed at checking that low rank approximation was valid for solving the EEG forward problem. The layered sphere contains 500 cells per layer. The obtained solution for high rank ($r = 200$) is exactly the same as the solution provided by the standard double layer formulation without any fast direct solving techniques as can be seen Figure 6.4.

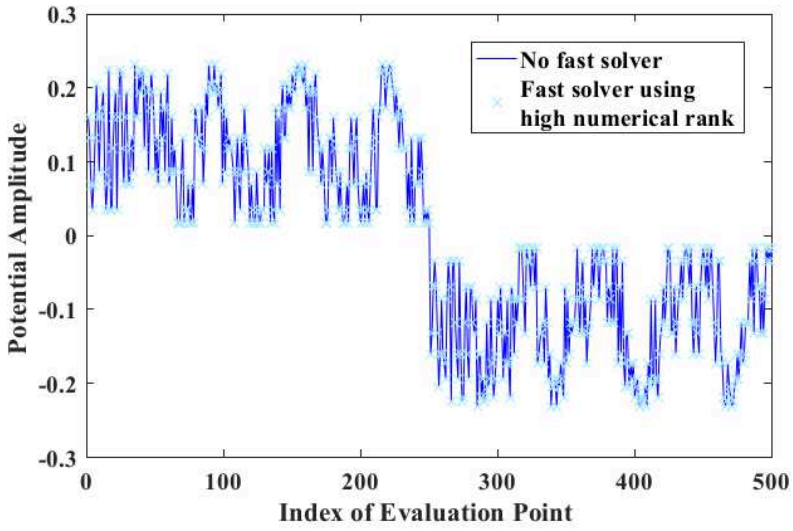

Figure 6.4: Comparison of the solution obtained with and without fast solver in the case where a high approximation rank was selected.

In a second experiment, using the same mesh, the rank was gradually decreased from 700 to 5 and the obtained solution was compared to the analytical solution presented in [106]. For each choice of rank approximation, the relative error was computed. The results are shown in Figure 6.5. It can be observed that from rank 700 to 90, the relative error is stable. This is in agreement with the assumption that the system matrix could actually be approximated with a low numerical rank matrix. The figure displays also the necessary memory for storing the HODLR decomposition of the matrix with respect to the chosen rank. To summarize this experiment shows that by approximating the system matrix with the proposed fast solver, the needs in memory can easily be decreased while keeping the same accuracy.

6.3.2 Memory and Complexity of the Solver

To apply the described fast solver, it is necessary to estimate the optimal rank r_0 that minimizes the cost of the storing the matrix and that does not change the accuracy of the method. To this aim, we repeated the previous experiments for two other meshes, a coarser mesh with 320 cells per layer and a denser mesh with 1280 cells per layer. The results are shown

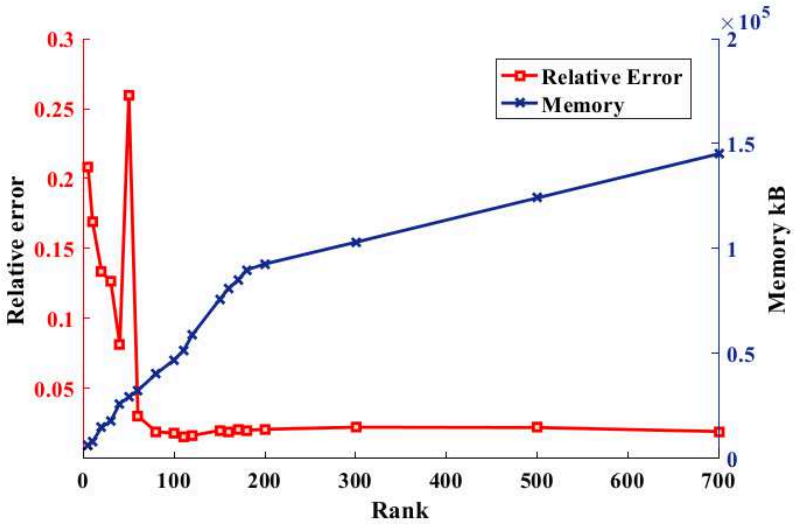

Figure 6.5: Relative error of the solution obtained with the fast solver for different rank approximations and associated memory requirements for storing the inverse.

in Figure 6.6. First note that, the denser the mesh, the more accurate the solution. This experiments aimed at estimating the optimal rank for our problem. For each mesh we selected as *optimal* the lowest rank for which the relative error is equal or smaller than the relative error given by the highest rank. In this numerical experiment we also paid attention to the the memory needed to store the HODLR matrices as shown in Figure 6.7 and the time for performing the inversion, displayed Figure 6.8. The results for the selected rank are shown in table 6.1 (the experiment was performed for a fourth mesh with 888 cells per interface in order to confirm the results, but for clarity purposes in the figures the associated curve is not shown). In table 6.2, we show the time that a conjugate gradient (CGS) solver needs to solve the same problem. For a single RHS vector and the meshes employed, it cannot be expected that the presented algorithm will be faster, since the time for building the HODLR matrix is much longer than the time needed to get the solution with CGS. However the direct inversion, once the HODLR matrix is obtained, is very fast compared to the time needed to compute the solution with the CGS.

The previous experiment allowed to highlight the complexity of the solver. In com-

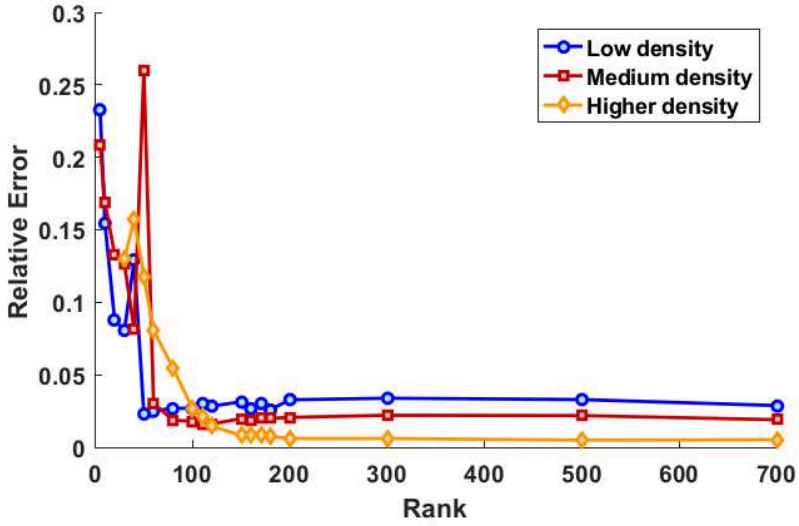

Figure 6.6: Relative error of the solution computed with the fast solver with respect to the analytical solution for different rank approximation and three different meshes.

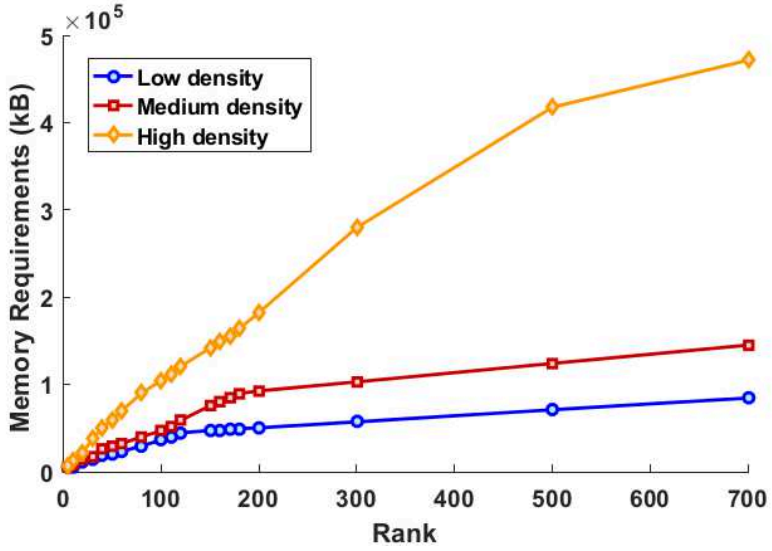

Figure 6.7: Memory requirements for building the HODLR matrix in computing the solution computed with the fast solver with respect to the analytical solution for different rank approximation and three different meshes.

paring the memory requirements with respect to the number of unknowns for the optimal ranks, we observe that it is in the order of $O(N^{1.5})$. This is shown in Figure 6.9 where the data of table 6.1 is plotted with respect to the number of unknowns. The gain with respect to storing directly the inverse of the matrix is confirmed by Figure 6.9. The curve showing the computation of the necessary memory $^{2/3}$ displays a linear behavior.

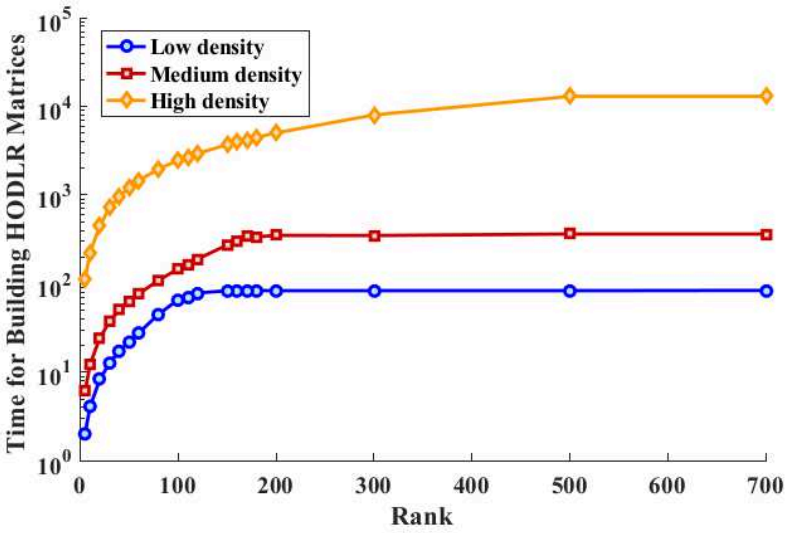

Figure 6.8: Time necessitated for building the HODLR matrix in computing the solution computed with the fast solver with respect to the analytical solution for different rank approximation and three different meshes.

Number of unknowns	Optimal rank	Memory (kB)	Building Time (s)	Solving Time (s)
960	60	25004	27	0.077
1500	80	42320	76	0.13
2664	150	104204	909	0.37
3840	180	163916	4482	0.76

Table 6.1: Selected rank and associated memory requirements for storing the HODLR matrix and the time necessary to build it for four meshes.

Number of unknowns	Time cgs (s)
960	0.12
1500	0.32
2664	1.51
3840	3.62

Table 6.2: Time for solving the EEG forward problem with the double layer formulation and CGS.

6.4 Conclusion

This chapter presented a fast direct solver for the EEG forward problem. It confirmed that low rank approximation was valid for solving the EEG forward problem and therefore shows that fast direct solvers are of high interest in the context of EEG. The numerical results show a memory cost of $O(N^{1.5})$ for the building of the HODLR matrix with the

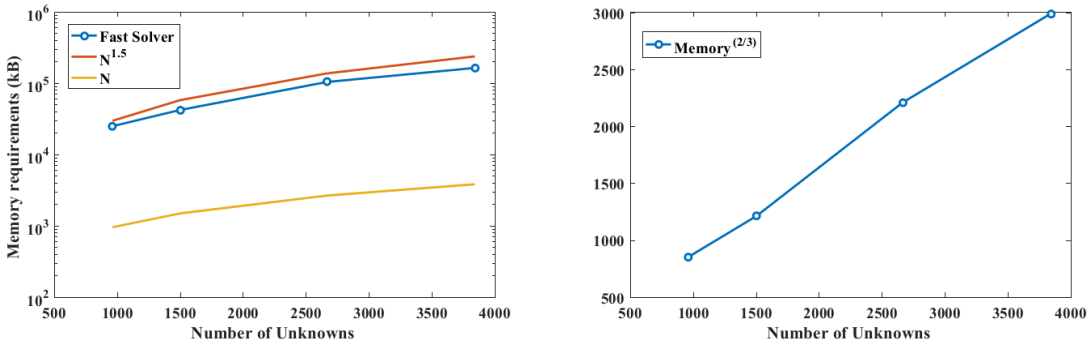

(a) (b)

Figure 6.9: Memory needs for building the HODLR matrix with respect to the number of unknowns (a). The second graph, on the right (b) displays the same curve rectified for a linear scale.

proposed algorithm. The time needed to build such a matrix has also been shown. It has been observed that for the small meshes for which the experiments were carried out, using a conjugate gradient algorithm is faster (since in this case it is not necessary to build the intermediate HODLR matrix). The gain in time could only be seen for denser mesh but this would necessitate to build, in a faster manner, the interaction matrix, for example with an Adaptive Cross Approximation (ACA) algorithm. However, the numerical experiments showed that there is a clear advantage in using the presented fast direct solver in terms of memory and time necessary to obtain the solution once the HODLR composition is known. The preliminary work presented in this chapter aimed at introducing fast direct solvers in the context the EEG source reconstruction. Future investigations will include the implementation of a fast direct solver with linear complexity. The work seeks to impact real time brain imaging with EEG in particular in the field of brain computer interfaces.

Chapter 7

Conclusion and Future Work

This manuscript gathers three years of doctoral work on 1-, 2- and 3-D integral equations for the modelling of the EEG forward problem. It started by recalling how from Maxwell's equation it is possible to derive the EEG forward problem. The treatment goes on by presenting the boundary element method, the numerical technique that we chose to tackle this specific electromagnetic problem. Indeed this technique permits to discretize only the interface of media with different dielectric properties. As such, it is expected to decrease the computational burden with respect to finite element method. It also has the advantage of intrinsically presenting high accuracy.

In order to tackle the weakness of the existing integral formulations for solving the EEG forward problem, namely the lack of anisotropy in their approach, two new integral formulations were presented. The first proposed integral formulation leverages on an indirect approach to build a harmonic function in each compartment of the head that has a different conductivity tensor. This approach even if it requires two unknowns per surface has the advantage that it can naturally deals with non nested geometries. This leads to the ability to handle, through volume meshes, any inhomogeneous and anisotropic conductivity profile. The proposed implementation naturally simplifies the geometry into surface mesh when the conductivity is isotropic. In this chapter, we also took into account the mapping properties of the operators by obtaining the system matrix with a mixed discretization. The efficiency

of this type of discretization in solving the EEG forward problem was also assessed and resulted to be favourable with respect to standard Galerkin discretization.

The second proposed formulation exploits the one-dimensionality of the white matter fibers to take its anisotropy into account. Currently the formulation handles only fibers in one layer. But the numerical results are satisfying and show that the simplification of the fiber in one dimension curve seems to be correct.

Primary to the introduction of this second formulation, a spectral analysis of the wire EFIE was proposed. This led to the development of a new Calderon preconditioner for this equation. A Calderon preconditioning technique was also studied in the context of EEG. The novelty here was to show that the Calderon identities in 2D and homogeneous media often used in high frequency problems can be extended to multilayer media. This approach was applied to the EEG symmetric formulation to confirm the theoretical developments.

A last chapter presented preliminary results on the application of a fast direct solver in solving the EEG forward Problem. Using hierarchical partitioning of the system matrix, we showed substantial acceleration of the solution of the forward problem.

The material presented in this manuscript opens several paths for future investigation:

- First of all, the assessment of the effects of the mixed discretization in the EEG inverse problem could be extended to multiple sources localization. This comparison could include the newly proposed formulations.

- Moreover, the proposed formulation for the modelling of the white matter fiber can be extended to multilayer media to become more realistic. A merging of the two proposed formulations can also be considered given the indirect nature of the new surface anisotropic formulation.

- The treatment on the spectral properties of the EFIE can be extended to theoretically and rigorously prove the logarithmic behaviour of the condition number of the proposed preconditioned system matrix. Moreover, since it is shown that this equation is equivalent to a Laplacian operator, another efficient way to precondition it may be to efficiently build the inverse of the Laplacian directly.

- Preconditioners for the EEG symmetric formulation can be useful to develop accurate and fast solution of the EEG forward problem. Obtaining accurate solutions rapidly is a considerable advantage if one is to develop real time applications. This solution can then be merged with fast solver and utilized for example in inverse source based BCI. In this context, it would also be of interest to develop a fast solver for the new integral formulations.

- The technique for preconditioning multilayer integral equations could also be employed in the context of high frequency problems with multilayer dielectric media.

- The application of the fast solver employed in Chapter 4 could be used in the framework of solving the EEG inverse problem. Such a tool could enable higher resolution and faster EEG brain source reconstruction.

List of Publications

Journal Contributions

- Axelle Pillain, Lyes Rahmouni, Rajendra Mitharwal, Maksims Abalenkov, Franceso P. Andriulli, "EEG Brain Source Reconstruction Based on Mixed Discretization of the Forward Problem", *in preparation*

- Axelle Pillain, Lyes Rahmouni, Francesco P. Andriulli, "A New Surface Integral Equation to Handle Anisotropic Conductivities in the EEG Forward Problem", *submitted*

- John Erick Ortiz Guzman, Axelle Pillain, Lyes Rahmouni, "A Calderon Regularized Symmetric Formulation for the EEG Forward Problem", *submitted*

Conference Contributions

- Axelle Pillain, Lyes Rahmouni, and Francesco P. Andriulli, "On an indirect boundary element method for the anisotropic EEG forward problem." *Antennas and Propagation (EuCAP), 2015 9th European Conference on, pp. 1-3. IEEE, 2015.*

- Axelle Pillain, Lyes Rahmouni, and Francesco P. Andriulli, "A Mixed Discretized Boundary Element Method for the Anisotropic EEG Forward Problem", *Engineering in Medicine and Biology Society (EMBC), 2015 37th Annual International Conference of the IEEE, pp.4061-4064. IEEE, 2015.*

- Axelle Pillain, Lyes Rahmouni, and Francesco P. Andriulli, ”On the Handling of Brain Tissue Anisotropy in the Forward EEG Problem with a Conformingly Discretized Surface Integral Method.” *Biomedical Imaging (ISBI), 2016 IEEE 13th International Symposium. IEEE, 2016.*

- John Eric Ortiz Guzman, Axelle Pillain, Lyes Rahmouni, and Francesco P. Andriulli, ”On the Preconditioning of the Symmetric Formulation for the EEG Forward Problem by Leveraging on Calderon Formulas”, *Biomedical Imaging (ISBI), 2016 IEEE 13th International Symposium. IEEE, 2016.*

Bibliography

[1] Y.A. Abramovich and C.D. Aliprantis. *An Invitation to Operator Theory*. Number vol. 1 in Graduate studies in mathematics. American Mathematical Society, 2002.

[2] M. Abramowitz and I.A. Stegun. *Handbook of Mathematical Functions: With Formulas, Graphs, and Mathematical Tables*. Applied mathematics series. Dover Publications, 1964.

[3] Zeynep Akalin Acar and Scott Makeig. Effects of Forward Model Errors on EEG Source Localization. *Brain Topography*, 26(3):378–396, January 2013.

[4] R.A. Adams and J.J.F. Fournier. *Sobolev Spaces*. Pure and Applied Mathematics. Elsevier Science, 2003.

[5] Geoffray Adde, Maureen Clerc, Olivier Faugeras, Renaud Keriven, Jan Kybic, and Théodore Papadopoulo. Symmetric bem formulation for the m/eeg forward problem. In *Information Processing in Medical Imaging*, pages 524–535. Springer, 2003.

[6] Francesco P. Andriulli, Kristof Cools, Hakan Bagci, Femke Olyslager, Annalisa Buffa, Snorre Christiansen, and Eric Michielssen. A Multiplicative Calderon Preconditioner for the Electric Field Integral Equation. *IEEE Transactions on Antennas and Propagation*, 56(8):2398–2412, August 2008.

[7] Francesco P Andriulli, Anita Tabacco, and Giuseppe Vecchi. Solving the EFIE at Low Frequencies With a Conditioning That Grows Only Logarithmically With

the Number of Unknowns. *IEEE Transactions on Antennas and Propagation*, 58(5):1614–1624, May 2010.

[8] O Axelson. Iterative solution methods. 1996.

[9] S Baillet, JJ Riera, G Marin, JF Mangin, J Aubert, and L Garnero. Evaluation of inverse methods and head models for eeg source localization using a human skull phantom. *Physics in medicine and biology*, 46(1):77, 2001.

[10] Constantine A. Balanis. *Antenna theory: analysis and design*. Wiley-Interscience, Hoboken, NJ, 3. ed edition, 2005.

[11] Nitin B Bangera, Donald L Schomer, Nima Dehghani, Istvan Ulbert, Sydney Cash, Steve Papavasiliou, Solomon R Eisenberg, Anders M Dale, and Eric Halgren. Experimental validation of the influence of white matter anisotropy on the intracranial eeg forward solution. *Journal of computational neuroscience*, 29(3):371–387, 2010.

[12] Hanna Becker, Laurent Albera, Pierre Comon, Rémi Gribonval, Fabrice Wendling, and Isabelle Merlet. A performance study of various brain source imaging approaches. In *Acoustics, Speech and Signal Processing (ICASSP), 2014 IEEE International Conference on*, pages 5869–5873. IEEE, 2014.

[13] Hanna Becker, Laurent Albera, Pierre Comon, Martin Haardt, Gwénaël Birot, Fabrice Wendling, Martine Gavaret, Christian-George Bénar, and Isabelle Merlet. EEG extended source localization: tensor-based vs. conventional methods. *NeuroImage*, 96:143–157, 2014.

[14] D. Beke, K. Cools, F. Olyslager, and E. Michielssen. Preconditioning of wire simulations in the presence of junctions. In *IEEE Antennas and Propagation Society International Symposium, 2009. APSURSI '09*, pages 1–4, June 2009.

[15] David Beke. *Preconditioning of wire simulations*. PhD thesis, 2007.

[16] Oscar P Bruno and Michael C Haslam. Regularity theory and superalgebraic solvers for wire antenna problems. *SIAM Journal on Scientific Computing*, 29(4):1375–1402, 2007.

[17] Helmut Buchner, Gunter Knoll, Manfred Fuchs, Adrian Rienäcker, Rainer Beckmann, Michael Wagner, Jiri Silny, and Jörg Pesch. Inverse localization of electric dipole current sources in finite element models of the human head. *Electroencephalography and clinical Neurophysiology*, 102(4):267–278, 1997.

[18] Annalisa Buffa and Snorre Christiansen. A dual finite element complex on the barycentric refinement. *Mathematics of Computation*, 76(260):1743–1769, 2007.

[19] E. Cances, B. Mennucci, and J. Tomasi. A new integral equation formalism for the polarizable continuum model: Theoretical background and applications to isotropic and anisotropic dielectrics. *The Journal of Chemical Physics*, 107(8):3032–3041, 1997.

[20] D Louis Collins, Alex P Zijdenbos, Vasken Kollokian, John G Sled, Noor J Kabani, Colin J Holmes, and Alan C Evans. Design and construction of a realistic digital brain phantom. *IEEE transactions on medical imaging*, 17(3):463–468, 1998.

[21] B Neil Cuffin. Eeg localization accuracy improvements using realistically shaped head models. *Biomedical Engineering, IEEE Transactions on*, 43(3):299–303, 1996.

[22] Tie Jun Cui and Weng Cho Chew. Accurate analysis of wire structures from very-low frequency to microwave frequency. *Antennas and Propagation, IEEE Transactions on*, 50(3):301–307, 2002.

[23] Sarang S Dalal, Johanna M Zumer, Adrian G Guggisberg, Michael Trumpis, Daniel DE Wong, Kensuke Sekihara, and Srikantan S Nagarajan. Meg/eeg source reconstruction, statistical evaluation, and visualization with nutmeg. *Computational intelligence and neuroscience*, 2011, 2011.

[24] Anders M Dale, Bruce Fischl, and Martin I Sereno. Cortical surface-based analysis: I. segmentation and surface reconstruction. *Neuroimage*, 9(2):179–194, 1999.

[25] Anders M Dale, Arthur K Liu, Bruce R Fischl, Randy L Buckner, John W Belliveau, Jeffrey D Lewine, and Eric Halgren. Dynamic statistical parametric mapping: combining fmri and meg for high-resolution imaging of cortical activity. *Neuron*, 26(1):55–67, 2000.

[26] JC De Munck. The potential distribution in a layered anisotropic spheroidal volume conductor. *Journal of applied Physics*, 64(2):464–470, 1988.

[27] J.C. de Munck, B.W. van Dijk, and H. Spekreijse. Mathematical dipoles are adequate to describe realistic generators of human brain activity. *Biomedical Engineering, IEEE Transactions on*, 35(11):960–966, Nov 1988.

[28] Qianqian Fang. Mesh-based monte carlo method using fast ray-tracing in plücker coordinates. *Biomedical optics express*, 1(1):165–175, 2010.

[29] Qianqian Fang and D. A. Boas. Tetrahedral mesh generation from volumetric binary and grayscale images. In *2009 IEEE International Symposium on Biomedical Imaging: From Nano to Macro*, pages 1142–1145, June 2009.

[30] M. Fuchs, R. Drenckhahn, H. Wischmann, and M. Wagner. An improved boundary element method for realistic volume-conductor modeling. *IEEE Transactions on Biomedical Engineering*, 45, 1998.

[31] Manfred Fuchs, Michael Wagner, and Jörn Kastner. Boundary element method volume conductor models for EEG source reconstruction. *Clinical neurophysiology*, 112(8):1400–1407, 2001.

[32] M. Gavaret, L. Maillard, and J. Jung. High-resolution EEG (HR-EEG) and magnetoencephalography (MEG). *Neurophysiologie Clinique/Clinical Neurophysiology*, 45(1):105–111, March 2015.

[33] Walton C. Gibson. *The Method of Moments in Electromagnetics 2nd Ed.* CRC press, 2014.

[34] Roberto D. Graglia. On the numerical integration of the linear shape functions times the 3-D Green's function or its gradient on a plane triangle. *Antennas and Propagation, IEEE Transactions on*, 41(10):1448–1455, 1993.

[35] Alexandre Gramfort, Matthieu Kowalski, and Matti Hämäläinen. Mixed-norm estimates for the M/EEG inverse problem using accelerated gradient methods. *Physics in Medicine and Biology*, 57(7):1937–1961, April 2012.

[36] Alexandre Gramfort, Théodore Papadopoulo, Emmanuel Olivi, Maureen Clerc, and others. OpenMEEG: opensource software for quasistatic bioelectromagnetics. *Biomed. Eng. Online*, 9(1):45, 2010.

[37] Roberta Grech, Tracey Cassar, Joseph Muscat, Kenneth P Camilleri, Simon G Fabri, Michalis Zervakis, Petros Xanthopoulos, Vangelis Sakkalis, and Bart Vanrumste. Review on solving the inverse problem in EEG source analysis. *Journal of Neuro-Engineering and Rehabilitation*, 5(1):25, 2008.

[38] Frédéric Grouiller, João Jorge, Francesca Pittau, Wietske van der Zwaag, Giannina Rita Iannotti, Christoph Martin Michel, Serge Vulliémoz, Maria Isabel Vargas,

and François Lazeyras. Presurgical brain mapping in epilepsy using simultaneous eeg and functional mri at ultra-high field: feasibility and first results. *Magnetic Resonance Materials in Physics, Biology and Medicine*, pages 1–12, 2016.

[39] D. Gullmar, J. Haueisen, M. Eiselt, F. Giessler, L. Flemming, A. Anwander, T.R. Knosche, C.H. Wolters, M. Dumpelmann, D.S. Tuch, and J.R. Reichenbach. Influence of anisotropic conductivity on EEG source reconstruction: investigations in a rabbit model. *IEEE Transactions on Biomedical Engineering*, 53(9):1841–1850, September 2006.

[40] Nikita Gupta and Swapna Devi. EEG Forward Problem Solution for a Multi-Shell Head Model.

[41] Daniel Güllmar, Jens Haueisen, and Jürgen R. Reichenbach. Influence of anisotropic electrical conductivity in white matter tissue on the EEG/MEG forward and inverse solution. A high-resolution whole head simulation study. *NeuroImage*, 51(1):145–163, May 2010.

[42] Hans Hallez, Steven Staelens, and Ignace Lemahieu. Dipole estimation errors due to not incorporating anisotropic conductivities in realistic head models for eeg source analysis. *Physics in medicine and biology*, 54(20):6079, 2009.

[43] Hans Hallez, Bart Vanrumste, Roberta Grech, Joseph Muscat, Wim De Clercq, Anneleen Vergult, Yves D'Asseler, Kenneth P Camilleri, Simon G Fabri, Sabine Van Huffel, and Ignace Lemahieu. Review on solving the forward problem in EEG source analysis. *Journal of NeuroEngineering and Rehabilitation*, 4(1):46, 2007.

[44] Matti S. Hamalainen and Jukka Sarvas. Realistic conductivity geometry model of the human head for interpretation of neuromagnetic data. *Biomedical Engineering, IEEE Transactions on*, 36(2):165–171, 1989.

[45] Jens Haueisen, David S Tuch, C Ramon, PH Schimpf, VJ Wedeen, JS George, and JW Belliveau. The influence of brain tissue anisotropy on human eeg and meg. *Neuroimage*, 15(1):159–166, 2002.

[46] H. V. Henderson and S. R. Searle. On Deriving the Inverse of a Sum of Matrices. *SIAM Review*, 23(1):53–60, January 1981.

[47] Ralf Hiptmair. Operator preconditioning. *Computers and mathematics with Applications*, 52(5):699–706, 2006.

[48] Ralf Hiptmair, Carlos Jerez-Hanckes, and Carolina Urzúa-Torres. Mesh-independent operator preconditioning for boundary elements on open curves. *SIAM Journal on Numerical Analysis*, 52(5):2295–2314, 2014.

[49] R Hoekema, GH Wieneke, FSS Leijten, CWM Van Veelen, PC Van Rijen, GJM Huiskamp, J Ansems, and AC Van Huffelen. Measurement of the conductivity of skull, temporarily removed during epilepsy surgery. *Brain topography*, 16(1):29–38, 2003.

[50] Saburo Homma, Toshimitsu Musha, Yoshio Nakajima, Yoshiwo Okamoto, Sigge Blom, Roland Flink, and Karl-Erik Hagbarth. Conductivity ratios of the scalp-skull-brain head model in estimating equivalent dipole sources in human brain. *Neuroscience research*, 22(1):51–55, 1995.

[51] Carlos Jerez-Hanckes and Jean-Claude Nédélec. Explicit Variational Forms for the Inverses of Integral Logarithmic Operators Over an Interval. *SIAM Journal on Mathematical Analysis*, 44(4):2666–2694, January 2012.

[52] Shidong Jiang and Vladimir Rokhlin. Second kind integral equations for the classical potential theory on open surfaces I: analytical apparatus. *Journal of Computational Physics*, 191(1):40–74, October 2003.

[53] D. S. Jones. Note on the integral equation for a straight wire antenna. In *IEE Proceedings H (Microwaves, Optics and Antennas)*, volume 128, pages 114–116. IET, 1981.

[54] J. Kybic, M. Clerc, T. Abboud, O. Faugeras, R. Keriven, and T. Papadopoulo. A common formalism for the Integral formulations of the forward EEG problem. *IEEE Transactions on Medical Imaging*, 24(1):12–28, January 2005.

[55] Jan Kybic, Maureen Clerc, Olivier Faugeras, Renaud Keriven, and Théo Papadopoulo. Fast multipole acceleration of the MEG/EEG boundary element method. *Physics in Medicine and Biology*, 50(19):4695–4710, October 2005.

[56] Y Lai, W Van Drongelen, L Ding, KE Hecox, VL Towle, DM Frim, and B He. Estimation of in vivo human brain-to-skull conductivity ratio from simultaneous extra-and intra-cranial electrical potential recordings. *Clinical neurophysiology*, 116(2):456–465, 2005.

[57] G. Lantz, R. Grave de Peralta, L. Spinelli, M. Seeck, and C. M. Michel. Epileptic source localization with high density EEG: how many electrodes are needed? *Clinical neurophysiology*, 114(1):63–69, 2003.

[58] Won Hee Lee, Zhongming Liu, Bryon A Mueller, Kelvin Lim, and Bin He. Influence of white matter anisotropic conductivity on eeg source localization: comparison to fmri in human primary visual cortex. *Clinical Neurophysiology*, 120(12):2071–2081, 2009.

[59] Eric C Leuthardt, Gerwin Schalk, Jarod Roland, Adam Rouse, and Daniel W Moran. Evolution of brain-computer interfaces: going beyond classic motor physiology. *Neurosurgical focus*, 27(1):E4, 2009.

[60] Emmanouil Magiorkinis, Kalliopi Sidiropoulou, and Aristidis Diamantis. Hallmarks in the history of epilepsy: epilepsy in antiquity. *Epilepsy & Behavior*, 17(1):103–108, 2010.

[61] Gildas Marin, Christophe Guerin, Sylvain Baillet, Line Garnero, and Gérard Meunier. Influence of skull anisotropy for the forward and inverse problem in EEG: simulation studies using FEM on realistic head models. *Human brain mapping*, 6(4):250–269, 1998.

[62] Per-Gunnar Martinsson. Compressing rank-structured matrices via randomized sampling. *SIAM Journal on Scientific Computing*, 3844(4):1959–1986, 2016.

[63] W. McLean and Olaf Steinbach. Boundary element preconditioners for a hypersingular integral equation on an interval. *Advances in Computational Mathematics*, 11(4):271–286, 1999.

[64] Takfarinas Medani, David Lautru, Denis Schwartz, Zhuoxiang Ren, and Gérard Sou. Fem method for the eeg forward problem and improvement based on modification of the saint venant's method. *Progress In Electromagnetics Research*, 153:11–22, 2015.

[65] J. Meixner. The behavior of electromagnetic fields at edges. *IEEE Transactions on Antennas and Propagation*, 20(4):442–446, Jul 1972.

[66] Elias R Melhem, Susumu Mori, Govind Mukundan, Michael A Kraut, Martin G Pomper, and Peter CM van Zijl. Diffusion tensor mr imaging of the brain and white matter tractography. *American Journal of Roentgenology*, 178(1):3–16, 2002.

[67] Christoph M. Michel and Micah M. Murray. Towards the utilization of EEG as a brain imaging tool. *NeuroImage*, 61(2):371–385, 2012.

[68] Christoph M. Michel, Micah M. Murray, Göran Lantz, Sara Gonzalez, Laurent Spinelli, and Rolando Grave de Peralta. EEG source imaging. *Clinical Neurophysiology*, 115(10):2195–2222, October 2004.

[69] Victoria Montes-Restrepo, Pieter van Mierlo, Gregor Strobbe, Steven Staelens, Stefaan Vandenberghe, and Hans Hallez. Influence of skull modeling approaches on eeg source localization. *Brain topography*, 27(1):95–111, 2014.

[70] Jean-Claude Nedelec. *Acoustic and electromagnetic equations: integral representations for harmonic problems*. Springer, New York, 2001.

[71] Soheyl Noachtar and Jan Rémi. The role of eeg in epilepsy: a critical review. *Epilepsy & Behavior*, 15(1):22–33, 2009.

[72] Paul L. Nunez and Ramesh Srinivasan. *Electric fields of the brain: the neurophysics of EEG*. Oxford university press, 2006.

[73] Seiji Ogawa, Tso-Ming Lee, Alan R Kay, and David W Tank. Brain magnetic resonance imaging with contrast dependent on blood oxygenation. *Proceedings of the National Academy of Sciences*, 87(24):9868–9872, 1990.

[74] Emmanuel Olivi, Theodore Papadopoulo, and Maureen Clerc. Handling white-matter anisotropy in BEM for the EEG forward problem. pages 799–802. IEEE, March 2011.

[75] Emmanuel Olivi, Théodore Papadopoulo, and Maureen Clerc. Handling white-matter anisotropy in bem for the eeg forward problem. In *Biomedical Imaging: From Nano to Macro, 2011 IEEE International Symposium on*, pages 799–802. IEEE, 2011.

[76] Thom F Oostendorp, Jean Delbeke, and Dick F Stegeman. The conductivity of the human skull: results of in vivo and in vitro measurements. *Biomedical Engineering, IEEE Transactions on*, 47(11):1487–1492, 2000.

[77] Robert Oostenveld, Pascal Fries, Eric Maris, and Jan-Mathijs Schoffelen. Fieldtrip: open source software for advanced analysis of meg, eeg, and invasive electrophysiological data. *Computational intelligence and neuroscience*, 2011, 2010.

[78] Robert Oostenveld and Thom F Oostendorp. Validating the boundary element method for forward and inverse eeg computations in the presence of a hole in the skull. *Human brain mapping*, 17(3):179–192, 2002.

[79] Roberto Domingo Pascual-Marqui. Review of methods for solving the EEG inverse problem. *International journal of bioelectromagnetism*, 1(1):75–86, 1999.

[80] Roberto Domingo Pascual-Marqui and others. Standardized low-resolution brain electromagnetic tomography (sLORETA): technical details. *Methods Find Exp Clin Pharmacol*, 24(Suppl D):5–12, 2002.

[81] Marco Piccolino. Animal electricity and the birth of electrophysiology: the legacy of luigi galvani. *Brain research bulletin*, 46(5):381–407, 1998.

[82] Chris Plummer, A. Simon Harvey, and Mark Cook. EEG source localization in focal epilepsy: Where are we now? *Epilepsia*, 49(2):201–218, February 2008.

[83] Chris Plummer, A Simon Harvey, and Mark Cook. Eeg source localization in focal epilepsy: where are we now? *Epilepsia*, 49(2):201–218, 2008.

[84] Vadim S Polikov, Patrick A Tresco, and William M Reichert. Response of brain tissue to chronically implanted neural electrodes. *Journal of neuroscience methods*, 148(1):1–18, 2005.

[85] GW Pruis, Brian H Gilding, and MJ Peters. A comparison of different numerical methods for solving the forward problem in eeg and meg. *Physiological measurement*, 14(4A):A1, 1993.

[86] Ian L Pykett, Jeffrey H Newhouse, Ferdinando S Buonanno, Thomas J Brady, Mark R Goldman, J Philip Kistler, and Gerald M Pohost. Principles of nuclear magnetic resonance imaging. *Radiology*, 143(1):157–168, 1982.

[87] B. Quercia, F. P. Andriulli, and K. Cools. Solving the low-frequency breakdown of the wire-efie without the search for global loops. In *2016 10th European Conference on Antennas and Propagation (EuCAP)*, pages 1–3, April 2016.

[88] Lyes Rahmouni, Simon Adrian, Kristof Cools, and Francesco P. Andriulli. Conforming discretizations of boundary element solutions of the electroencephalography forward problem. *Submitted to NeuroImage*, 2016. preprint arXiv:1603.06283.

[89] Ceon Ramon, Paul H. Schimpf, and Jens Haueisen. Influence of head models on EEG simulations and inverse source localizations. *BioMedical Engineering Online*, 5(1):10, 2006.

[90] S. Rush and D. A. Driscoll. Current distribution in the brain from surface electrodes. *Anesthesia & Analgesia*, 47(6):717–723, 1968.

[91] Jukka Sarvas. Basic mathematical and electromagnetic concepts of the biomagnetic inverse problem. *Physics in medicine and biology*, 32(1):11, 1987.

[92] Stefan A. Sauter and Christoph Schwab. *Boundary Element Methods*, volume 39 of *Springer Series in Computational Mathematics*. Springer Berlin Heidelberg, Berlin, Heidelberg, 2011.

[93] Tonio Ball; Markus Kern; Isabella Mutschler; Ad Aertsen; Andreas Schulze-Bonhage. Signal quality of simultaneously recorded invasive and non-invasive eeg. *NeuroImage*, 46, 2009.

[94] Olaf Steinbach. *Numerical approximation methods for elliptic boundary value problems: finite and boundary elements*. Springer, New York, 2008.

[95] Olaf Steinbach and Wolfgang L Wendland. The construction of some efficient preconditioners in the boundary element method. *Advances in Computational Mathematics*, 9(1-2):191–216, 1998.

[96] M Stenroos and J Sarvas. Bioelectromagnetic forward problem: isolated source approach revis (it) ed. *Physics in medicine and biology*, 57(11):3517, 2012.

[97] François Tadel, Sylvain Baillet, John C Mosher, Dimitrios Pantazis, and Richard M Leahy. Brainstorm: a user-friendly application for meg/eeg analysis. *Computational intelligence and neuroscience*, 2011:8, 2011.

[98] David S. Tuch, Van J. Wedeen, Anders M. Dale, John S. George, and John W. Belliveau. Conductivity tensor mapping of the human brain using diffusion tensor MRI. *Proceedings of the National Academy of Sciences*, 98(20):11697–11701, 2001.

[99] Bart Vanrumste, Gert Van Hoey, Rik Van de Walle, RP D Michel, Ignace A Lemahieu, and Paul AJM Boon. The validation of the finite difference method and reciprocity for solving the inverse problem in eeg dipole source analysis. *Brain topography*, 14(2):83–92, 2001.

[100] V.S. Vladimirov. *Equations of mathematical physics*. Pure and applied mathematics. M. Dekker, 1971.

[101] J Vorwerk, M Clerc, M Burger, and CH Wolters. Comparison of boundary element and finite element approaches to the eeg forward problem. *Biomedical Engineering/Biomedizinische Technik*, 57(SI-1 Track-O):795–798, 2012.

[102] Johannes Vorwerk, Jae-Hyun Cho, Stefan Rampp, Hajo Hamer, Thomas R Knösche, and Carsten H Wolters. A guideline for head volume conductor modeling in eeg and meg. *NeuroImage*, 100:590–607, 2014.

[103] C H Wolters, L Grasedyck, and W Hackbusch. Efficient computation of lead field bases and influence matrix for the FEM-based EEG and MEG inverse problem. *Inverse Problems*, 20(4):1099–1116, August 2004.

[104] Carsten Hermann Wolters, Alfred Anwander, X Tricoche, D Weinstein, Martin A Koch, and RS MacLeod. Influence of tissue conductivity anisotropy on eeg/meg field and return current computation in a realistic head model: a simulation and visualization study using high-resolution finite element modeling. *NeuroImage*, 30(3):813–826, 2006.

[105] Y Yan, PL Nunez, and RT Hart. Finite-element model of the human head: scalp potentials due to dipole sources. *Medical and Biological Engineering and Computing*, 29(5):475–481, 1991.

[106] Zhi Zhang. A fast method to compute surface potentials generated by dipoles within multilayer anisotropic spheres. *Physics in medicine and biology*, 40(3):335, 1995.

[107] Zhi Zhang. A fast method to compute surface potentials generated by dipoles within multilayer anisotropic spheres. *Physics in medicine and biology*, 40(3):335, 1995.

[108] H. Zhou and A. van Oosterom. Application of the boundary element method to the solution of anisotropic electromagnetic problems. *Medical and Biological Engineering and Computing*, 32(4):399–405, July 1994.

Résumé

La reconstruction des sources de l'activité cérébrale à partir des mesures de potentiel fournies par un électroencéphalographie (EEG) nécessite de résoudre le problème connu sous le nom de « problème inverse de l'EEG ». La solution de ce problème dépend de la solution du « problème direct de l'EEG », qui fournit à partir de sources de courant connues, le potentiel mesuré au niveau des électrodes. Pour des modèles de tête réels, ce problème ne peut être résolut que de manière numérique. En particulier, les équations intégrales de surfaces requièrent uniquement la discrétisation des interfaces entre les différents compartiments constituant le milieu cérébral. Cependant, les formulations intégrales existant actuellement ne prennent pas en comptent l'anisotropie du milieu. Le travail présenté dans cette thèse introduit deux nouvelles formulations intégrales permettant de palier à cette faiblesse. Une formulation indirecte capable de prendre en compte l'anisotropie du cerveau est proposée. Elle est discrétisée à l'aide de fonctions conformes aux propriétés spectrales des opérateurs impliqués. L'effet de cette discrétisation de type mixe lors de la reconstruction des sources cérébrales est aussi étudié. La seconde formulation se concentre sur l'anisotropie due à la matière blanche. Calculer rapidement la solution du système numérique obtenu est aussi très désirable. Le travail est ainsi complémenté d'une preuve de l'applicabilité des stratégies de préconditionnement de type Calderon pour les milieux multicouches. Le théorème proposé est appliqué dans le contexte de la résolution du problème direct de l'EEG. Un préconditionneur de type Calderon est aussi introduit pour l'équation intégrale du champ électrique (EFIE) dans le cas de structures unidimensionnelles. Finalement, des résultats préliminaires sur l'impact d'un solveur rapide direct lors de la résolution rapide du problème direct de l'EEG sont présentés.

Mots-clés : EEG, méthode des éléments de frontière, problème direct, équations intégrales, préconditionement

Abstract

Electroencephalography (EEG) is a very useful tool for characterizing epileptic sources. Brain source imaging with EEG necessitates to solve the so-called EEG inverse problem. Its solution depends on the solution of the EEG forward problem that provides from known current sources the potential measured at the electrodes positions. For realistic head shapes, this problem can be solved with different numerical techniques. In particular surface integral equations necessitates to discretize only the interfaces between the brain compartments. However, the existing formulations do not take into account the anisotropy of the media. The work presented in this thesis introduces two new integral formulations to tackle this weakness. An indirect formulation that can handle brain anisotropies is proposed. It is discretized with basis functions conform to the mapping properties of the involved operators. The effect of this mixed discretization on brain source reconstruction is also studied. The second formulation focuses on the white matter fiber anisotropy. Obtaining the solution to the obtained numerical system rapidly is also highly desirable. The work is hence complemented with a proof of the preconditioning effect of Calderon strategies for multilayered media. The proposed theorem is applied in the context of solving the EEG forward problem. A Calderon preconditioner is also introduced for the wire electric field integral equation. Finally, preliminary results on the impact of a fast direct solver in solving the EEG forward problem are presented.

Keywords : EEG, Boundary Element Method, Forward Problem, Integral Equations, Preconditioning

TELECOM Bretagne

n° d'ordre : 2016telb0412
Télécom Bretagne
Technopôle Brest-Iroise - CS 83818 - 29238 Brest Cedex 3
Tél : + 33(0) 29 00 11 11 - Fax : + 33(0) 29 00 10 00